Recent Advances on High-Entropy Alloys for 3D Printing

*Changjun Han, Qihong Fang, Yusheng Shi, Shu Beng Tor, Chee Kai Chua, Kun Zhou**

Dr. C. Han, Prof. S. B. Tor, Prof. K. Zhou
Singapore Centre for 3D Printing, School of Mechanical and Aerospace Engineering, Nanyang Technological University, 50 Nanyang Avenue, Singapore 639798, Singapore

Prof. Q. Fang
College of Mechanical and Vehicle Engineering, Hunan University, Changsha 410082, China

Prof. Y. Shi
State Key Lab of Materials Processing and Die & Mould Technology, School of Materials Science and Engineering, Huazhong University of Science and Technology, Wuhan 430074, China

Prof. C. K. Chua
Engineering Product Development, Singapore University of Technology and Design, 8 Somapah Road, Singapore 487372, Singapore

E-mail: kzhou@ntu.edu.sg

Keywords: 3D printing, additive manufacturing, high-entropy alloy, rapid solidification, powder development

Abstract

Boosted by the success of high-entropy alloys (HEAs) manufactured by conventional processes in various applications, the development of HEAs for three-dimensional (3D) printing has been advancing rapidly in recent years. 3D printing of HEAs gives rise to great potential for manufacturing geometrically complex HEA products with desirable performances, thereby inspiring their increased manifestation in industrial applications. In this paper, a comprehensive review of the recent achievements of 3D printing of HEAs is provided, in the aspects of their powder development, printing processes, microstructures, properties and potential applications. It begins with the introduction of the fundamentals of 3D printing and HEAs as well as the unique properties of 3D-printed HEA products. The processes for the development of HEA powders, including atomization and mechanical alloying, and the powder properties are then presented. Thereafter, typical processes for printing HEA products from powders, namely, directed energy deposition, selective laser

melting and electron beam melting, are discussed with regard to the phases, crystal features, mechanical properties, functionalities and potential applications of these products (particularly in the aerospace, energy, molding and tooling industries). Finally, perspectives are outlined to provide guidance for future research.

1. Introduction

Three-dimensional (3D) printing, more formally termed as additive manufacturing (AM), is an emerging technology to bring about revolutionary manufacturing by providing great flexibility for the design and fabrication of complex and/or customized parts through a layer-by-layer strategy.[1-6] For example, a complicated product previously assembled from multiple components can now be conveniently redesigned and printed as an integrated one, thus realizing tremendous design freedom. Seven categories of AM processes,[7-13] namely vat polymerization, material jetting, binder jetting, material extrusion, sheet lamination, powder bed fusion (PBF) and directed energy deposition (DED), have been developed to enable the printing of various materials including metals, polymers, ceramics and composites.[14-20]

Metal products can be printed by binder jetting, sheet lamination, PBF and DED, although these processes are not limited to metals.[21] Binder jetting selectively deposits liquid-state binder materials through a printing head onto pre-laid metal powder layers on a powder bed to glue the powder particles into products, which subsequently undergo post-processes to remove the binder materials and improve the densification of the products.[22] Sheet lamination uses ultrasonic energy to join two adjacent metal foils through the disruption of surface oxide films under low temperatures, followed by cutting to form the independent geometry of each layer.[23] PBF utilizes a focused high-energy laser beam or electron beam to melt the pre-laid powder layer in a powder bed selectively;[24-27] selective laser melting (SLM) and electron beam melting (EBM) are two typical PBF processes for printing metals. DED uses a laser, electron beam or plasma arc to melt metal powders or wires upon their deposition

along the printing paths.[28, 29] Compared to binder jetting and sheet lamination, PBF and DED undergo a metallurgical process from melting and solidification to achieve fully dense and high-strength products.[30, 31]

Both PBF and DED are characterized by their ultrafast heating rates and cooling rates, with the latter reaching 10^3–10^8 K/s at the solid/liquid interface in a small-sized melt pool.[31-35] The rapid melting and solidification are derived from the short interaction time between the focused energy and metal powders, resulting in refined microstructures that are beneficial in improving the mechanical properties of printed products.[36] Due to such characteristics, PBF and DED have been widely utilized in various applications within the aerospace, energy, biomedical, automotive, marine and offshore, molding and tooling industries.[37]

High-entropy alloys (HEAs), emerging as a novel frontier in the metal materials community,[38-43] have high mixing configurational entropies that tend to stabilize solid solutions based on simple underlying face-centered cubic (FCC), body-centered cubic (BCC) or hexagonal close-packed (HCP) structures.[44-47] In general, the definition of an HEA is based on composition or entropy. For the composition-based definition, an HEA is composed of five or more principal elements each with a concentration between 5 and 35 atomic percentage (at%).[48] According to the entropy-based definition, an HEA has a configurational entropy larger than 1.5R, which is calculated by $\Delta S_{\mathrm{conf}} = -\mathrm{R}\sum_{i=1}^{n} c_i \ln c_i$, where R is the molar gas constant, c_i the mole fraction of the i^{th} element, and n the number of its constituent elements.[49] Not limited to these definitions, some researchers suggested four-equimolar-element alloys as HEAs.[45, 50] The constituent elements of HEAs can be selected from transition metals, alkaline earth metals, basic metals, metalloids and non-metals, where Co, Cr, Cu, Fe, Mn, Ni, Hf, Ta, Ti, Mo, Nb, V, Zr, W, Zn, Al, Si and B are commonly used.[51] Through screening proper combinations of their constituent elements and regulating their proportions, HEAs can exhibit remarkable mechanical properties at high temperatures and exceptional strength, ductility and fracture toughness at cryogenic temperatures, as well as

superparamagnetism, superconductivity and exceptional irradiation resistance.[43, 52-57] Therefore, they are considered alternatives for high-temperature turbine blades, high-temperature molds and dies, hard coatings on cutting tools, components of 4th generation nuclear reactors, etc.[58]

Compared to conventional manufacturing processes, DED and PBF hold greater promise for the development of HEA products. The focused high-energy beam in DED and PBF melts powders into near-fully dense products. Simultaneously, the ultrafast cooling rates of DED and PBF contribute to preventing the formation of undesired intermetallic compounds and the diffusion of the constituent elements, and lead to the microstructure refinement of HEA products. However, rapid solidification causes a large temperature gradient that produces residual stresses and cracks in the printed products. Thus, the constituent elements insensitive to cracks and strong enough to counteract residual stresses can be considered primarily for the composition design of HEA powders to improve their printability. Both DED and PBF utilize HEA pre-alloyed powders developed by gas atomization, water atomization or mechanical alloying to achieve homogeneity of the printed products. In addition, DED enables the printing of HEA products using elemental powders through *in situ* alloying, which circumvents the lengthy process of developing HEA powders. Other advantages in DED and PBF, such as design freedom and the capability to manufacture complex geometries, open up an avenue of producing lightweight, customizable and non-assembly required 3D-printed HEA products for industrial applications. An overview of the relationships between HEAs and 3D printing is illustrated in **Figure 1**.

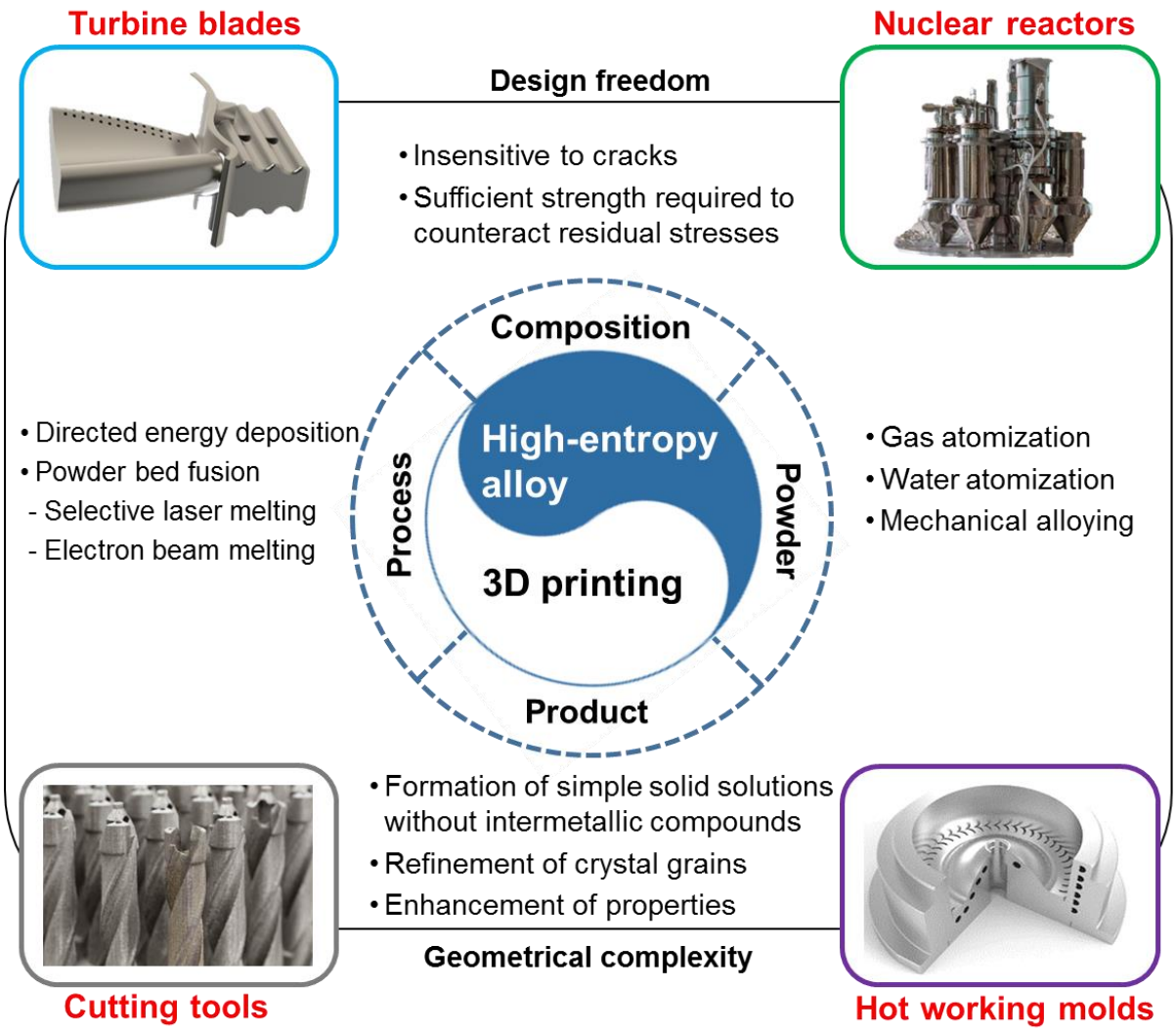

Figure 1. Overview of the relationship between HEAs and 3D printing, with regard to the composition design, powder development, printing processes, product characteristics and potential applications.

Recent substantial reviews have reported on HEAs,[27, 51, 52, 54, 59-63] but most of them focused on the design principles, metallurgical mechanisms, phase transformations, microstructure and properties of HEAs manufactured by conventional processes. There have also been a few reviews related to the 3D printing of HEAs. Li *et al.* reviewed a comparison of the processeses, microstructures and mechanical properties between HEA and bulk metallic glass products manufactured by 3D printing.[64] Chen *et al.* provided a brief review on different 3D-printed HEA products with regard to their microstructure and mechanical properties.[65] In view of the rapid development of HEAs and the increasingly significant roles

in 3D printing in current investigations, a timely summary of the insightful works in this field is of great importance to guide the development of 3D printing of HEAs.

Hence, this article is intended to provide a comprehensive review on the 3D printing of HEAs with regard to the powder development, printing processes, unique microstructures and properties of printed products as well as their potential applications. After a brief introduction in Section 1, Section 2 summarizes the processes for the development of HEA powders with the desired physical and chemical properties. In Section 3, 3D-printed HEA products using powders will be reviewed in terms of their phases and crystal features. Section 4 presents the mechanical properties and functionalities of printed HEA products and their potential applications. Finally, Section 5 concludes with perspectives on the challenges faced and opportunities presented in the development of 3D printing of HEAs.

2. Processes for HEA powder development

Powder properties determine the quality and performances of DED and PBF products. A poor powder quality can produce defects, such as pores, cracks, inclusions and suboptimal surface roughness, in the printed products. **Figure 2** illustrates the requirement diagram of HEA powders for DED and PBF printing processes, involving their chemical compositions, flowability, optical and thermal properties. It was suggested that the powder particles of HEAs should have a high mixing entropy exceeding 1.5R.[49, 66] Their spherical morphology, smooth surface and narrow size distribution contribute to good powder flowability.[67]

Various processes have been used to develop metal powders for 3D printing, including gas atomization, water atomization, plasma atomization, plasma rotating electrode process, mechanical alloying, chemical reduction, chloride reduction, hydride-dehydride process, electrolysis process, carbonyl process, plasma spheroidization, etc. Currently, gas atomization, water atomization and mechanical alloying processes are used to develop HEA powders. Gas atomization and water atomization allow for the production of spherical powder particles,

while mechanical alloying prepares irregular-shape powder particles that need to be processed to achieve high degrees of sphericity for good printability. The optical properties (absorption, reflection and transmission) and the thermal properties (specific heat, thermal conductivity, latent heat and expansion coefficient) of powders also influence the process parameters in 3D printing. Therefore, a strong understanding of such properties is vital to the development of printable HEA powders.

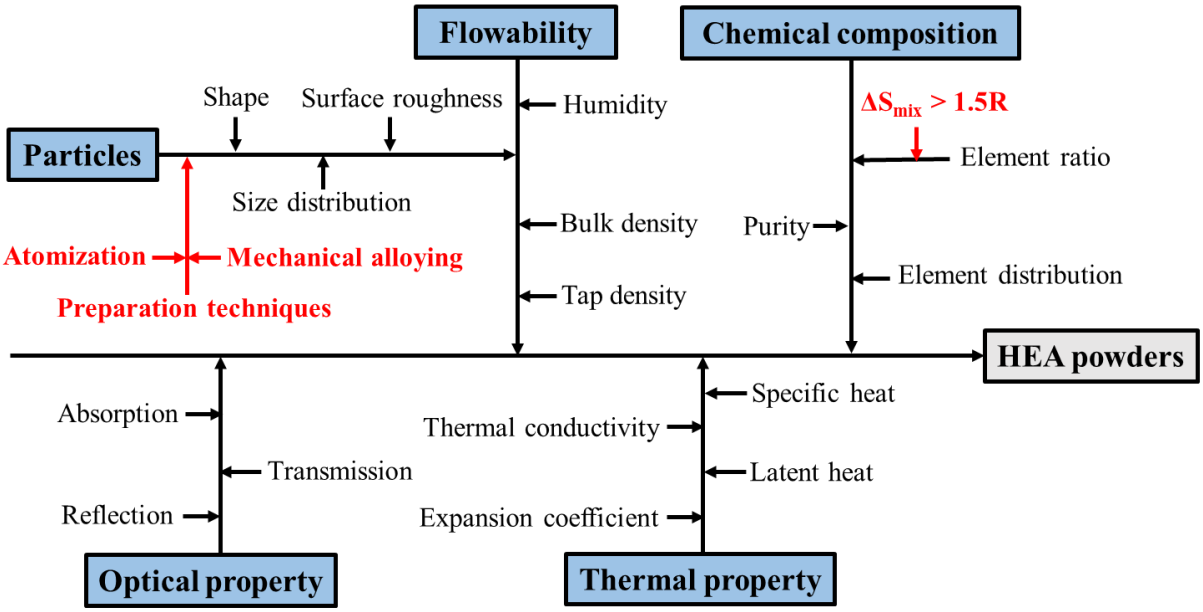

Figure 2. Requirement diagram of HEA powders for DED and PBF printing processes, where ΔS_{mix} denotes the mixing entropy and R the gas constant.

2.1. Atomization

Atomization has been established as a promising technology in recent years to develop pre-alloyed powders for DED and PBF. It utilizes high pressure from gas, water, plasma or rotating forces to disintegrate a thin stream of molten metal into liquid droplets that subsequently solidify to form spherical powder particles. Gas atomization and water atomization have been reportedly used to develop printable HEA powders.

Gas atomization is presently the most widely accepted method in the production of fine metal spherical powders for 3D printing.[68-70] A schematic of its experimental setup is presented in **Figure 3**a. First, HEA ingots or pure elements of compositions are melted in a

crucible melting furnace to prepare a molten stream. Then, the stream is broken down into droplets from the impact of a high-pressure and high-speed gas through an atomizer. In this process, a shockwave is produced in the gas/melt impact zone, which converts the kinetic energy of the gas into the surface energy and kinetic energy of the droplets. The droplets will solidify to form powder particles during their flight before they reach the walls of the atomization chamber. The mechanism on the stream disintegration consists of two stages.[71] In the primary stage, the molten metal is disturbed by sinusoidal oscillations from the high-pressure gas and then broken into huge droplets or unstable ligaments due to surface tension and fluctuations. In the secondary stage, the droplets or ligaments are further disintegrated into flight either by a low-turbulence mechanism or by more chaotic high-turbulence procedures in a stripping fashion and then solidified into spherical powder particles of different sizes (Figure 3b).[72, 73] **Table 1** summarizes the HEA powders developed by gas atomization.

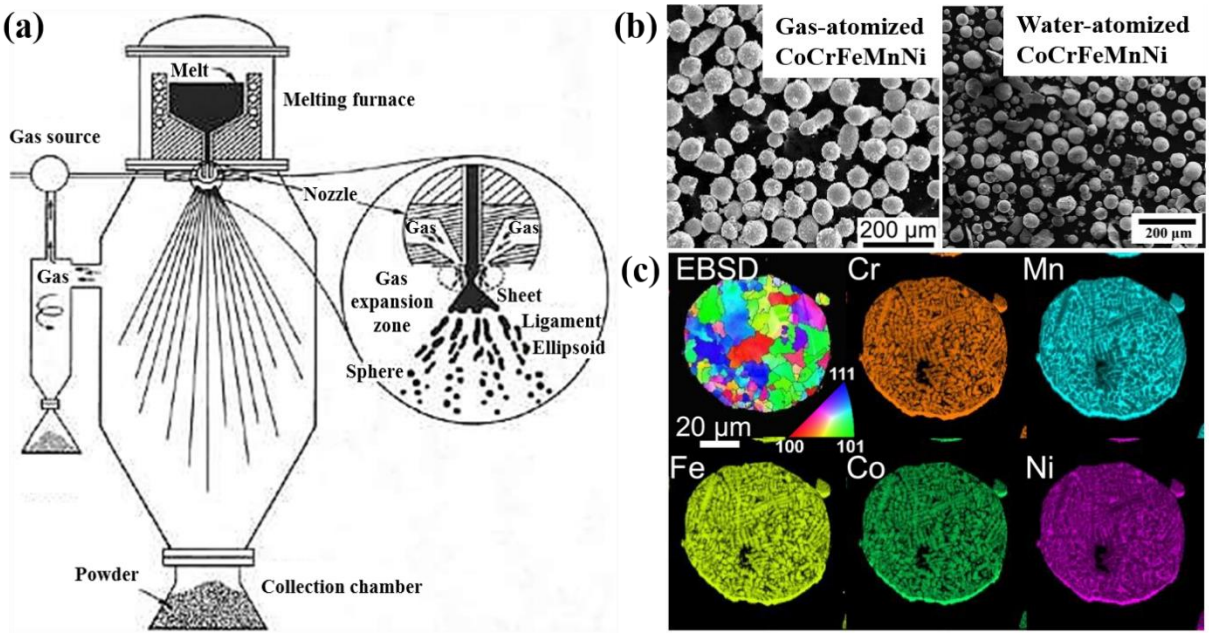

Figure 3. (a) Illustration of a typical experimental setup for gas atomization and its schematic mechanism of atomization stages, (b) morphologies of gas-atomized and water-atomized CoCrFeMnNi HEA powders,[74, 75] and (c) electron backscatter diffraction (EBSD) image and elemental distribution of a powder particle.[75] Reproduced with permission.[74] Copyright 2018, Elsevier. Reproduced with permission.[75] Copyright 2019, Elsevier.

HEA powders with high degrees of sphericity, homogeneous distributions of their constituent elements and desirable particle sizes can be developed by optimizing the gas pressure, gas flow rate and melt flow rate in gas atomization.[76-78] However, satellite particles that are generated from the solidification of small molten droplets attached to the surfaces of large droplets will be adverse to the powder flowability.[79, 80] Intensive process optimization is required to effectively minimize these satellite particles and improve the powder flow.[76]

Table 1. HEA powders developed by gas atomization.

HEA powder	Feedstock	Particle size distribution (μm)	Average particle size (μm)	Phase	Ref.
$AlCoCrFeNi_{2.1}$	Elemental metals	20–80	-	FCC + BCC	[76]
AlCoCrFeNi	-	-	70	BCC	[81]
	Alloy ingot	40–100	-	BCC	[80]
	-	-	70	BCC	[82]
	-	45–105	-	-	[83]
	Elemental metals	-	75	BCC	[84]
$Al_{0.5}CoCrFeNi$	Elemental metals	-	33.5	FCC + BCC	[85]
$Al_{0.6}CoCrFeNi$	Alloy ingot	-	78.65	FCC + BCC	[79]
$Al_{0.5}CoCrFeNiCu$	Alloy ingot	-	27	FCC	[77]
$Al_{0.5}CoCrFeNiCuSi$	Alloy ingot	-	27	FCC + BCC	
AlCoCrFeNiCu	-		47.88	FCC	[86]
CoCrFeNi	Elemental metals	-	35.2	FCC	[87]
CoCrFeNiMn	-	63–160	-	FCC	[88]
	Elemental metals	-	45.2	FCC	[89]
	-	5–45	36	FCC	[90]
CoCrFeNiMn	Alloy ingot	0–53; 100–150	-	FCC	[91]
	-	-	36	FCC	[92]
$CoCrFeNiC_{0.05}$	-	9–85	45	FCC	[93]
$CoCrFeNiMo_{0.2}$	Alloy ingot	15–45	-	FCC	[78]

Particle size strongly influences the phases and morphologies of HEA powders. Zhou *et al.* discovered that gas-atomized $Al_{0.6}CoCrFeNi$ powder particles with sizes greater than 75 μm consisted of FCC + BCC phases, whereas particles with sizes less than 75 μm only exhibited a BCC phase.[79] The high cooling rates in the small particles not only inhibited eutectic solidification but also increased the solubility of Al in CoCrFeNi to form the BCC phase.

Besides, the decrease in particle size improves the surface quality of HEA powder particles. Park *et al.* indicated that CoCrFeNiMn powder particles with sizes less than 53 μm had spherical shapes and smooth surfaces without satellites or defects, compared to those with sizes greater than 100 μm.[91]

The constituent elements and their proportions play a critical role in determining the phases of gas-atomized HEA powders. The CoCrFeNi-based HEA powders obtain an FCC phase regardless of the presence of Mn, Mo and C elements. In addition to the strong FCC stabilizer of Co, the high cooling rates of gas atomization (10^4–10^5 K/s) are also advantageous to avoid compositional segregation and limit the atomic ordering required for the formation of intermetallic compounds.[94] In contrast, the phases in the AlCoCrFeNi-based HEA powders are dependent on both the type of elements and their proportions. For instance, the addition of Si to AlCoCrFeNiCu initiated the phase transformation from FCC to BCC,[77] while a higher Al content in the powder led to a BCC-dominant structure due to the strong BCC stabilizing effect of Al.[95-97] The high mixing entropies in HEA powders compete with mixing enthalpies to lower their Gibbs free energies, thus enhancing the solubility of these solid solutions.

Gas-atomized HEA powders exhibit remarkable properties due to their simple microstructures and homogeneous element distributions, as presented in Figure 3c. Ding *et al.* investigated the electrochemical and magnetic properties of a gas-atomized $AlCoCrFeNi_{2.1}$ powder.[76] The powder not only exhibited better corrosion resistance than stainless steel powders, but also possessed characteristics of soft magnetic materials with the a saturation magnetization of 8.67 emu/g, a remanence ratio of 2.07 % and a coercivity of 19.17 Oe. Yang *et al.* highlighted that the addition of Si brought about a 3.5-fold increment in the hardness of the gas-atomized AlCoCrFeNiCu powder.[77]

Water atomization, schematically similar to gas atomization, utilizes water jets instead of high-pressure gases as the atomizing medium. The water-atomized powders are typically dehydrated, heated and dried.[98-100] The cooling rate for water atomization is 10–100 times

larger than that of gas atomization due to the cooling medium, water, having a higher specific heat capacity.[101] Molten droplets with large surface tensions will solidify into near-spherical powder particles, while droplets with small surface tensions tend to form irregularly shaped particles. This explains why water-atomized HEA powder particles generally possess a lower degree of sphericity than their gas-atomized counterparts (Figure 3b). By optimizing the process parameters and adjusting the degrees of superheat of alloys during water atomization, the degrees of sphericity of the produced powders can be improved.[101]

Yim *et al.* investigated the relationship between particle size distribution and compaction behavior of a water-atomized CoCrFeMnNi powder (**Figure 4**).[74] The increase in the imposed pressure and particle size contributed to the rise in the relative density of the powder. These different compaction behaviors were derived from the different strain hardening behaviors in the powder particles. Small powder particles achieve higher strain hardening than large particles during plastic deformation, due to their higher dislocation densities and shorter dislocation mean free paths. Although water atomization is not as favorable as gas atomization for HEA powder development, it brings about higher efficiency in terms of powder production due to the higher impact energy from water pressure. Water-atomized HEA powders and their printability could be explored more extensively in the future.

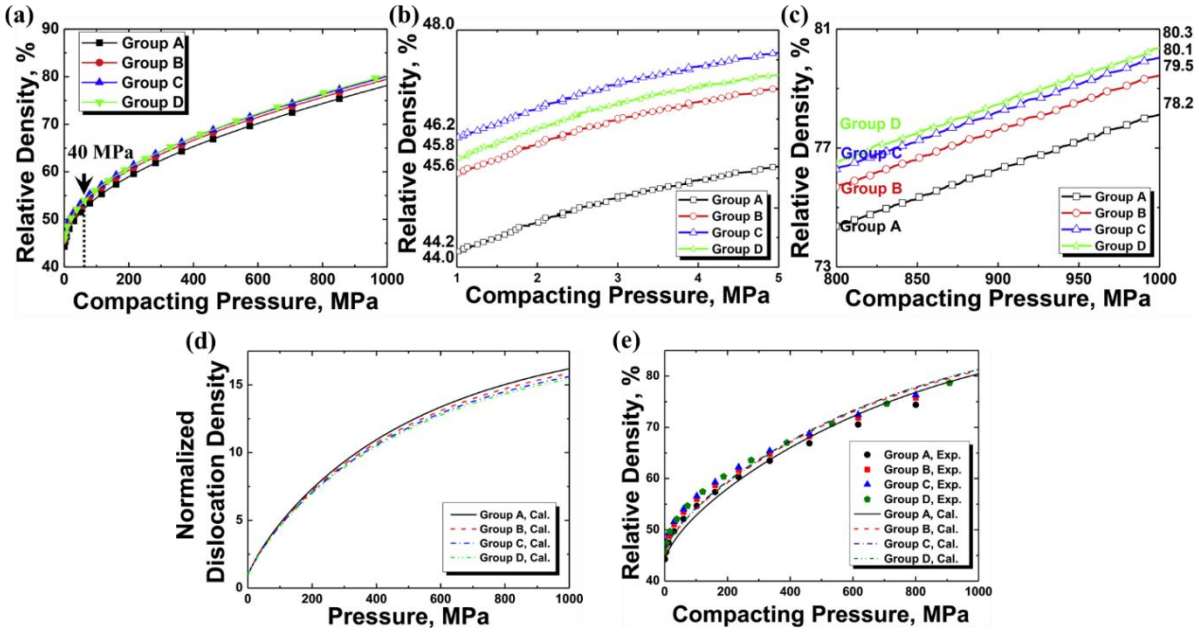

Figure 4. Compacting behaviors of a water-atomized CoCrFeMnNi HEA powder with various particle sizes: (a) compaction curves, (b) tap density, (c) relative density under higher pressure, (d) theoretical and experimental compaction curves, and (e) the calculated dislocation density. Group A, B, C and D represent the particle sizes of 0–45, 45–75, 75–105 and 105–150 μm, respectively.[74] Reproduced with permission.[74] Copyright 2018, Elsevier.

2.2. Mechanical alloying

Mechanical alloying is a high-energy ball milling process to develop fine metal powders for 3D printing.[102-104] It is one of the most promising techniques to produce homogeneous microstructures of HEA powder particles with increased solid solubility.[105, 106] As schematized in **Figure 5**a and b, elemental powders experience breaking and welding to form HEA powder particles under the rotation of the grinding bowl during the milling process. Under extreme states of hydrostatic compression, when trapped between colliding grinding balls, elemental powder particles undergo large plastic deformation before fracturing. Repeated fracturing and cold welding occur throughout the milling process, resulting in the continual refinement of the particles. When a balance is achieved between the repetitions of welding and fracturing, powder particles with a steady-state size distribution and homogeneously distributed elements will be obtained (**Figure 5**c and d).[107-109] An enhanced solid solubility, room-temperature processing and homogenous element distribution are the key benefits of mechanical alloying.[110]

Among the alloying parameters, the milling time crucially determines the phases, crystal sizes and lattice strains of HEA powder particles. Zhang *et al.* illustrated that increasing the milling time led to the weakening of diffraction peaks of an $Al_{0.4}CoFeNiSi_{0.4}$ HEA powder (**Figure 6**a).[108] This indicated that a long milling time was disadvantageous to the phase identification of the powder. The increase in the milling time decreased the crystal sizes but increased the lattice strains within the powder particles (Figure 6b), due to the rise in grain boundary fractions and lattice deformation.[112]

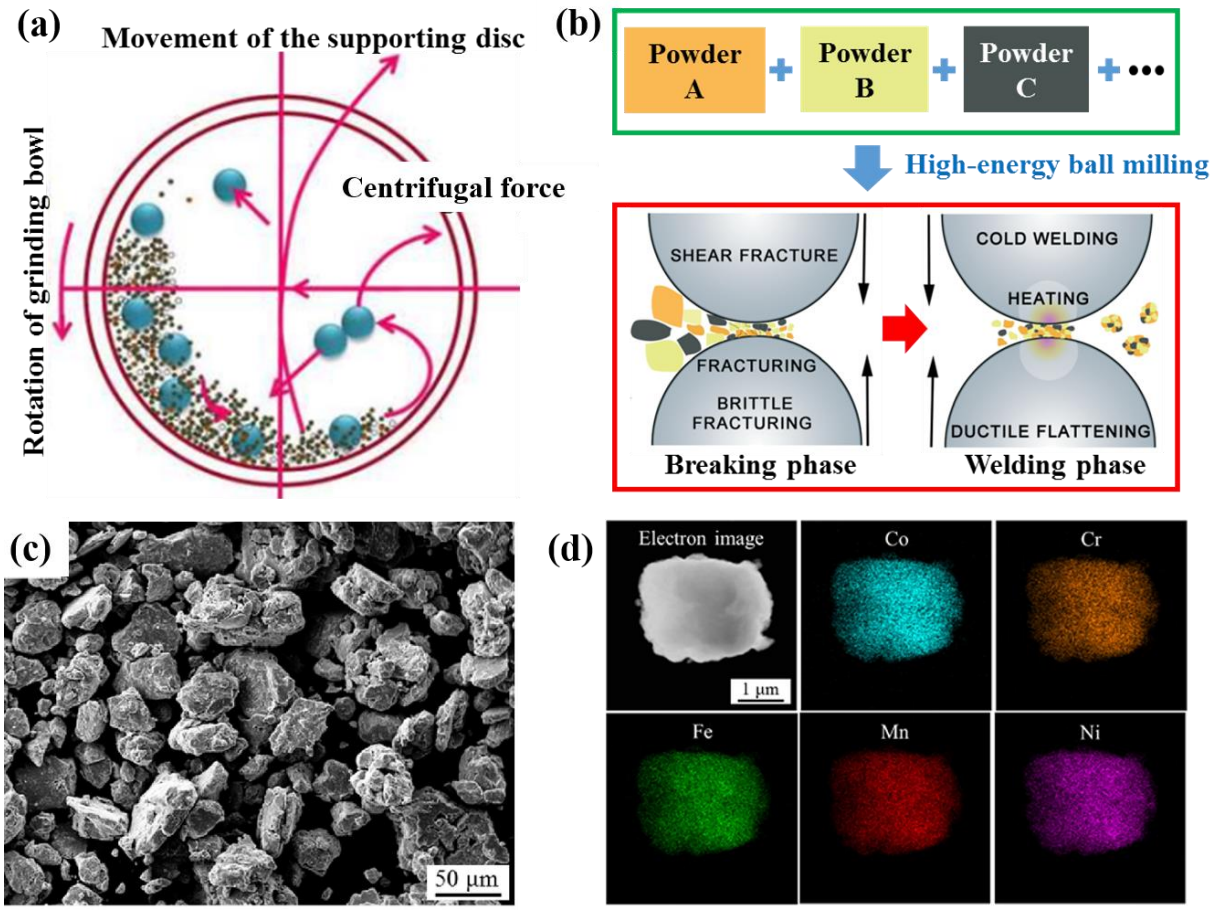

Figure 5. (a) Illustration of the mechanical alloying process, (b) schematic mechanism of mechanical alloying including breaking and welding phases, (c) morphology of a CoCrFeMnNi HEA powder produced by mechanical alloying, and (d) element distributions in a powder particle.[111] Reproduced with permission.[111] Copyright 2017, Elsevier.

In the mechanical alloying process, the repetition of cold welding and crushing promotes mutual dissolution between the different constituent elements and the formation of solid solutions (Figure 6c). Elements with low melting points or brittle crystal structures dissolve preferentially. Similar to atomization, the phases of HEA powders developed by mechanical alloying depend on the constituent elements and their proportions. Wang *et al.* reported that an Al content of less than 11 at% showed the appearance of an FCC phase in the powder particle but a higher Al amount promoted the formation of a BCC phase.[113] Zhao *et al.* showed a phase transformation of $Co_xCrFeMnNiCu$ powders from BCC to FCC with an increase in its Co content.[114] The addition of Co facilitated the formation of the FCC phase due to its higher atomic packing efficiency compared with the BCC phase. The elemental

phases remained in certain powder particles after mechanical alloying, which was attributed to the lower solid solubility of elements than the nominal composition. The solid solubility of the elements can be extended by using a powder matrix with a high storage energy and large free volume. The high storage energy provides a large thermodynamic driving force for atomic migration, while the large free volume offers a number of diffusion channels for solid-state alloying.[115] **Table 2** summarizes HEA powders developed by mechanical alloying.

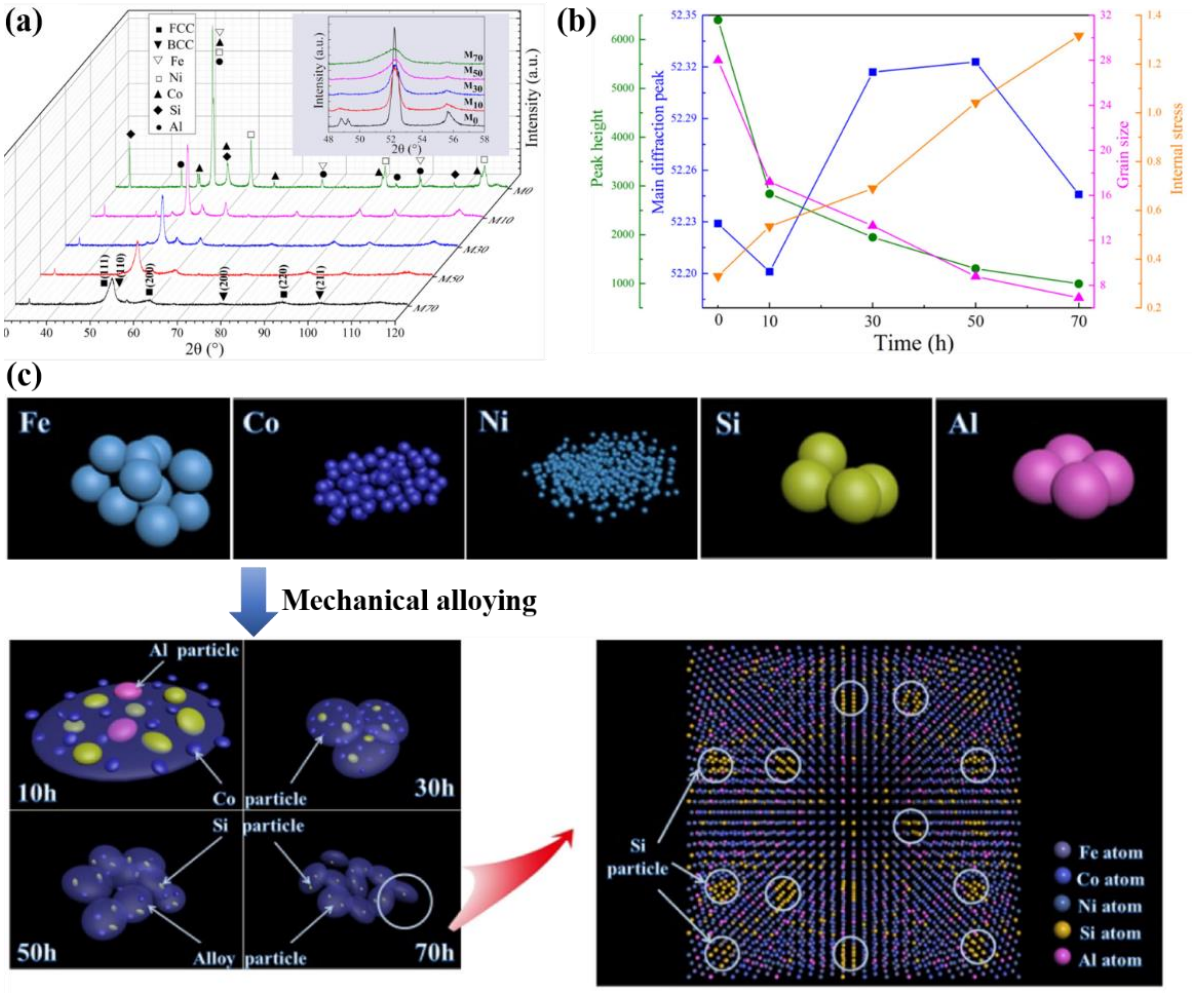

Figure 6. The $Al_{0.4}CoFeNiSi_{0.4}$ HEA powder developed by mechanical alloying with different milling times: (a) X-ray diffraction (XRD) patterns with the enlarged picture from 48° to 58° in the inset, (b) peak height, main diffraction peak angle position, grain size (nm) and internal stress (%) obtained from XRD, and (c) flow schematic illustration for the formation of powders. M0, M10, M30, M50 and M70 represent the milling times of 0, 10, 30, 50 and 70 h, respectively.[108] Reproduced with permission.[108] Copyright 2018, Elsevier.

Table 2. HEA powders developed by mechanical alloying with regard to the feedstock, milling parameters and phases.

HEA powder	Feedstock		Milling parameters				Phase	Crystallite size (nm)	Lattice strain (%)	Ref.
	Purity (wt%)	Particle size (μm)	Ball to powder ratio	Time (h)	Speed (rpm)	Apparatus				
AlCoCrFeCu	99.5	-	10:1	15	300	Pulverisette-P5	FCC + BCC	10	0.5	[116]
$Al_xCoCrFeMnNi$	99	45	18:1	14	600	Pulverisette-P7	FCC	7.4–11.4	0.84–1.28	[117]
AlCoCrFeMnNi	99	45	10:1	40	200	Retsch PM 400	BCC	15-20	0.24–0.70	[109]
AlCoCrFeNiSi	99.5	75	10:1	30	300	QM-3SP2	FCC + BCC	11.7	0.73	[118]
$Al_{0.15}CoCrCuFeNiTi_xC$	99.5–99.9	180	15:1	36	500	KMC-1BV	FCC + BCC	-	-	[119]
$AlCoCrCuFeTi_x$	-	45	10:1	20	300	Pulverisette-P5	FCC + BCC	13–58	0.096–0.231	[120]
$Al_xCrFeMoV$	99.5	-	10:1	7	200	-	BCC	-	-	[121]
$Al_{0.4}CoFeNiSi_{0.4}$	99	-	20:1	70	300	QM-QX4	FCC + BCC	-	-	[122]
$Al_{0.4}CoCr_{0.5}FeNiTi_{0.6}$	99.6	30	10:1	60	-	QM-3SP4	FCC + BCC	7	0.175	[123]
$AlCo_xFeNiSiB$	99.5	75	15:1	140	350	-	BCC	-	-	[124]
$Al_xCoFeNi_{1.5}V_{0.5}Cu_{1-x}$	99.5	48	10:1	70	300	QM-3SP4	FCC + BCC	6.3–7.7	1.21–1.52	[125]
AlCoFeNiCu	99	-	5:1	10	-	SPEX-8000M	FCC + BCC	7.1	-	[126]
AlCoCrFeNiCuTi	99	-	5:1	10	-	SPEX-8000M	FCC + BCC	6.8	-	
AlCoCrFeNiMo	99	-	5:1	10	-	SPEX-8000M	BCC	8.3–16.5	-	
AlCoNiZnCu	99.5–99.8	60	10:1	50	300	Pulverisette-P7	FCC	14.5	0.84	[127]
AlCrFeCuMnW	99.5	-	10:1	20	300	Pulverisette-P7	FCC + BCC	17–25	0.43–0.53	[128]
AlCrFeTiZnCu	99.5	45	10:1	20	300	Pulverisette-P5	BCC	9–10	1.31–1.52	[105]
$(AlCrFeMnV)_{100-x}Bi_x$	99.5	-	20:1	25	200	Pulverisette-P5	BCC + Bi	-	-	[129]
AlNiTiZrCu	99.5	70	15:1	-	350	KE-2L	amorphous	-	-	[130]
CoCrFeNi	99.5	-	10:1	15		Pulverisette-P5	FCC + BCC	10	-	[131]
CoCrCuFeNi	99.5	-	10:1	15	300	Pulverisette-P5	FCC + BCC	7	1	[116]
CoCuFeNi	99.5	-	10:1	15	300	Pulverisette-P5	FCC	9	0.73	
CoCrFeNi	99.5	-	10:1	15	300	Pulverisette-P5	FCC + BCC	6	0.83	
CoCrCuNi	99.5	-	10:1	15	300	Pulverisette-P5	FCC + BCC	6–10	-	[132]
$Co_xCrCuFeMnNi$	99.5	75	10:1	50	300	QM-WX4	FCC + BCC	5.6–8.9	1.05–1.84	[114]

	99.5	-	10:1	35	200	Pulverisette-P5	FCC	-	-	[133]
CoCrFeMnNi	99.9	-	15:1	45	250	QM-QX4L	FCC	-	-	[134]
$CoCrFeMnNiTi_{0.3}C_{0.3}$	99.9		15:1	45	250	QM-QX4L	FCC + BCC	-	-	
CoCrFeNiTi	99.9	50	25:1	10	400	-	FCC	6.38	1.4	[135]
CrFeNiMnTi	99.9	50	25:1	10	400	-	FCC	5.17	1.84	
CrFeNiTi	99.9	50	25:1	10	400	-	FCC	6.53	1.5	
$Co_{1.5}CrFeNi_{1.5}Ti_{0.5}$	99.5	-	10:1	30	250	-	FCC + BCC	-	-	[136]
$CrFeMoVMn_x$	99	75	10:1	15	200	-	BCC + σ	-	-	[121]
$(CrCuFeTiZn)_{100-x}Pb_x$	99.5	-	20:1	25	200	Pulverisette-P5	BCC + FCC + Pb	-	-	[129]
$(CuCrFeTiZn)_{100-x}Pb_x$	99.5	-	20:1	44	200	Pulverisette-P5	FCC + BCC + Pb	-	0.0372–0.1092	
NbMoTaW	99.9	48	10:1	60	300	TENCAN	BCC	11.8	0.688	[107]
NbMoTaWV	99	75	10:1	6	300	Pulverisette-P5	BCC	66.1	0.96	[137]
NbMoTaWVTi	99.9	-	13:1	40	-	-	BCC	-	-	[138]
NbMoWZrV	99.5	50	10:1	100	-	Pulverisette-P5	FCC + BCC	11	0.58	[139]
$Fe_{18}Ni_{23}Co_{25}Cr_{21}Mo_8WNb_3C_2$	99.5	70	60:1	24	940	-	γ + Mo	-	-	[115]

The magnetic properties of mechanically alloyed HEA powders are dependent on the milling time and the type and proportion of their constituent ferromagnetic elements, as illustrated in **Table 3**. Zhao *et al.* concluded that the saturation magnetization of a $Co_xCrFeMnNiCu$ HEA powder decreased with the increase in the milling time.[114] The refined crystallite sizes of the HEA resulted in the formation of a large number of boundaries, leading to a decrease in its saturation magnetization. On the other hand, the increase in coercivity contributed to an enhanced resistance to the demagnetization of a magnetic material, which was derived from the growth of defects and internal strains caused by repetitive crushing and cold welding. The milling time also showed a pronounced effect on the electromagnetic wave absorbing properties of HEA powders.[108] As the milling time increased, the particle sizes decreased and more defects were produced from the mutual solubility of elements. As a consequence, the augmentation of point polarization sites was promoted, enhancing the relative complex permittivity of HEA powders.

Table 3. Magnetic properties of reported HEA powders produced by mechanical alloying.

HEA powder	Milling time (h)	Saturation magnetization (emu/g)	Coercivity (Oe)	Ref
$Co_{0.5}CrCuFeMnNi$	50	21	63	[114]
$Co_{1.0}CrCuFeMnNi$	50	32	27	
$Co_{1.5}CrCuFeMnNi$	50	40	19	
$Co_{2.0}CrCuFeMnNi$	0/5/10/15/30/45/50	105/76/79/74/69/51/52	56/85/59/49/33/17/14	
$Al_{0.4}CoFeNiSi_{0.4}$	0/10/30/50/70	113/105/94/94/95	65/85/150/160/142	[108]
AlFeNiSiB	140/160/260	8/6/1	380/380/290	[140]
AlFeNiSiBNb	100/180/260	10/4/1	350/350/280	
AlFeNiSiBCo	40/80/140	25/15/2	320/310/230	
AlFeNiSiBC	20/40/80/140/160	53/49/32/35/27	238/338/190/75/80	[141]
AlFeNiSiBCe	20/40/80/140/160	25/6/5/2/2	250/350/325/240/230	
AlFeNiSiBCu	40/80/140	5/3/2	310/290/340	
AlFeNiSiBAg	40/80/140	15/3/2	330/320/310	
CrFeNiTi	20	14	167	[120]
CrFeMnNiTi	20	2	226	
CoCrFeNiTi	20	24	150	

In summary, HEA powders developed by gas atomization show higher degrees of sphericity, lower oxygen content and better printability compared with those produced by water atomization and mechanical alloying. Despite the high cost and low production efficiency, gas atomization is still the most popular method to develop HEA powders for PBF and DED printing processes. Mechanical alloying, in contrast to gas atomization and water atomization, can conveniently realize the alloying of any ratios of elemental powders, which provides a versatile and resource-efficient approach to design and screen compositions of HEA powders. However, mechanical alloying will undermine the sphericity of powders, resulting in poor flowability. This makes it difficult particularly for the powder spreading in PBF processes that use a recoater such as roller and scraper, and subsequently results in a poor quality of printed parts. Spheroidization techniques using plasma and pulsed electron beam irradiation,[142, 143] which are processes to convert powders with an initial irregular shape to a spherical shape, can be employed to improve the flowability and printability of mechanically alloyed HEA powders for 3D printing.

3. 3D printing of HEAs

3D printing of HEAs has attracted increasing attention from academia and industries, due to the unique merit of the 3D printing technology for printing products with design freedoms and geometric complexities. The DED and PBF processes have been greatly explored for printing HEA products, as schematized in **Figure 7**. In these processes, a focused high-energy beam interacts with powders and produces a melt pool where rapid melting and solidification occur. This rapid solidification is beneficial in avoiding elemental segregation that usually occurs at linear defects (more precisely, dislocations) or surface defects (stacking faults, grain boundaries, phase boundaries, etc.) and preventing the formation of brittle intermetallic compounds, which improves the mechanical properties of the products. This section highlights the phases and crystal features of 3D-printed HEA products.

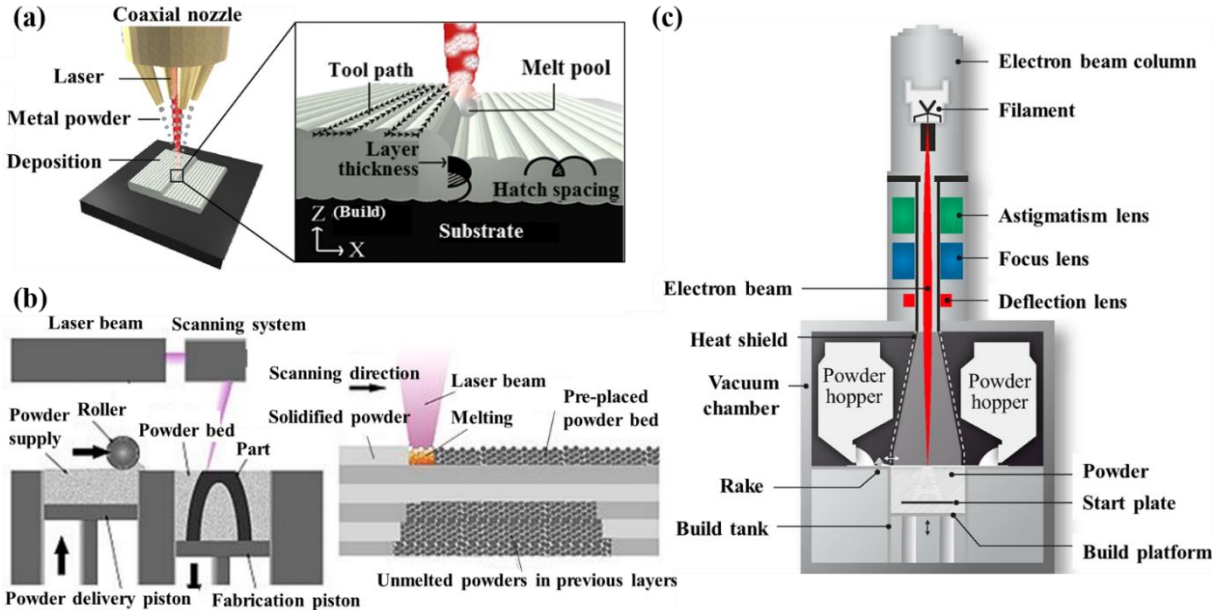

Figure 7. Schematic diagrams of major 3D printing processes for HEA products: (a) DED,[144] (b) SLM,[145] and (c) EBM.[146] Reproduced with permission.[144] Copyright 2017, Elsevier. Reproduced with permission.[145] Copyright 2019, Public Library of Science. Reproduced with permission.[146] Copyright 2018, Elsevier.

3.1. DED

DED is the most popular printing process to develop HEA products. It uses a laser or electron beam to melt metals in the forms of powders or wires upon deposition.[29, 147] The DED process based on powders melted by laser covers a range of terminologies, such as laser metal deposition, laser engineered net shaping, laser powder deposition, direct laser deposition, direct metal deposition and 3D laser cladding. As schematized in Figure 7a, powders are blown from nozzles, and a focus point is generated for powder flow. Both the focal points of the powder flow and laser are aligned for deposition, which allows the powder to fuse in a melt pool that moves in tandem with the laser.[148] DED is usually conducted in an inert environment filled with argon gas where the oxygen level can be reduced to 5–10 ppm. Compared with PBF, DED can not only use HEA powders but also utilize different pristine elemental powders fed simultaneously through multiple hoppers to print HEA products. Elemental powders are melted and deposited onto a substrate to produce melt pools, in which homogeneous element distributions can be obtained through optimizing the process

parameters of DED. After the solidification, HEA melt pools can be achieved through *in situ* alloying, which is the basis for the printing of HEA products.

The process parameters in DED, including laser power, scanning speed, powder flow rate and hatch space, play a crucial role in the properties of the printed products.[144] **Table 4** summarizes the typical DED processing conditions for printing HEA products. Optimized process parameters lead to a continuous and fully melted single track to ensure the high quality of printed products. It is critical for DED to process optimization to *in situ* fabricate HEA products using different elemental powders. Melting of at least four elemental powders has a high possibility of resulting in a discontinuous and porous melt pool with an inhomogeneous elemental distribution.[149] Therefore, remelting of each solidified melt pool is often conducted to mitigate this disadvantage and to achieve a homogeneous elemental distribution.

Table 4. The DED processing conditions for printing HEA products.

HEA	Laser power (W)	Scanning speed (mm/min)	Layer thickness (mm)	Oxygen level (ppm)	Apparatus	Ref.
AlCoCrFeNi	800	800	0.25	10	TruLaser Cell 7040	[150]
AlCoCrFeNi	600–650	300	0.7–0.8	-	-	[151]
$AlCo_xCr_{1-x}FeNi$	200–300	400	0.25	10	-	[152]
$Al_xCoCrFeNi$	800	800	-	-	TruLaser Cell 7040	[153]
$Al_xCoCrFeNi$	800–1200	400–1200	-	20	TruLaser Cell 7040	[154]
AlCoCrFeCu	1000–3000	60–900	-	-	TLF1500 TURBO	[155]
$AlCrFeMoV_x$	400	1020	0.254	10	Optomec LENS-750	[156]
AlCrFeNiTa	600–650	300	0.7–0.8	-	-	[151]
CoCrFeMnNi	370	800	-	-	Schuler	[157]
$CoCrFeNiCu_{0.5}$	250	480	-	10	Optomec LENS 750	[158]
TiZrNbMoV	300/1000	300	0.25	10	LENS MR7	[159]
ZrTiVCrFeNi	200–300	96	0.1	10	LENS MR7	[160]
LaNiFeVMn	200–300	96	0.1	10	LENS MR7	[161]

The cooling rate of DED depends on the applied laser power and scanning speed, and crucially influences the phases and crystal features of printed HEA products. The increase in the laser power causes a decrease in the cooling rate and provides sufficient time for phase

transformation. Kunce *et al.* found that a high-power laser source (1 kW) produced a BCC phase in TiZrNbMoV HEAs, whereas, a low-power laser source (300 W) generated BCC + $NbTi_4$-type phases with Zr-rich precipitates.[159] Furthermore, the increase in the scanning speed contributed to a rise in the cooling rate which further reduced the crystal sizes. They also illustrated that the cooling rate in DED rose from 2.6×10^3 K/s to 44×10^3 K/s when the scanning speed increased from 2.5 mm/s to 40 mm/s, which led to the decrease in the average grain size of printed AlCoCrFeNi HEA products from 108.3 μm to 30.6 μm.[80] The cooling rate can be obtained by the product of the thermal gradient G and crystal growth rate R, which determines the fineness of microstructure.[162] G is the derivative of temperature T with respect to distance x, otherwise denoted by dT/dx inside melt pools, while R depends on the scanning speed and the angle between the direction of the laser and crystal growth direction. A higher cooling rate (i.e., $G \times R$) leads to a higher degree of supercooling, thus increasing the nucleation rate and growth rate of nuclei. Therefore, microstructure refinement induced by the obstruction of crystal growth in printed products occurs.

DED exhibits great capability to develop functionally graded HEAs through *in situ* alloying using elemental powders. Borkar *et al.* investigated the microstructures and phases of DED-printed graded $Al_xCrCuFeNi_2$ ($0 \leq x \leq 1.5$)[163] and $AlCo_xCr_{1-x}FeNi$ ($0 \leq x \leq 1$) HEA products.[152] Variations of both phases and crystal features were created according to a predefined compositional gradient. With the increase in Al content, the printed $Al_xCrCuFeNi_2$ HEA products achieved a transition in microstructure from a disordered FCC to FCC + ordered $L1_2$, and to disordered BCC + ordered B2 (**Figure 8**). The difference between disordered and ordered phases is whether atoms occupy the specific lattice sites. The addition of Al distorted the FCC lattice, inducing the transition from a close-packed FCC phase to a more looselt packed BCC phase. The preference for BCC-based structures at high Al contents was due to the presence of partial ordering of Ni and Al atoms at few specific sites. At lower

temperatures, a complete ordered BCC phase, B2 (rich in Ni and Al), is more energetically favorable.

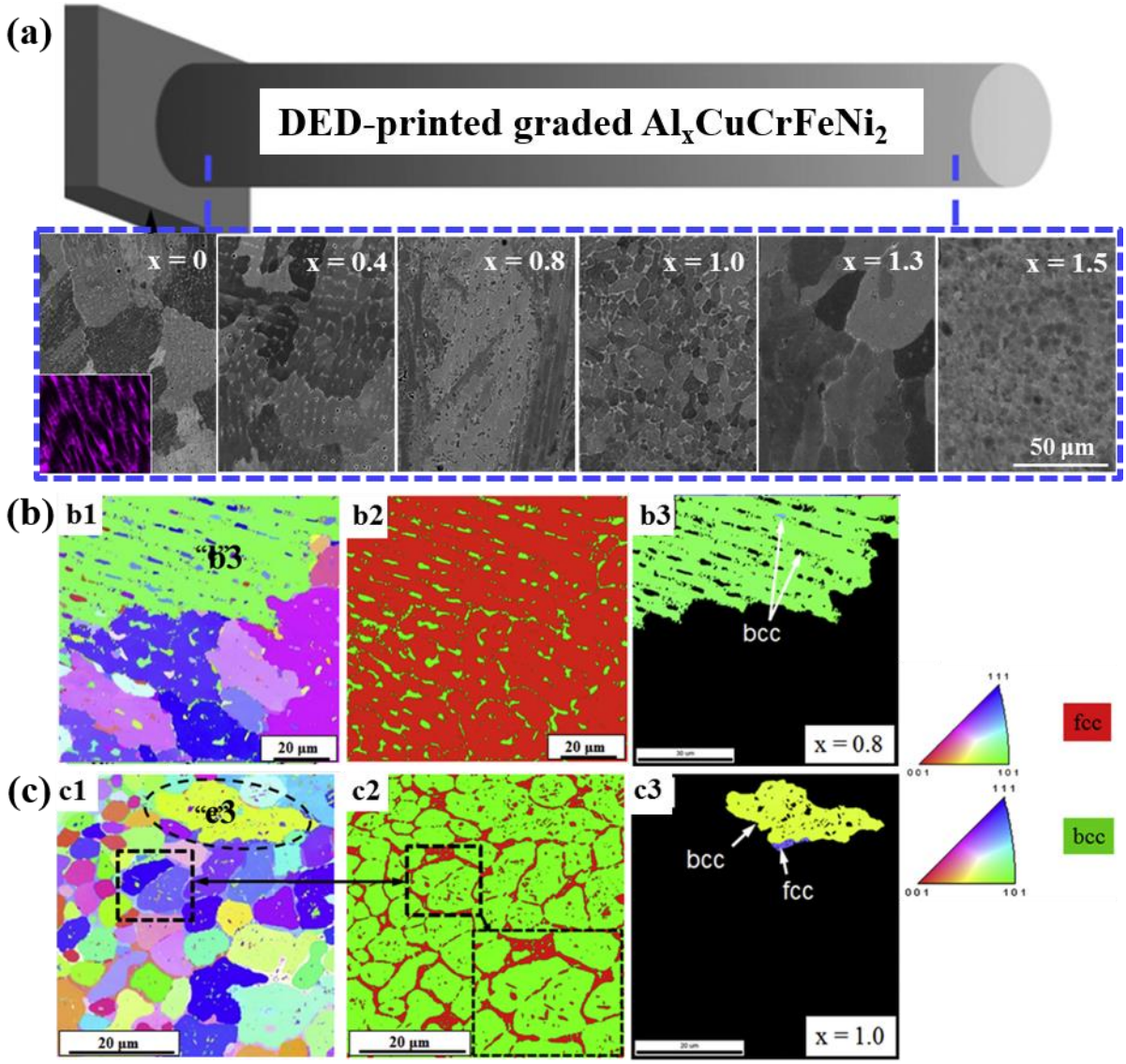

Figure 8. Microstructure of compositionally graded $Al_xCuCrFeNi_2$ HEA products printed by DED: (a) morphologies, (b) EBSD results from $Al_{0.8}CuCrFeNi_2$, (b1) various orientations and the inverse pole figure map, (b2) phase map demarking FCC and BCC regions, (b3) inverse pole figure map of a selected grain in (b1), (c) EBSD results from $AlCuCrFeNi_2$, (c1) various orientations and the inverse pole figure map, (c2) phase map demarking FCC and BCC regions, and (c3) inverse pole figure map of a selected grain in (c1).[163] Reproduced with permission.[163] Copyright 2016, Elsevier.

The intradendritic phase was FCC while the interdendritic regions were BCC (Figure 8b). The $AlCrCuFeNi_2$ products exhibited a larger fraction of BCC (green regions in Figure 8c) but smaller FCC grains (red regions in Figure 8c) compared to the $Al_{0.8}CrCuFeNi_2$ products.

Higher Al contents not only promoted a higher volume fraction of B2 phase but also refined equiaxed grains. Sista *et al.* also indicated similar results indicating that as the Al/Ni ratio decreased, the lattice parameter of $Al_xCoCrFeNi_{2-x}$ HEA products increased and the microstructure varied in the following order: dendritic grains, equiaxed grains, columnar grains.[164] Gwalani *et al.* developed graded $Al_xCoCrFeNi$ HEA products ($0.3 \leq x \leq 0.7$) using DED.[165] The results showed that $Al_{0.3}CoCrFeNi$ obtained an FCC phase whereas $Al_{0.7}CoCrFeNi$ had FCC + B2 phases, which was also observed in the study of Mohanty *et al*.[166] The printed graded HEA products achieved a heterogeneous microstructure composed of anisotropic and equiaxed grains with an FCC phase, B2 precipitates at grain boundaries, and a mixture of B2 and FCC grains exhibiting rudimentary lamellar morphologies.

On the contrary, no obvious phase transformation was observed in the graded $AlCo_xCr_{1-x}FeNi$ products.[152] As presented in **Figure 9**a–d, an intermixed network of ordered B2 + disordered BCC phases was observed in AlCrFeNi, indicating spinodal decomposition in the grains. Figure 9e shows a disordered FCC phase belonging to one of the precipitates at grain boundaries and misorientation between grains in the printed $AlCo_{0.8}Cr_{0.2}FeNi$ products. Dark-field images from the diffracting grain boundary precipitate were indexed as the [111] and [011] zone axis of the FCC phase (Figure 9f–h). As shown in Figure 9i, composition profiles recorded across the FCC precipitates through transmission electron microscope (TEM) determined its composition to be 36Co-29Fe-19Ni-11Cr-5Al (at%). In comparison, the composition for B2 + BCC grains was 29Co-18Fe-29Ni-4Cr-20Al (at%). With higher Cr contents, the graded HEAs showed a greater degree of spinodal decomposition in the BCC grains, resulting in the occurrence of different conjugate phases.

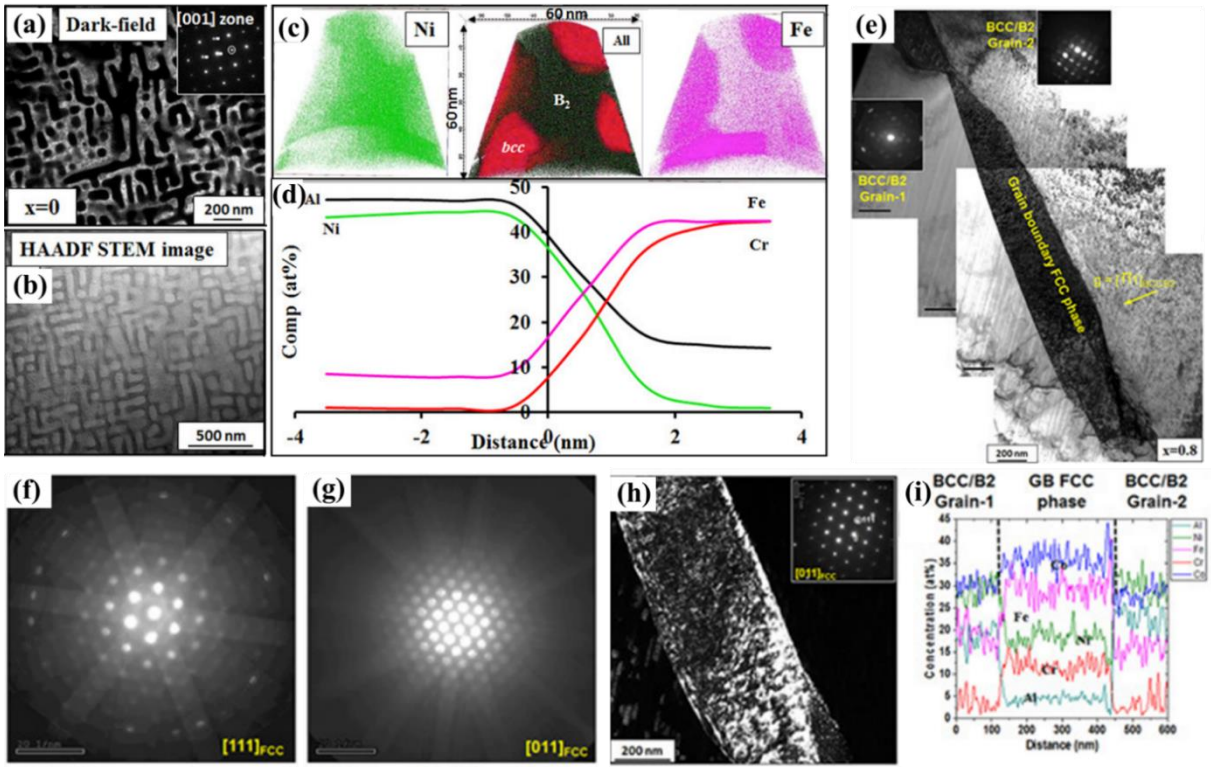

Figure 9. Phase identification in DED-printed graded $AlCo_xCr_{1-x}FeNi$ HEA products: (a) dark-field image from superlattice B2 reflection in a [001] zone axis (x = 0), (b) TEM image, (c) 3D reconstructions of atoms from atom probe tomography measurements, (d) composition profiles across a 12 at% Cr isosurface, (e) grain boundary region (x = 0.8), (f) its dark field image from the grain boundary precipitate, (g) and (h) SAD patterns from [111]FCC and [110]FCC zone axis of the precipitate, respectively, and (i) composition profiles recorded across the precipitate.[152] Reproduced with permission.[152] Copyright 2017, Wiley-VCH.

A recent study by Dobbelstein *et al.* developed crack-free graded refractory $Ti_{25}Zr_{50-x}Nb_xTa_{25}$ HEA products with x from 0 to 50 by DED.[149] The microstructure of the printed graded column is illustrated in **Figure 10**a. Equiaxed grains in region E evolved to form elongated grains in region A, along with an increase of the average grain size from 2 μm to 60 μm. The grain boundary and a dendritic core (indicated by red arrows) were enriched in Ta element, while other elements showed an opposite trend especially for Zr with a strongly depleted dendritic region. A second Ta-rich BCC phase (dotted yellow arrows) was located at grain boundaries of a Zr-rich BCC matrix (**Figure 10**b). The increase in the grain size was dependent on the cooling rate. This regulation was also found in the microstructure of DED-printed graded $AlCrFeMoV_x$ HEA products.[156] A single BCC phase was observed

throughout the composition range, which resulted from the high solubility of V element. The increase in V content from 0.3 at% to 18.5 at% led to a microstructure variation where equiaxed grains with an average grain size of 68 μm formed elongated grains with an average length and width of 165 μm and 110 μm, respectively. These works indicate that a compositional gradient in DED-printed HEA products can be achieved from an iterative adjustment of the elemental powder ratio, which contributes to tailoring the microstructure of printed products and obtaining the desirable properties in the designated areas.

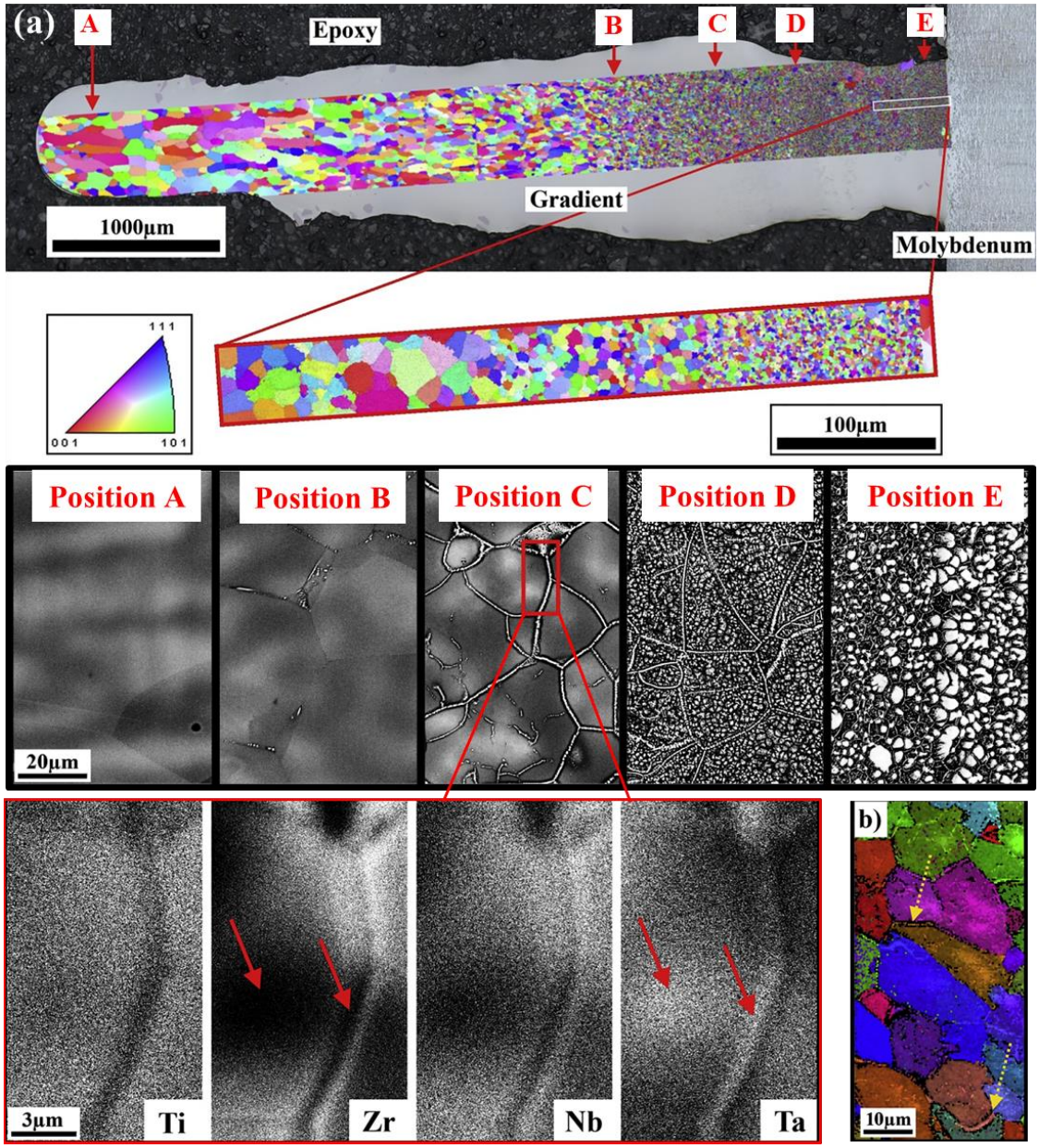

Figure 10. Microstructure of a graded $Ti_{25}Zr_{50-x}Nb_xTa_{25}$ HEA developed by DED: (a) color-coded grain orientation map from EBSD and enlarged backscattered electron images in

different positions, and (b) color-coded grain orientation map obtained by EBSD showing both the matrix and the secondary phase at the grain boundaries. From position A to E, *x* varied from 0 to 50. [149] Reproduced with permission.[149] Copyright 2019, Elsevier.

Besides, Welk *et al.* provided new insight to utilize DED to develop graded products from bulk metallic glass to HEAs.[158] Specifically, two products with compositional gradients, from $Zr_{57}Ti_5Al_{10}Cu_{20}Ni_8$ to $CoCrFeNiCu_{0.5}$ and from TiZrCuNb to $(TiZrCuNb)_{65}Ni_{35}$, were printed and characterized by different microstructures. The former exhibited a largely amorphous structure and the latter presented an amorphous matrix/crystalline dendrite structure. It was confirmed that the composition consisting of an amorphous matrix with a uniform distribution of crystalline particles could contribute to enhanced mechanical properties of the printed products.

The crystal features between HEA bulk products and HEA coatings prepared via DED are different. **Figure 11** compares typical microstructures of $Al_xCoCrFeNi$ HEA products and coatings with the same Al content (x = 0.3, 0.6 and 0.85).[153, 154] From **Figure 11**a and b, grains were columnar accompanied by a strong <001> fibre texture in the $Al_{0.3}CoCrFeNi$ and $Al_{0.85}CoCrFeNi$ products printed by Joseph *et al.*, but became dendritic or equiaxed with random crystallographic orientations in the $Al_{0.6}CoCrFeNi$ bulk product.[153] Nevertheless, the HEA coatings prepared by Chao *et al*. exhibited coarse columnar grains with a random crystallographic texture.[154] As the Al content increased, the average grain size decreased from 40.9 μm to 32.5 μm (**Figure 11**c and d). The microstructural difference was ascribed to the distinct printing conditions. The deposited zone of printed HEA products was subjected to a higher accumulated energy density and longer interaction time by successive layers, which exposed prior deposited layers to a short-time annealing. However, element segregation and phase separation were largely restricted in the HEA coating due to single layer deposition.

Efforts have been made to develop refractory HEA products using DED, such as MoNbTaW,[167] TiZrNbHfTa [168] and TiZrNbMoV [159] that are difficult to melt into

chemically homogeneous ingots. Besides, novel HEA composites have been developed using DED, such as AlCoCrFeCu with the addition of yttria partially stabilized ZrO_2 to reduce micro-cracks and refine microstructures,[155] CoCrFeMnNi with the additions of TiC [169] and WC [170] to improve its tensile strengths. Other examples of the phases and crystal features of DED-printed HEA products are summarized in **Table 5**.

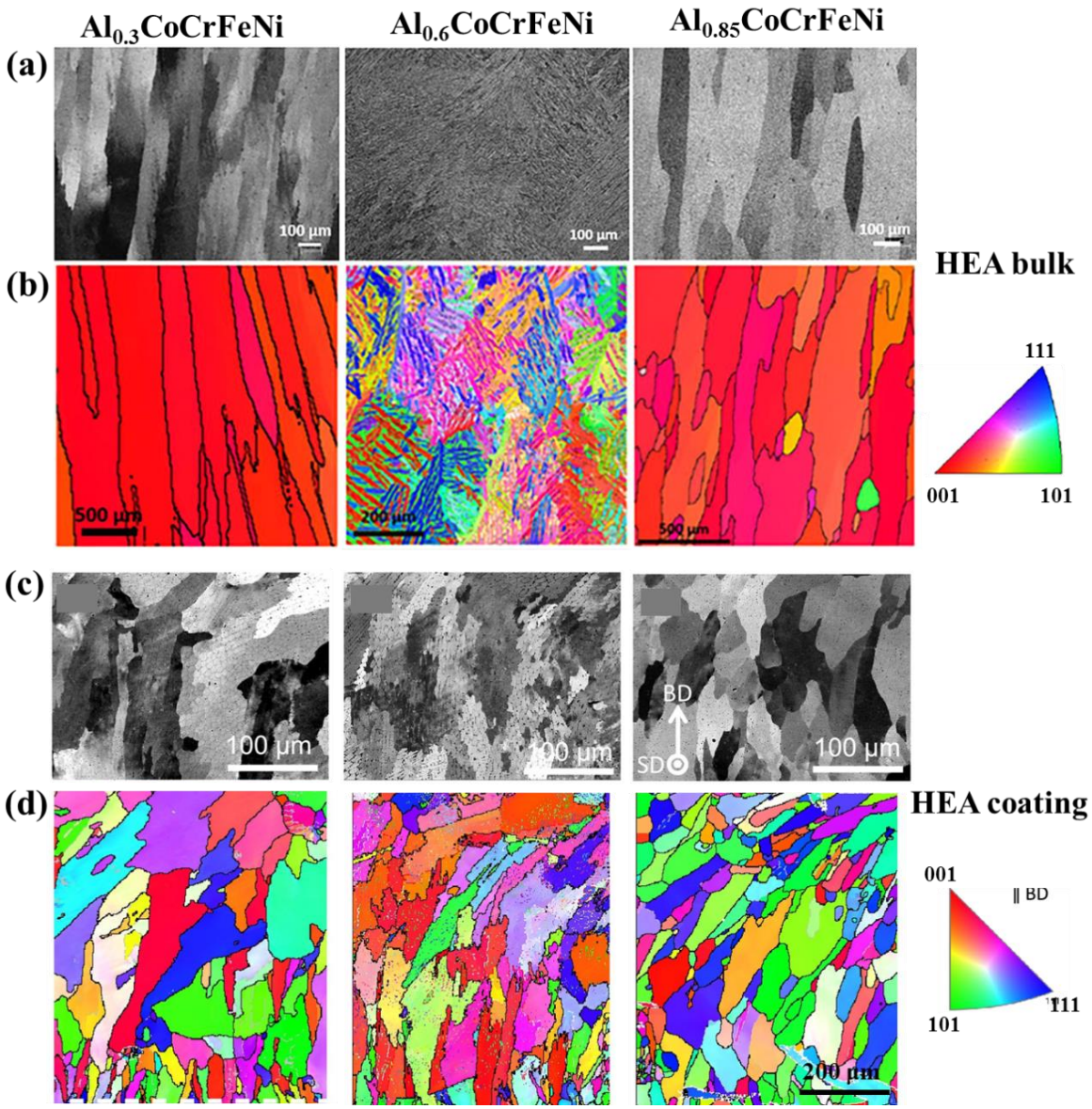

Figure 11. Comparison of the microstructures of DED-printed $Al_xCoCrFeNi$ HEA bulk products and coatings parallel to the build direction: (a) scanning electron microscope (SEM) images showing surface morphologies and (b) corrresponding inverse pole figure map of the products through EBSD,[153] (c) SEM morphology and (d) inverse pole figure map of the deposited coating.[154] Reproduced with permission.[153] Copyright 2015, Elsevier. Reproduced with permission.[154] Copyright 2017, Elsevier.

Table 5. Summary of phases and crystal features observed in various HEA products developed by DED.

HEA	Phase	Crystal features	Ref.
AlCoCrFeNi	B2	Periodic and fine grains consisting of ordered B2 phase	[150]
	BCC + B2	Columnar grains; equiaxed grains at the interlayer interface; grain sizes of 27.4–114.2 μm; disordered BCC precipitates in the ordered B2 matrix in the dendrites and interdendrites	[80]
$Al_xCoCrFeNi_{2-x}$	γ (x = 0.3)	Columnar grains with length greater than 1 mm	[164]
	γ + B2 (x = 0.7)	Dendritic structure	
	A2 + B2 + $L1_2$ (x = 1)	Equiaxed grains with alternating Fe-Cr and Al-Ni rich plates with $L1_2$ precipitates	
	A2 + B2 (x = 1.7)	Dendritic structure with alternating Fe-Cr and Al-Ni rich plates	
$Al_xCoCrFeNi$	FCC (x = 0.3)	Columnar structure with elongated grains longitudinal to the build direction and equiaxed grains transverse to the build direction; segregation of Al in grain boundaries	[153, 171]
	FCC + BCC (x = 0.6)	Widmanstätten grains with random crystallographic orientations	
	BCC (x = 0.85)	Columnar structure	
	FCC (x = 0.3)	Columnar grains with an average size of 40.9 μm; uniform cellular substructures with an average size of 5.7 μm in grains	[154]
	FCC + BCC (x = 0.6)	Columnar grains with an average size of 38.2 μm; a dispersion of FCC phase in the matrix of columnar BCC grains	
	BCC (x = 0.85)	Columnar grains with an average size of 32.5 μm; segregation of Cr and Fe in grain boundaries	
	FCC (x = 0.3)	Elongated grains	[165]
	FCC + B2 (x = 0.7)	FCC lamella widths of 2–3 μm	
$AlCo_xCr_{1-x}FeNi$	B2 (x = 1)	Columnar grains with an average size of 100 μm in length and 25 μm in width	[152]
	BCC + B2 + FCC (x = 0.8)	Equiaxed grains with an average size of 25μm; disordered BCC uniformly distributed within ordered B2 matrix; precipitation of disordered FCC phase in grain boundaries	
	BCC (x = 0.6)	Equiaxed grains with an average size of 25μm; A fine substructure in grains	
	BCC + B2 (x = 0.4)	Equiaxed grains with an average size of 40 μm; ordered B2 enriched in Al, Ni, and Co, disordered BCC enriched in Fe and Cr	
	BCC + B2 (x = 0.2)	Columnar grains with an average size of 150 μm in length and 240 μm in width	
	BCC + B2 (x = 0)	Columnar grains with an average size of 150 μm in length and 10 μm in width; ordered B2 enriched in Al and Ni, and disordered BCC enriched in Fe and Cr	

$Al_xCrCuFeNi_2$	FCC + BCC (x = 0)	Dendritic structure	[163]
	FCC (x = 0.4)	Dendritic structure; cellular boundary structure with fine precipitates; segregation of Cu in to interdendritic regions	
	FCC + $L1_2$ + BCC + B2 (x = 0.8)	Dendritic structure with coarse and fine needle-like BCC/B2 precipitates	
	FCC + $L1_2$ + BCC + B2 (x = 1.0)	Equiaxed grains with coarse and fine needle-like precipitates	
	FCC + $L1_2$ + BCC + B2 (x = 1.3)	Large equiaxed grains of BCC/B2 with highly refined intragranular precipitates of FCC/$L1_2$	
	FCC + BCC + B2 (x = 1.5)	Fine-scale equiaxed grains; eutectic mixture of BCC and B2 phases; FCC precipitates	
$Al_xCoFeNiCu_{1-x}$	FCC (x = 0.25)	Columnar dendritic grains	[172]
	FCC (x = 0.5)	Columnar dendritic grains	
	FCC + BCC (x = 0.75)	Dendritic FCC structure enriched in Co and Fe; BCC matrix enriched in Al and Ni	
$AlCrFeMoV_x$	BCC (x = 0.3 at%)	Equiaxed grains with an average size of 68 μm	[156]
	BCC (x = 10 at%)	Elongated grains with an average size of 127 μm in length and 56 μm in width	
	BCC (x = 18.5 at%)	Elongated grains with an average size of 165 μm in length and 110 μm in width	
CoCrFeMnNi	FCC	Fine cellular dendrite structure with sizes of 2.9–5.2 μm	[157]
		Columnar and equiaxed grains	[173]
		Equiaxed grains with an average size of 3.68 μm and dendritic columnar grains with an average size of 3.11 μm in width; grain boundaries enriched in Mn and Ni	[174]
		Columnar grains with an average size of 13 μm and micro-sized cellular substructures	[175]
TiZrNbTa	BCC	From equiaxed grains to elongated grains along with grain sizes of 2–60 μm	[149]
TiZrNbHfTa	BCC	Equiaxed grains with random orientations	[168]
TiZrNbMoV	BCC + $NbTi_4$	Dendrites composed of BCC and $NbTi_4$-type phases with Zr-rich precipitates; no dendritic segregation	[159]
ZrTiVCrFeNi	C14 + αTi	Irregular cell-like structure with an average grain size of 50 μm	[160]
$La_{0.1}Ni_{0.5}Fe_{0.1}V_{0.1}Mn_{0.2}$	FCC + La(Ni, Mn)$_5$	FCC dendritic microstructure	[161]
$La_{0.03}Ni_{0.17}Fe_{0.2}V_{0.2}Mn_{0.4}$	σ + La(Ni, Mn)$_5$	Granular La(Ni, Mn)$_5$ precipitates; (V, Mn)-rich needle-like precipitates in the σ matrix	
$AlCoCrFeCu/Y_2O_3/ZrO_2$	I + $AlCu_2Zr$ + Amorphous	Block-shape crystalline phases composed of ultrafine nanocrystals	[155]

3.2. SLM

SLM, one of the PBF printing processes, is characterized by melting metal powders on a powder bed using a high-energy laser to print geometrically complex products.[176-184] A major difference between DED and SLM is the way powders are fed. In SLM, HEA powders are spread on the building platform by a rake rather than being blown from the nozzles in the case of DED. A focused laser beam selectively melts the powders in the printing layer according to a predefined path, and non-melted powders are remained in the powder bed to support subsequent printing layers. After solidification of the printing layer, the fabrication piston depresses the foundation by the thickness of a singer layer to provide space for the new layer, and powder spreading and melting are repeated, as schematized in Figure 7b. The melting of each layer is followed by rapid solidification at the rate of 10^6–10^8 K/s,[36] leading to unique refined microstructures of printed HEA products.

SLM has been introduced to print HEA products using the developed HEA powders, due to its capability to produce complex components with outstanding mechanical properties.[185, 186] For example, Brif *et al.* initiated the work on SLM-printed CoCrFeNi HEA products with a combination of high strength and ductility.[187] The printability of SLM for HEA powders can be evaluated through the investigation of a single track, a single layer and multiple layers. In the study of Piglione *et al.*,[188] the single track of CoCrFeMnNi exhibited multiple grains that grew epitaxially from existing grains in the substrate, with cell axes perpendicular to the fusion line. These grains were found to have both their cell axes and one <001> orientation aligned in the direction of maximum heat flux (**Figure 12**a and b). However, the grains in the multi-layer build showed columnar grains with <001> and <011> orientations and reduced grain numbers (Figure 12c and d). Each solidified melt pool in the multi-layer build experienced a remelting process when the laser melted adjacent tracks and successive layers, promoting grain selection via competitive growth.

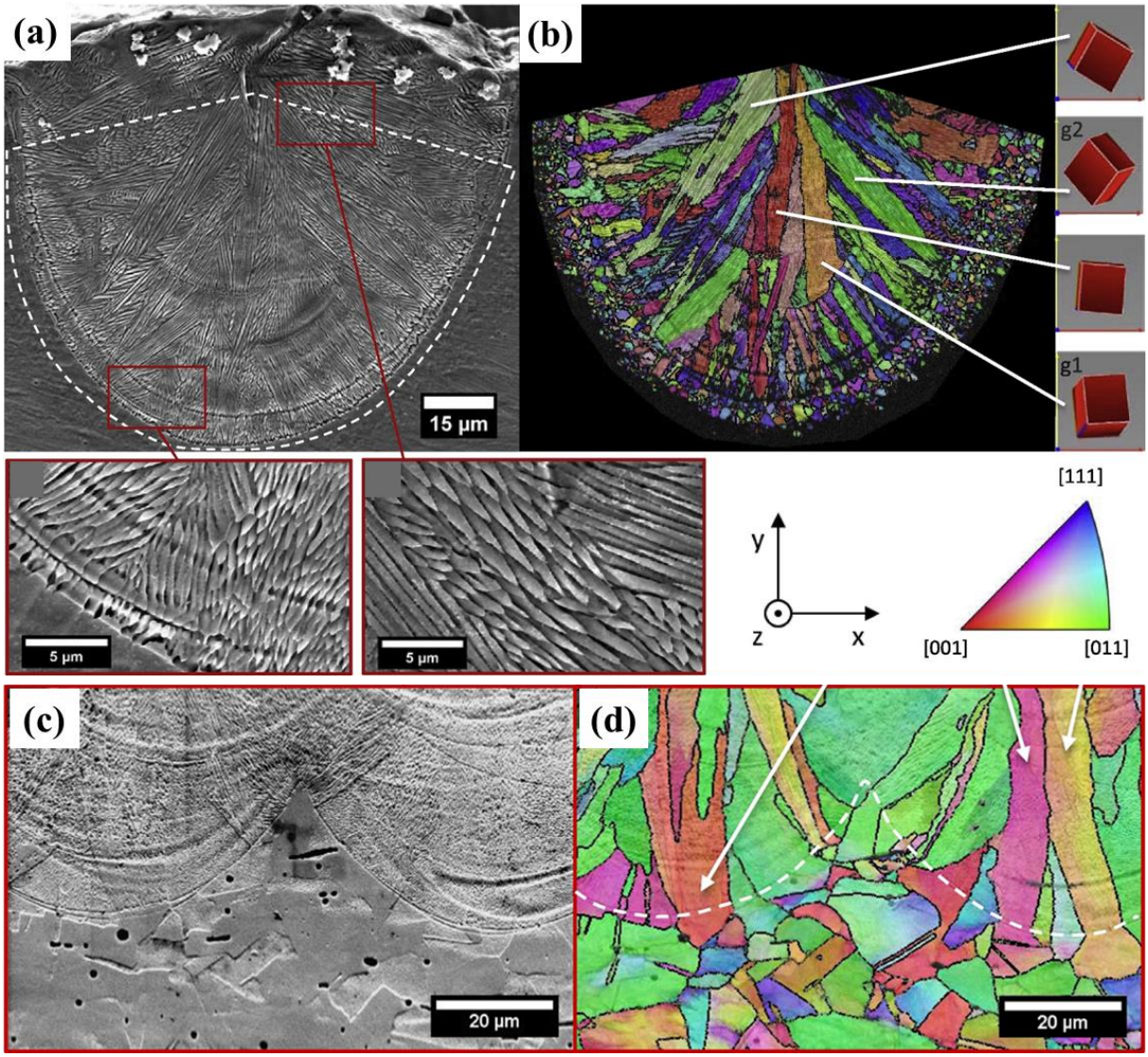

Figure 12. (a) Microstructure and (b) inverse pole figure map of the cross section of one track in the single-layer build produced by SLM from a CoCrFeMnNi HEA powder through EBSD measurement; the cubes showed the crystallographic orientations of selected grains, (c) microstructure and (d) inverse pole figure map of the cross-section in the multi-layer build.[188] Reproduced with permission.[188] Copyright 2018, Elsevier.

Even small changes in the composition of printed materials can result in significant changes in process parameters corresponding to successful printing. Therefore, Johnson *et al.* proposed a methodology for predicting the printablity of a CoCrFeMnNi HEA powder using SLM with melt pool geometry-based criteria.[189] Threshold values of L/W, W/D and D/t were used to define the space of process parameters, where L, W and D correspond to the length, width and depth of the melt pool, respectively, and t corresponds to the powder bed layer

thickness. The values of L/W ranging between $2 < L/W < \pi$ were related to the balling phenomenon that is widely considered to be the result of Plateau-Rayleigh instabilities in melt pools. The threshold value $W/D > 1.5$ was a reasonable criteria for the keyhole phenomenon resulting from the vaporization of metal and subsequently the collapse of depression zones. The criteria of $D/t > 1.5$ was proposed for lack of fusion induced by the insufficient supplement of molten metal. This methodology provides a plausible route for the printing of HEA products with reduced sensitivity to the variability of SLM machines.

Sputtering is the ejection of molten metals from melt pools, which is a representative phenomenon during the SLM process. The metal vaporization caused by a high-energy input leads to a recoil force that overcomes the surface tension, which opposes the compressive effect of the recoil force, therefore creating the sputtering.[190] Sputtering is detrimental to the mechanical properties of SLM products and can potentially lead to their failure. Increasing the laser scan speed or decreasing the laser power can lead to the reduction in the sputtering; however, the process optimization by minimizing the laser energy to reduce the sputtering is ineffective in improving the mechanical properties of the products.[191] Besides, oxide layers tend to develop on the molten droplets upon ejection, increasing the mass and size of the sputtering particles.[192] Therefore, HEAs for SLM can be designed with a decrease in the ratio of volatile elements to reduce the recoil force and sputtering, a compensation of volatile elements to maintain chemical compositions of printed HEA products, and the avoidance of using elements that have high affinity to oxidize.

The laser volumetric energy density strongly influences the heat transfer and crystal growth during SLM, which can be defined by the equation $E = P/(vht)$, where P is the laser power, v the scanning speed, h the hatch space and t the layer thickness. Li *et al.* studied the effect of the laser energy density on the microstructural evolution of SLM-printed CoCrFeMnNi and AlCoCrFeNi HEA products.[90, 193] The increase of E from 37 J/mm^3 to 185 J/mm^3 did not change the FCC phase of CoCrFeMnNi but decreased its lattice parameter through the

vaporization of Mn. Besides, the increased energy density eliminated porosity and delamination between layers and strengthened the metallurgical bonding between neighboring layers of the products. High cooling rates in SLM led to large degrees of undercooling within melt pools, thus resulting in the sub-micro cellular grains in the CoCrFeMnNi HEA products (**Figure 13**a). Figure 13b and d show the high-density dislocation pile-up and dislocation entanglement. In particular, a primary FCC phase and a tetragonal σ precipitate phase with an orientation relationship [011]FCC // [167]σ were identified (Figure 13c). Another notable observation was the existence of nano-twins in the printed HEA with stacking faults nearby (Figure 13e and f). Similar characteristics were observed in other studies on the printing of CoCrFeMnNi HEA products,[92, 173] which additionally proposed a hierarchical microstructure consisting of columnar grains, submicron cellular structures, dislocation networks and nano-sized oxides.[194]

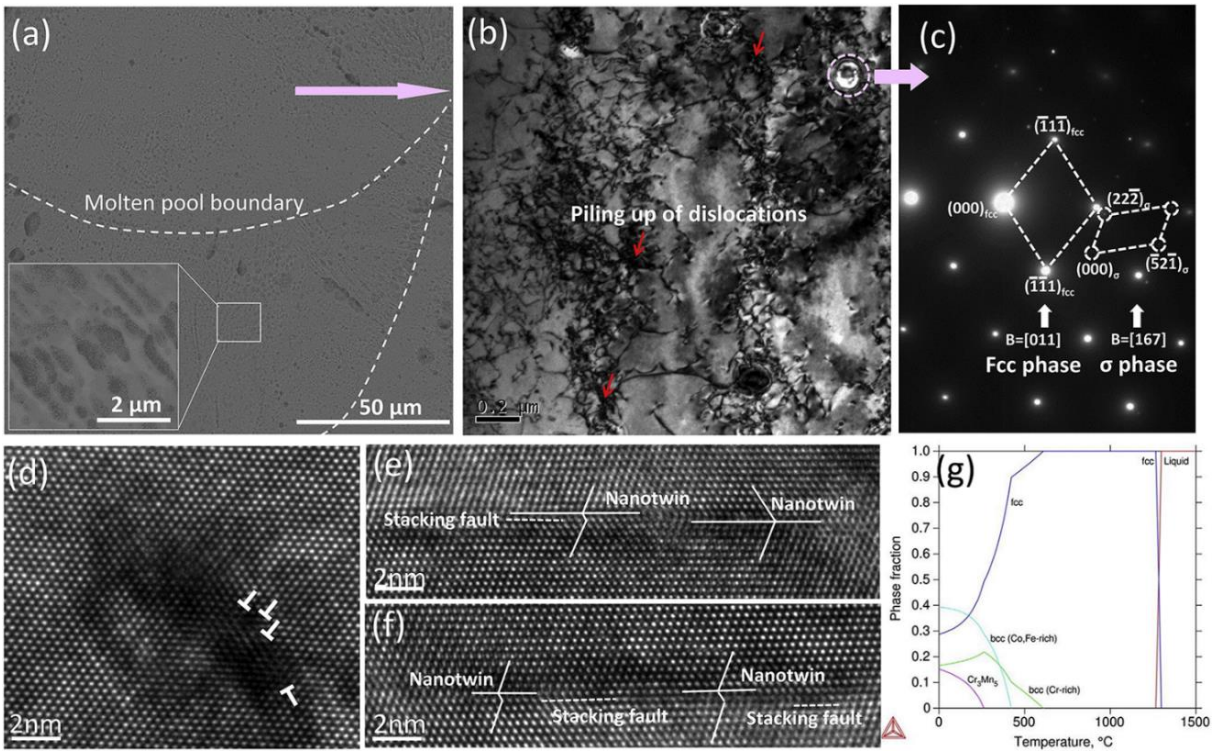

Figure 13. Microstructure of SLM-printed CoCrFeMnNi HEA products: (a) SEM image showing the melt pool boundary and sub-micro cellular grains, (b) TEM bright field showing high density of dislocation piled up and dislocation network, (c) selected area diffraction pattern showing FCC phase and σ precipitate phase, high-resolution transmission electron microscopy images showing (d) dislocations and (e, f) nano-twins coupled with stacking

faults, and (g) calculated equilibrium phase fractions.[90] Reproduced with permission.[90] Copyright 2018, Elsevier.

The relative densities, phases and crystal features of SLM-printed HEA products are summarized in **Table 6**. The SLM-printed HEA products can achieve a relative density of 99.7% using optimized process parameters. However, it is difficult to optimize process parameters of SLM for newly developed HEA powders. Zhou *et al.* proposed a universal model to predict the laser energy density required to achieve near-fully dense parts using SLM, considering the powder surface, porosity of the powder bed, vaporization and heat loss.[207] This model, which provides a practical approach to estimate the optimized laser energy density for the printing of HEA powders, was then validated through the printing of a CoCrFeMnNi powder. A guideline on the composition design of HEAs for SLM can be provided based on the developed model. The energy absorption Q_a by the local powder bed should be 3–8 times greater than the energy consumption Q_c to achieve HEA products with near-full density using SLM. The value of Q_a/Q_c highly depends on laser absorptivity, latent heat of melting and specific heat capacity of designed HEAs. Besides, transition and basic elements, such as Al, Co, Cr, Fe, Ni, Mn, Ti, Cu, Mo, Nb, Ta and W, can be recommended for the design of HEAs for SLM through various combinations and proportions. However, alkaline earth metals and non-metals are not included.

A comparison of the microstructures of AlCoCrFeNi HEA products printed by SLM and casting was conducted by Karlsson *et al*.[195] The SLM-printed HEA product had a different microstructure compared to its casted counterpart (**Figure 14**a and b), which was attributed to the higher cooling rate of SLM. The grain sizes of the SLM product were much finer (less than 20 μm). Both SLM-printed and casted products showed a dendritic structure, in which a fine-structure with small domains existed, but SLM produced finer structures with BCC and B2 domains in the range of 20–30 nm.

Table 6. Summary of relative density, phase and crystal features in SLM-printed HEA products.

HEA	Relative density (%)	Phase	Crystal features	Ref.
$Al_{0.5}CoCrFeNi$	-	FCC	Coarse columnar grains and fine equiaxed grains	[85]
AlCoCrFeNi	98.4	A2 + B2	Epitaxial growth of columnar A2 grain bundles perpendicular to the melt pool boundary with an average grain size of 1.5 μm; the B2 phase is between A2 grains; Precipitates enriched in Fe and Cr	[193]
	-	A2 + B2	Elongated grains with an average size less than 20 μm; B2 subgrains with sizes of 20–30 nm	[195]
AlCoCuFeNi	-	B2	Fine columnar grains located along melt pool boundaries in the <001> orientation and equiaxed grains at the centre of melt pools with <001> and <101> orientations; an average size of 10 μm for B2 subgrains	[196]
AlCrCuFeNi	99.7	A2 + B2	Fine columnar grains consisting of ultrafine subgrains with a <100> preferred orientation; precipitation of nano-scale Cu-rich phases with chain-like and granular shape	[197]
$Al_{0.26}CoFeMnNi$	99.5	FCC	Microstructure enriched in Co, Fe, and Ni under low energy densities	[198]
$AlCoFeNiSm_{0.1}TiV_{0.9}$	-	FCC	Uniformly distributed equiaxed grains with random orientations; no element segregation	[199]
CoCrFeNi	-	FCC	Fine grains with dissimilar crystallographic orientations	[187]
	98.7	-	Epitaxial growth of columnar grains with an average size of 3 mm in length and 200 μm in width	[200]
CoCrFeMnNi	98.2	FCC + σ	Epitaxial growth of grains to form elongated columnar grains with a <001> orientation parallel to the build direction	[90]
	-	FCC	Epitaxial growth and competitive grain growth	[188]
	99.2		A hierarchical microstructure with columnar grains along the build direction and a typical submicron cellular structure	[92]

	-		A hierarchical microstructure with epitaxial growth of grains with sizes of 5.98–15.66 μm; cellular- and columnar-type structures within the grains	[194]
	-		Elongated grains with a preferred growth <001> direction along the build direction	[201]
$CoCrFeNiC_{0.05}$	99	FCC	Fine columnar-like grains with sizes of 40–50 μm; cellular and columnar subgrains with an average size of 500 nm; precipitates enriched in C and Cr	[202]
$Co_{1.5}CrFeNi_{1.5}Ti_{0.5}Mo_{0.1}$	99.3	FCC + Single cubic + HCP	Fine uniform microstructure with no visible segregations	[203]
MoNbTaW	-	BCC	Lamellar martensite structure dendrites with the primary and secondary dendrite arm spacings of 6.59 and 1.68 μm, respectively	[204]
$Ni_6Cr_4WFe_9Ti$	-	FCC + Unknown phase	Columnar dendritic and fine equiaxed dendritic structures; tiny precipitates (unknown phase) with sizes of 30–50 nm dispersed on intragranular boundaries	[205, 206]

Figure 14c and d reveal the formation of (Cr, Fe)-rich phase and (Ni, Al)-rich phases in the casted HEA product but not in the SLM-printed one. Moreover, anti-correlated fluctuations between Cr and Fe as well as Cr and Co were found in the (Cr, Fe)-rich phase, which proved a further element segregation to Cr-rich and Fe-rich regions (Figure 14f). However, fluctuations in the elemental distribution, predominantly for Cr, was found in the SLM-printed product (Figure 14e), which indicated a spinodal decomposition process. Similarly, Niu *et al.* observed no precipitates enriched in Cr existing in the SLM-printed product, even though various energy densities were used.[193] Besides, the printed product consisted of BCC + B2 and BCC + A2 phases. The epitaxial growth of A2 grain bundles was perpendicular to the melt pool boundary, and the B2 phase appeared between the columnar A2 grains.

Besides, Zhou *et al.* developed novel $FeCoCrNiC_{0.05}$ HEA products using SLM, and found that the density and grain size increased with the laser power and the decrease in the scanning speed.[93] **Figure 15** shows the different crystal features exhibited along the build direction of SLM. It was attributed to the inhomogeneous temperature distribution and the existence of a temperature gradient, which was demonstrated through numerical simulations on the temperature distribution in melt pools.[208] The printed $FeCoCrNiC_{0.05}$ HEA products obtained grains with random orientations in three different regions along the build direction (Figure 15a). Figure 15b reveals the high level of local deformations, leading to strain concentration and the occurrence of microcracks.

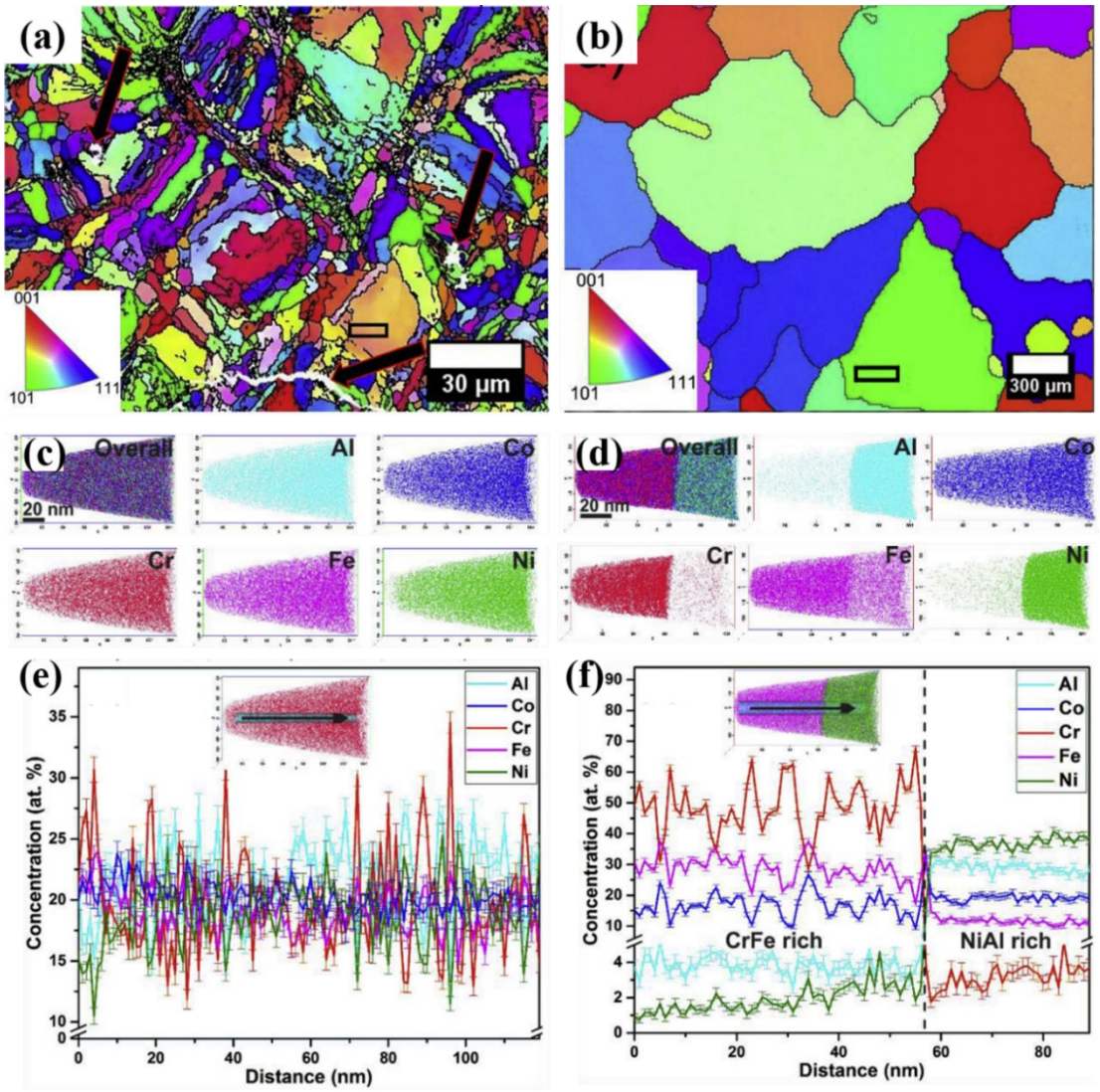

Figure 14. Comparison of microstructure between the SLM-printed AlCoCrFeNi HEA product and the casted counterpart: EBSD images of (a) SLM-printed product and (b) casted counterpart; atom probe tomography analysis showing three-dimensional distribution of Al, Co, Cr, Fe and Ni atoms of (c) SLM-printed product and (d) casted counterpart, one-dimensional concentration profile of elements taken along the cylinder of (e) SLM-printed product and (f) casted counterpart.[195] Reproduced with permission.[195] Copyright 2019, Elsevier.

Equiaxed grains existed mostly in the middle and bottom regions, while columnar grains were dominant in the top region and exhibited fewer grain boundaries (Figure 15c). Similar to DED, the solidification mode and microstructure fineness are dependent on *G* and *R*. The *G*/*R* ratio determines the stability of the solidification front and solidification mode. The following types of structures are expected to form as the *G*/*R* ratio decreases: planar, cellular, columnar

dendritic and equiaxed dendritic. As the SLM process proceeded, the heat transfer slowed down and *R* decreased. The value of *G*/*R* in the top region was higher than that in the bottom and middle regions, which contributed to the grain growth and coarser grains in the top region.

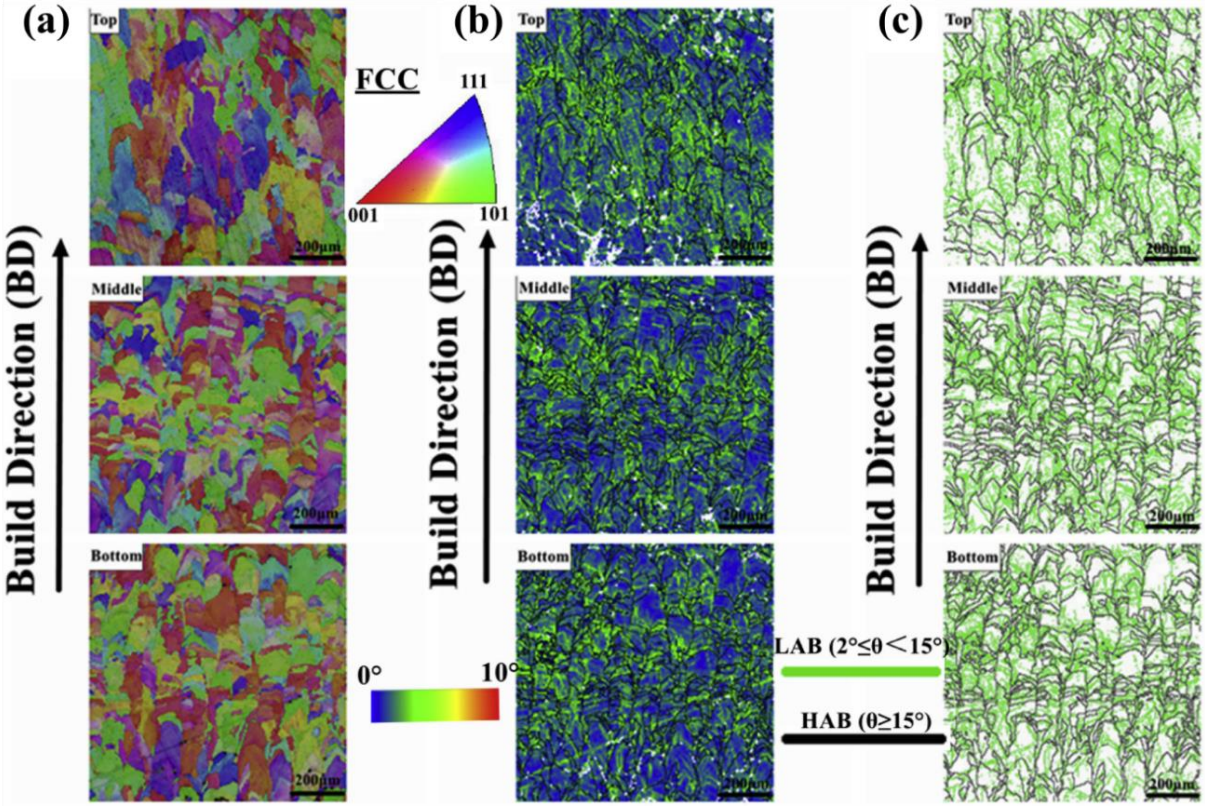

Figure 15. EBSD analyses in different regions of SLM-printed $FeCoCrNiC_{0.05}$ HEA products: (a) inverse pole figure, (b) local misorientation maps, and (c) grain boundary maps.[93] Reproduced with permission.[93] Copyright 2018, Elsevier.

Notably, Sun *et al.* found that intergranular hot cracks were present, which were independent of the processing parameters used for printing CoCrFeNi HEA products, suggesting poor laser-based printability for this HEA powder.[200] The products printed using chessboard and stripe strategies (**Figure 16**g and h) exhibited coarse-grained microstructures with a number of intergranular cracks, as illustrated in Figure 16c–f. Columnar grains epitaxially grew up to 3 mm in length and 200 μm in width, but the growth broke down in the periphery of the lack-of-fusion cracks. Both products exhibited a strong <011> crystallographic texture. The majority of misorientations of the adjacent grains were located between 40° and 50°. Furthermore, element segregation did not exist at the grain boundaries

that favored hot cracking (Figure 16i and j). Severe residual stresses induced by the large grain sizes was the root cause for the intergranular cracking. Therefore, fine-grained microstructures offer sufficient grain boundaries to withstand the residual stresses and help minimize hot cracking.

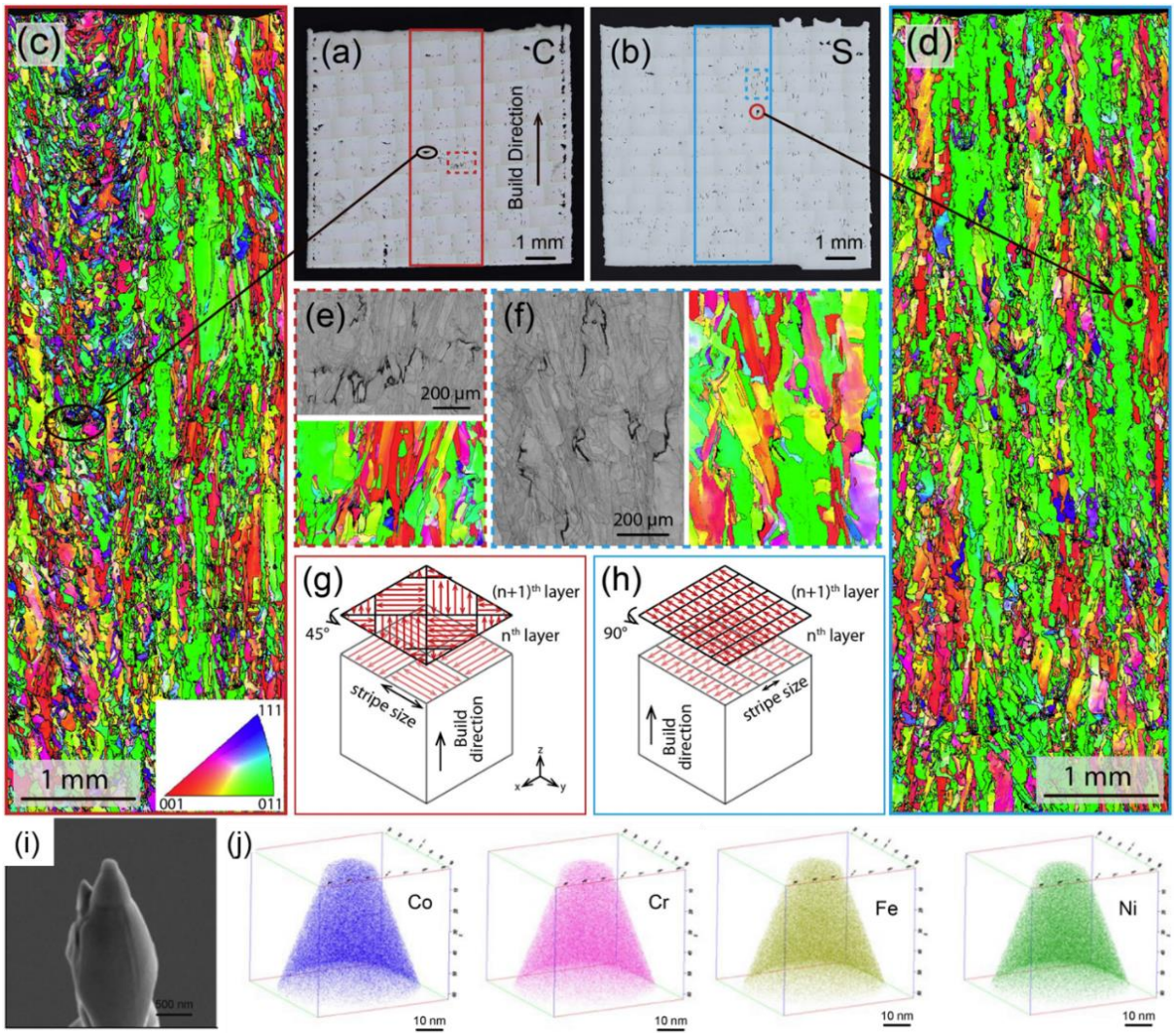

Figure 16. Optical microscope images of SLM-printed CoCrFeNi HEA products with (a) chessboard (denoted as C) and (b) stripe (denoted as S) scanning strategies; EBSD inverse pole figure maps with respect to the build direction of the selected areas for (c) C product and (d) S product; Enlarged EBSD band contrast images and inverse pole figure maps showing intergranular cracks within (e) C product and (f) S product; schematic illustrations of scanning strategy of SLM: (g) chessboard and (h) stripe; (i) SEM image showing a tip of atom probe tomography specimen with a dimension of 50 nm, and (j) atom distribution of the constituting elements.[200] Reproduced with permission.[200] Copyright 2019, Elsevier.

Li *et al.* developed a cemented carbide system with an AlCoCrFeNiCu HEA as a binder to consolidate a casted tungsten carbide via SLM.[86] A fine W_2C/HEA dendritic structure could be identified in melt pools. The W_2C dendrite was primarily formed and followed by rapid solidification of the remaining melt pools as the interdendritic FCC phase. The W_2C/HEA dendritic structure was then repeatedly heated by iterative laser scanning, which led to the precipitation and coarsening of faceted WC from the W_2C dendrite. The HEA could not hinder the uneven growth of carbides during SLM as a binder.

The surfaces of SLM products often need to be processed to improve their quality and dimensional accuracy for industrial applications. Guo *et al.* reported a pioneering work on the machinability study of SLM-printed CoCrFeMnNi HEA products by mechanical, thermal and electrochemical machining processes, such as milling, grinding, wire electrical discharge machining (EDM) and electropolishing (EP).[209] These processes created various surface morphologies and roughness, residual stresses and subsurface quality, as presented in **Figure 17**. The milling and grinding smoothed the surfaces without subsurface damages, but induced tool marks and compressed residual stresses were caused by the deformation of microstructures. Wire EDM flattened the surfaces but resulted in the increase in tensile residual stress. Followed by EP, the as-printed, mechanical and thermal processed surfaces obtained better surface finishes. Among these techniques, EP and mechanical polishing can be adopted to reduce subsurface damage and further improve the surface quality of the products.

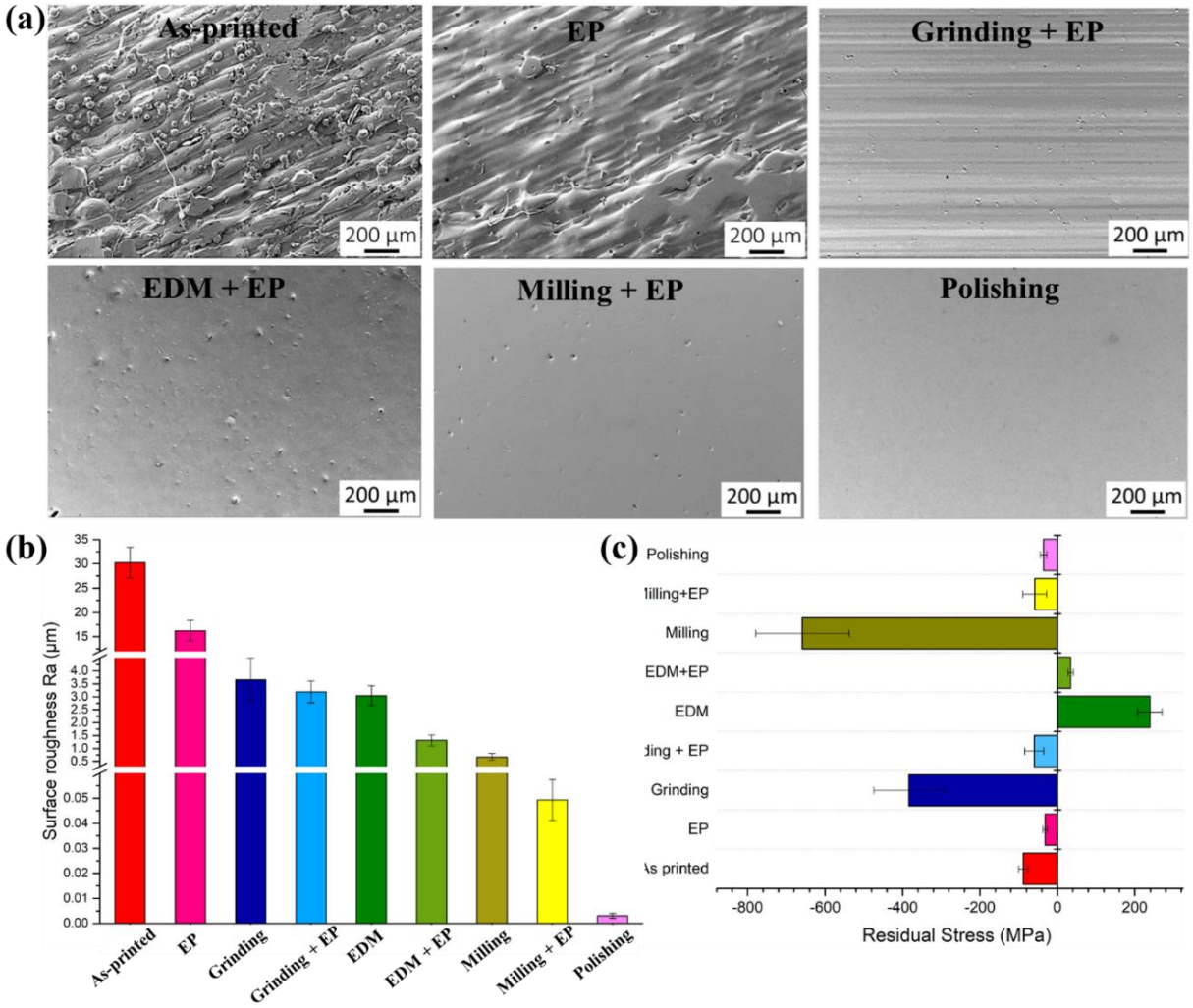

Figure 17. Surface characteristics of SLM-printed CoCrFeMnNi HEA products with different machining processes: (a) secondary electron images of typical surface morphologies, (b) surface roughness, and (c) residual stresses.[209] Reproduced with permission.[209] Copyright 2018, Elsevier.

3.3. EBM

EBM uses an electron beam to melt metal powders,[210] and its schematic is presented in Figure 7c. Due to the special operating environment of the electron beam, EBM fabricates components in a high-vacuum environment of 10^{-4} mbar or greater, offering an ideal contamination-free environment for manufacturing. It has a similar working principle to SLM but different working conditions. The preheating of the powder bed by the electron beam at a temperature up to 750 °C before the scanning and melting is a distinctive procedure in EBM to reduce the thermal gradient in printed products. The scanning speed of EBM is usually two

orders of magnitude lower than that of SLM.[211] The lower cooling rate and smaller temperature gradient in EBM contribute to the reduction of residual stresses, distortion and cracking tendency.[212]

The AlCoCrFeNi HEA products printed by EBM were first developed in the study by Fujieda *et al*.[81] Their following works exhibited similar phase components but different microstructures in the top and bottom regions of the HEA (**Figure 18**), due to different temperature distributions induced by preheating and heat transfer.[83] B2 + BCC phases with FCC precipitates were identified. The (Al, Ni)-rich and (Cr, Fe)-rich phases corresponded to the B2 and BCC, respectively. Preheating at 950 °C resulted in the formation and precipitation of the FCC phase at the grain boundaries of B2 and BCC. Since the FCC phase in an equilibrium condition was approximately 20 %, the top region was in a non-equilibrium condition with 7.1 % FCC while the bottom reached an equilibrium condition with 29.7 % FCC. The reduced temperature gradient through preheating promoted the phase transformation from the BCC to FCC. On another note, a modulated structure within equiaxed grains was observed both in top and bottom regions, but the abundance of equiaxed grains was greater at the bottom. The regional difference within the microstructure was attributed to the difference in the exposure time at the preheating temperature.

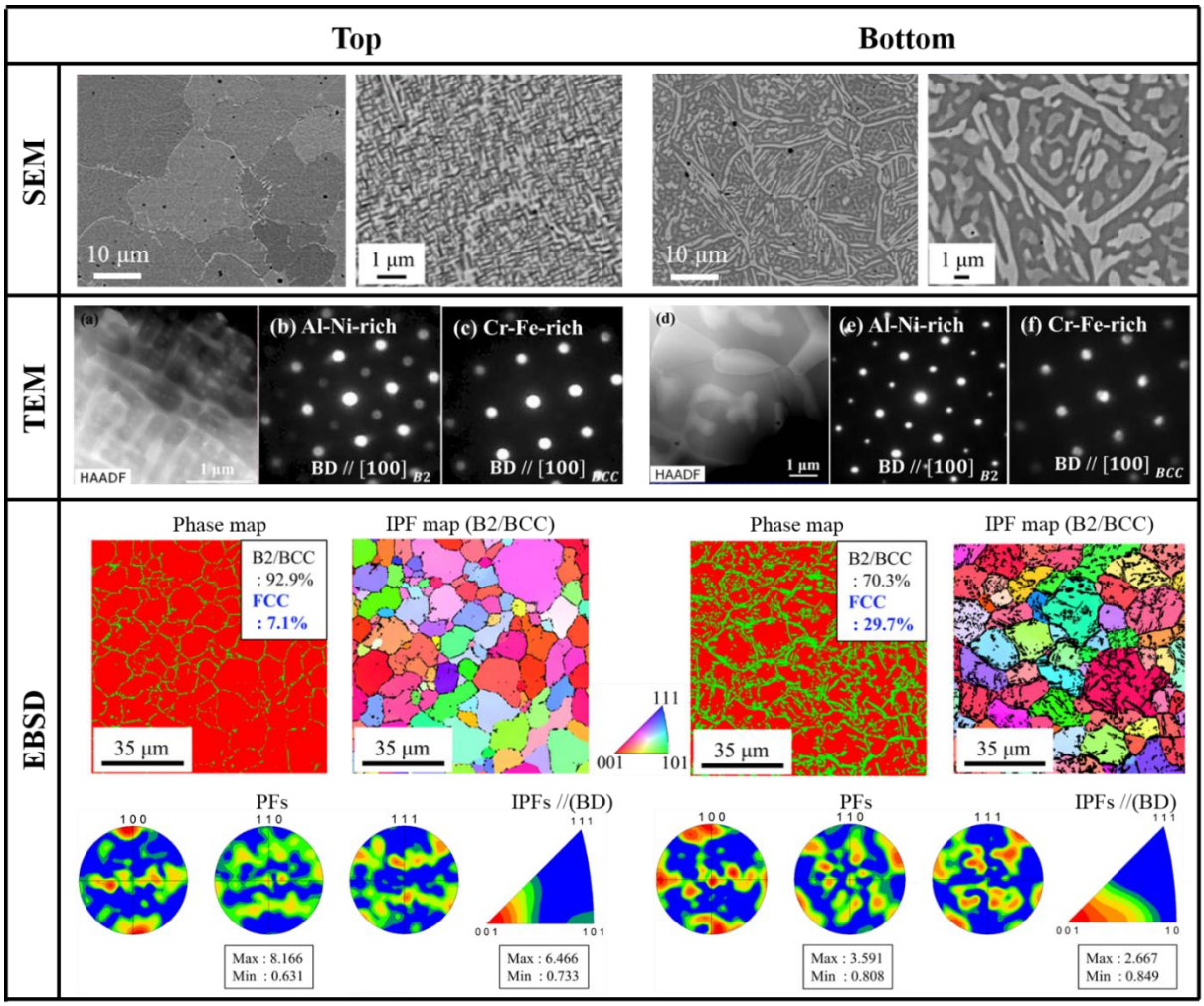

Figure 18. Phase and microstructural characteristics of EBM-printed AlCoCrFeNi HEA products at top and bottom regions from TEM, SEM and EBSD measurements.[83] Reproduced with permission.[83] Copyright 2016, Elsevier.

Attempts have been made to develop novel HEA products based on the CoCrFeNiTi system.[213] The EBM-printed $Co_{1.5}CrFeNi_{1.5}Ti_{0.5}Mo_{0.1}$ HEA products with a relative density of 99.4% were investigated in comparison to SLM-printed counterparts.[203] Both of the products exhibited single cubic and FCC phases, but Ni_3Ti brittle intermetallic compounds precipitated solely in the EBM-printed one. It was ascribed to the much lower cooling rates (10^3-10^5 K/s) derived from the preheating and larger melt pool sizes in EBM,[214] which provided sufficient time for precipitation to occur. In addition, there was a difference of columnarization for crystal grains and anisotropy between EBM- and SLM-printed HEA products. The larger G/R ratio in EBM inhibited the growth of equiaxed grains.[215]

Furthermore, this study demonstrated that solution treatments of water quenching (W.Q.) and air cooling (A.C.) for the printed products could effectively prevent the formation of intermetallic compound precipitates, as shown in **Figure 19**a. A fine particulate single-cubic-ordering phase was observed in the FCC matrix (Figure 19b). After the treatments, small particles with Ni and Ti concentrations existed in different sizes due to the distinction between the initial and final cooling rates of the system (Figure 19c and d). The spinodal decomposition progressed to a certain degree before the ordering phase precipitated.

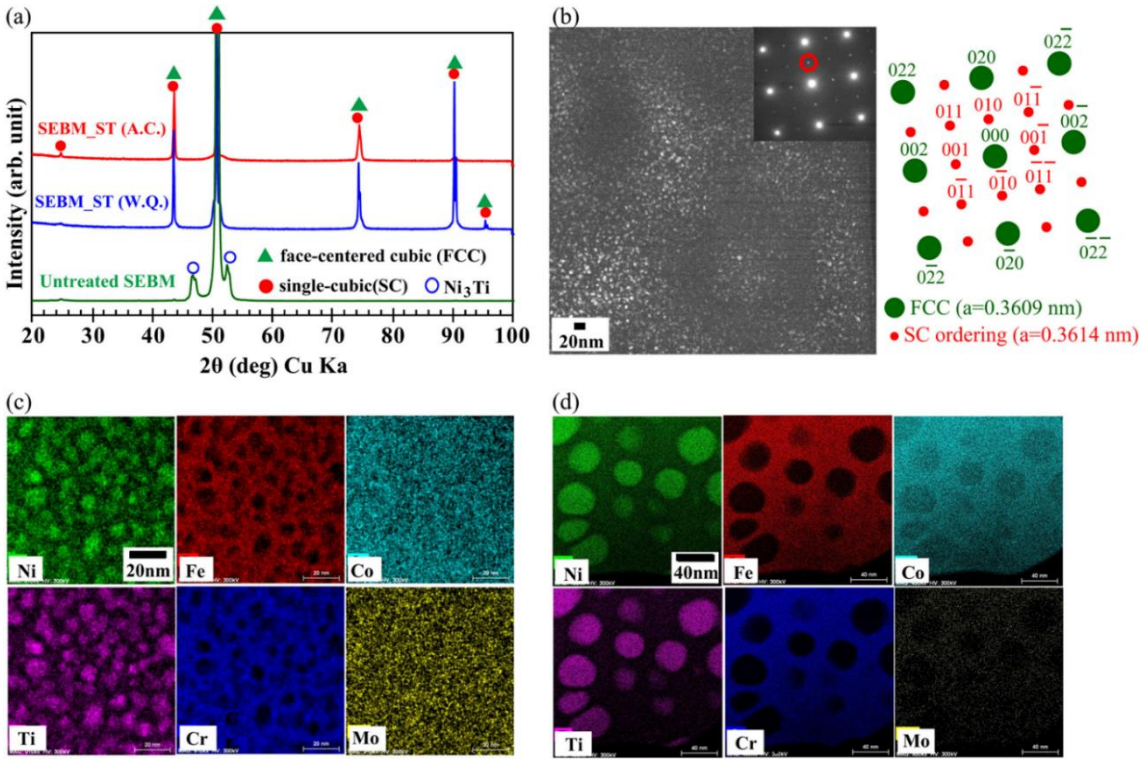

Figure 19. Effects of the solution treatments on the phases of EBM-printed $Co_{1.5}CrFeNi_{1.5}Ti_{0.5}Mo_{0.1}$ HEA products: (a) Phase identification of untreated and solution-treated products, (b) TEM dark field image and corresponding diffraction pattern of EBM products by W.Q., (c) and (d) elemental mappings of EBM products by W.Q. and A.C., respectively.[213] Reproduced with permission.[213] Copyright 2017, Elsevier.

Wang *et al.* performed the process optimization of EBM for CoCrFeMnNi products using a gas-atomized HEA powder.[75] The printed products achieved a relative density of 99.4%. These HEAs exhibited columnar grains with intragranular cellular grains along the build direction and a strong <100> texture. The columnar grains were a few millimeters in length

and had an average width of 65 μm, and the cellular grains obtained an average width of 2.9 μm. The Mn and Ni elements segregated into interdendrites and the Fe, Cr, and Co elements segregated into dendrites. It was highlighted that the surface quality was crucial for reproducible production and consistent metallurgical bonding. Through the process optimization, the level and smooth surfaces of printed HEAs could be obtained without swelling and pores. The swollen top surface was an after-effect of vigorous melt pool motion, which resulted from the temperature gradients, Marangoni convection and element vaporization. This implied that a large melt pool and high melting temperatures facilitated the formation of surface swelling and unevenness. Adjusting the line offset, focus offset, scanning speed, reference current and preheating temperature parameters could be effective in maintaining the same melting conditions under similar energy inputs for fully melted HEA products with homogeneous top surfaces.

It is challenging to manufacture of HEA products through the *in situ* alloying of at least four pre-mixed constituent elemental powders using EBM and SLM. The distribution of the elemental powders in each printed layer will be inhomogeneous during the powder spreading, and rapid solidification of the melt pools will inhibit sufficient convection and diffusion of elements. These will cause chemical inhomogeneity in the layers and consequently microstructure inhomogeneity in printed products. A research work on $Al_{0.5}CrMoNbTa_{0.5}$ HEA products developed through the *in situ* alloying of blended elemental powders using EBM showed the formation of TaNbMo-based and $(TaMoNbCr)_{Al}$ solid solutions, but the microstructure homogeneity and mechanical properties of the HEA still needed to be investigated for a comprehensive understanding.[216] Furthermore, a recent study was conducted on the SLM of both $Al_{0.26}CoFeMnNi$ and $Al_{0.26}CoFeMnNiC_{0.12}$ HEA products using the blended elemental powders, indicating that the use of high energy densities contributed to enlarged melt pools and homogeneous element distributions inside.[198] However, these investigations are still limited and further explorations are required to validate

the effectiveness of printing HEA products via SLM and EBM through the *in situ* alloying approach.

3.4. Other processes

Attempts were made to explore other processes to print HEA products. Kenel *et al.* developed a low-cost non-beam method to print CoCrFeNi HEA products, based on the extrusion of inks containing inexpensive oxides (Co_3O_4 + Cr_2O_3 + Fe_2O_3 + NiO), followed by co-reduction and sintering.[217] **Figure 20** shows the phase evolution upon co-reduction of printed blended oxides by *in situ* synchrotron X-ray diffraction in H_2. An CoCrFeNi HEA with an FCC phase was obtained after the *in situ* co-reduction (Figure 20a). Upon the oxide co-reduction, the rapid sequential formation of Co, Ni and Fe was observed, while the Cr_2O_3 remained until its slow reduction above 1073 K (Figure 20b). The complexity of the phases upon co-reduction is illustrated in Figure 20c. Initial sequential reduction of NiO to FCC, of Fe_2O_3 to Fe_3O_4 and to FCC, and of Co_3O_4 to fine grained HCP with inter-dispersed stable Cr_2O_3 occurred between 573 and 673 K. At higher temperatures, the HCP transformed to FCC, and inter-diffusion led to the formation of additional FCC enriched in Fe and Ni and BCC enriched in Co and Fe. With the onset of Cr_2O_3 reduction at 1073 K, a fourth FCC phase appeared, consuming all other phases and became an FCC phase in the final CoCrFeNi HEA product.

Karthik *et al.* used friction deposition to print an Al matrix composite reinforced with nanocrystalline CoCrFeNi HEAs.[131] The printed HEA products exhibited fine, closely spaced, uniformly distributed, nanocrystalline reinforcement particles without any brittle intermetallic compounds. Karlsson *et al.* reported on binder jetting followed by sintering to develop AlCoCrFeNi HEA products with a porosity of ~1 %.[218] These explorations indicate the viability to print HEA products without the melting of powders by high-energy beams, which is beneficial in avoiding thermal stresses existing in DED- and SLM-printed HEA products, thus contributing to reduction in cracks and deformation. Currently, the HEA types

studied are still very much limited and a considerable of research is required to validate the reliability of these processes for printing HEA products.

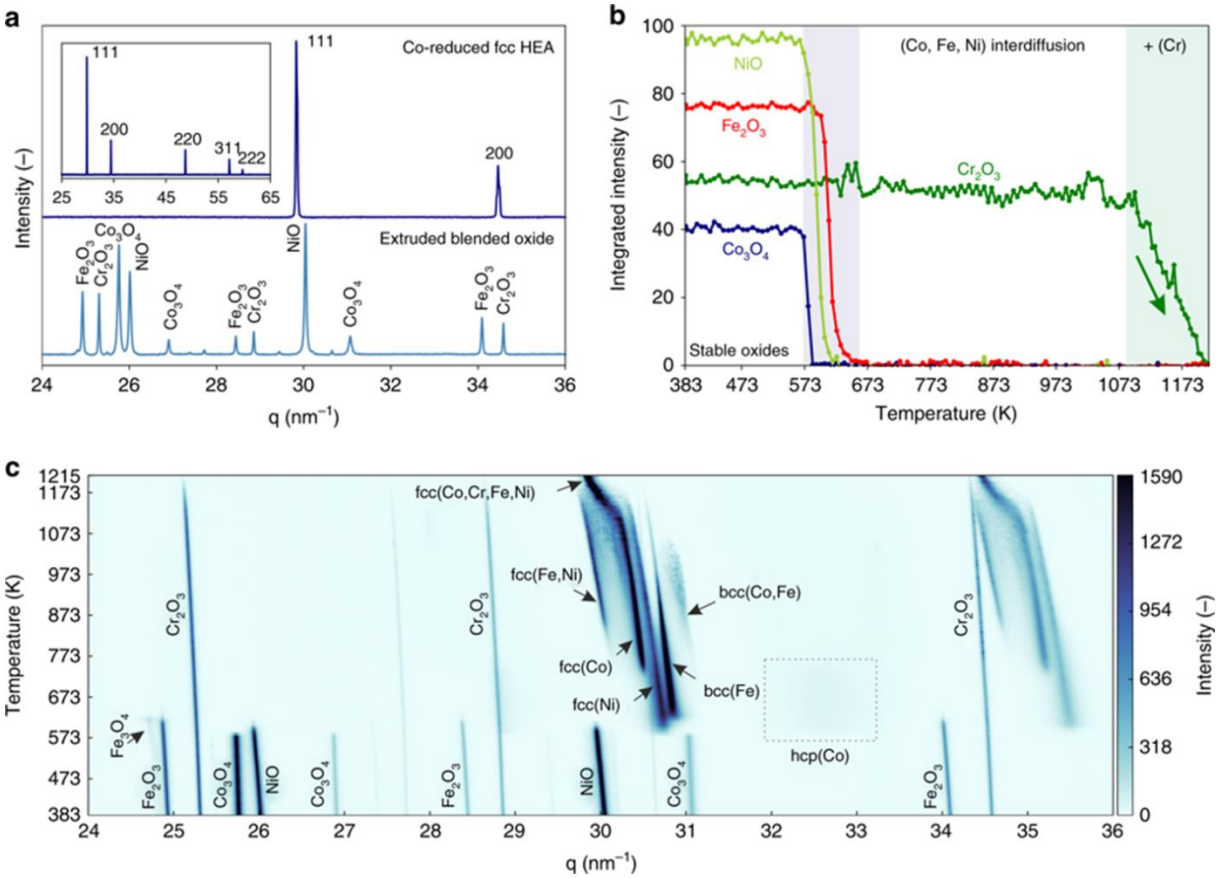

Figure 20. Phase evolution upon co-reduction of 3D-extruded blended oxides by *in situ* synchrotron X-ray diffraction in H_2: (a) X-ray diffraction diffractograms, (b) evolution of the integrated peak intensities for Co_3O_4, Cr_2O_3, Fe_2O_3 and NiO, demonstrating sequential reduction forming Co, Ni, Fe between 573 K and 637 K, followed by reduction of Cr_2O_3 between 1073 K and 1215 K, and (c) 2D phase evolution plot (temperature vs. the scattering vector *q*, with diffraction peak intensity as color map) upon heating and reduction, illustrating the complex pathway to form the CoCrFeNi HEA.[217] Reproduced with permission.[217] Copyright 2019, Nature Research.

In summary, DED and PBF (SLM and EBM) are major printing processes for HEA products, and DED is the most popular. The multi-powder delivery system enables DED to be a member of multi-material additive manufacturing community, which can realize the printing of hierarchical materials and functionally graded materials.[21] This holds promise for improving the performances of HEA products by increasing the complexity and functionality in user-definable locations. Compared to PBF, the lower scanning speed in DED results in a

lower crystal growth rate and cooling rate, which leads to larger grain sizes in DED-printed HEA products. On another note, large temperature gradients exist in the melt pools of DED and PBF due to the highly localized heat input and short interaction time. The rapid heating and cooling rates cause high residual stresses in DED- and SLM-printed products. This dramatically affects the microstructure of the products, which in turn govern their macroscopic mechanical performances. Comparatively, EBM products show negligible residual stresses due to the preheating for powder layers, which is beneficial in reducing cracks in the final products.[32, 219]

A comparison of microstructures of AlCoCrFeNi and CoCrFeMnNi HEA products manufactured by both 3D printing and conventional processes is presented in **Table 7**. The 3D-printed HEA products possess finer grain sizes than casted ones, which contributes to the enhancement of mechanical properties. The ultrafine grains and a large number of dislocations in printed products provide an abundance of grain boundaries and enhance overall element diffusion, favoring the phase precipitation during the repeating thermal cycle process of layer-by-layer manufacturing. In particular, the preheating process in EBM provides the possibility to control the formation and the proportion of precipitated phases in the AlCoCrFeNi products. The hierarchical structures in the 3D-printed HEA products, including melt pools, columnar and dendritic grains, submicron cellular structures, and dislocations, potentially endows the products with an extraordinary combination of high strength and excellent ductility compared to those manufactured by conventional processes.

Table 7. Comparison of microstructures of typical HEA products manufactured by both 3D printing and conventional processes.

Manufacturing method		**AlCoCrFeNi**	**Ref.**
3D printing	DED	Ordered B2 + disordered BCC phases; grain sizes of 27.4–114.2 μm; BCC precipitates; (Al, Ni)- rich in B2 and (Cr, Fe)-rich in BCC	[80]
	SLM	Ordered B2 + disordered A2 phases; grain sizes less than 20 μm; BCC precipitates; (Al, Ni)- rich in B2 and (Cr, Fe)-rich in BCC	[193, 195]
	EBM	Ordered B2 + disordered BCC + FCC phases; an average grain size of 10 μm; FCC precipitates; (Al, Ni)- rich in B2 and (Cr, Fe)-rich in BCC	[83]
Conventional process	Cast	Ordered B2 + disordered BCC phases; an average grain size of 179.3 μm; BCC precipitates; Al and Ni segregated into dendrites, and Cr and Fe segregated into interdendrites	[80]
	Powder metallurgy	Ordered B2 + disordered BCC + FCC phases; grain sizes of 10–20 μm; B2 + σ precipitates	[220, 221]
Manufacturing method		**CoCrFeMnNi**	**Ref.**
3D printing	DED	FCC phase; columnar grain sizes with several hundred microns in length and 3.11 μm in width; Ni and Mn segregated into grain boundaries	[174]
	SLM	FCC phase; grain sizes of 5.98–15.66 μm; σ phase precipitate; Mn segregated into melt pools	[90, 194]
	EBM	FCC phase; cellular grains with an average size of 2.9 μm; Co, Cr and Fe segregated into dendrites, and Mn and Ni segregated into interdendrites	[75]
Conventional process	Cast	FCC phase; grain sizes greater than 1000 μm; Cr and Mn segregated into interdendrites	[222, 223]
	Powder metallurgy	FCC phase; an average grain size of 25 μm	[88]

4. Properties and applications of 3D-printed HEAs

Compared with conventional manufacturing processes, the rapid solidification in DED and PBF contributes to refined grain sizes and prevents of the formation of intermetallic compounds in printed HEA products, which holds great promise for practical applications. This section focuses on the mechanical, corrosion, magnetic and hydrogen storage properties of printed HEA products as well as their potential applications.

4.1. Mechanical properties

Regarding service quality and durability, the mechanical properties of a final product are the most important in deciding whether 3D printing can be implemented in lieu of conventional manufacturing processes. Phases play a crucial role in the mechanical properties of HEAs.[224, 225] For example, BCC-based HEAs exhibit high yield strength and limited plasticity, while FCC-based HEAs possess low yield strength and superb plasticity.[60] A comprehensive understanding of the mechanical properties of 3D-printed HEA products precedes the rational design of composition for potential applications.

3D-printed HEA products exhibit the microhardness ranging from 195 HV to 860 HV, as shown in **Figure 21**. Printed HEA products with FCC phases, such as CoCrFeNi, CoCrFeMnNi and $Al_{0.5}$CoCrFeNi, possess much lower hardness than those with the BCC phases. Especially, the WTaNbMo refractory HEA products possess the BCC phase with extraordinary high hardness, which results from heavy lattice distortion through the introduction of large atoms. Note that there is no significant difference in hardness between DED-, SLM- and EBM-printed AlCoCrFeNi HEA products. However, the AlCoCrFeNi, CoCrFeMnNi and TiZrNbHfTa products manufactured by 3D printing possess higher hardnesses than those fabricated by casting and powder metallurgy, due to the hard phases, residual stresses and refined grains. Zhang *et al.* found a decrease in the microhardness of SLM-printed AlCoCuFeNi HEA products after an annealing treatment at 900–1000 °C.[196] The large grain sizes obtained after annealing and the precipitation of the FCC phase from the BCC matrix were responsible for the reduction.

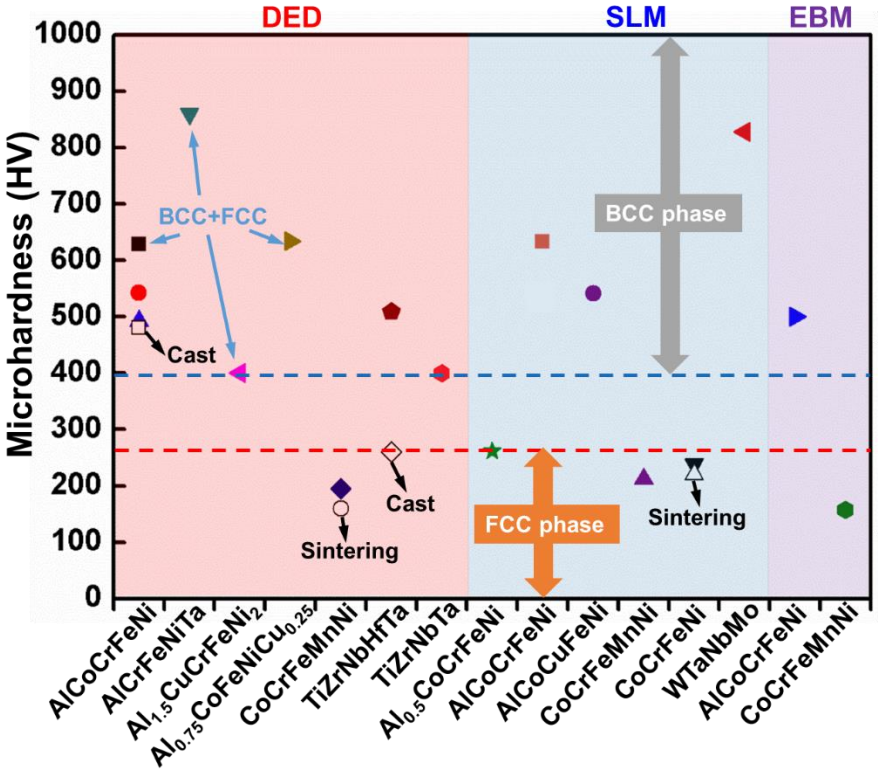

Figure 21. Microhardness of 3D-printed HEA products.[75, 80, 83, 85, 149, 151, 157, 163, 164, 168, 172, 187, 188, 193, 196, 207, 208] Typical HEA counterparts prepared by conventional manufacturing processes are contrastive.[88, 226, 227]

Table 8 provides a summary of tensile and compressive properties present in 3D-printed HEA products. The strength-ductility relationship of the printed products is illustrated in **Figure 22**. The wide ranges of strength and elongation are more dependent on the compositions of HEAs than on the process parameters in each printing process. The HEAs exhibit varying tensile yield strength from 194 MPa for an FCC-based microstructure to 773 MPa for a BCC- based microstructure. The SLM-printed HEA products exhibit better tensile properties than EBM-printed ones, due to their finer crystal grains and uniform composition without any intermetallic compound precipitates. The exceptional elongations with improved strength of printed AlCoCrFeNi and CoCrFeMnNi HEA products indicate a strength-ductility synergy, which is superior to those manufactured by conventional processes.

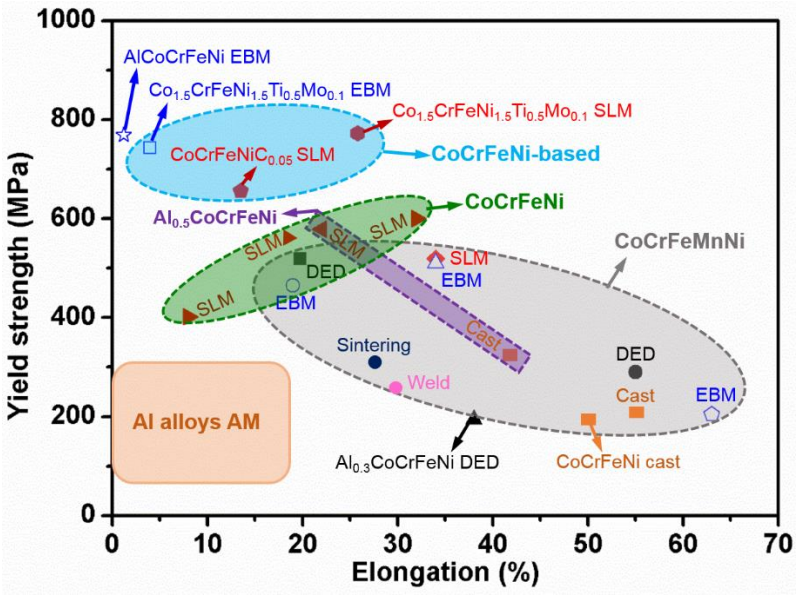

Figure 22. Summary of tensile yield strength versus elongation for 3D-printed HEA products.

Compared to the casting process, DED and PBF processes show a significant solute-trapping effect and minimize the element segregation due to their small melt pool sizes and rapid cooling rates, contributing to improved mechanical properties. The strengthening strategies of printed HEA products are attributed to grain boundary strengthening, precipitation hardening, solid solution strengthening and strain hardening. Zhou *et al.* illustrated that the yield strength of $Al_{0.5}$FeCoCrNi HEA products printed by SLM was 73.4 % higher than those fabricated by casting, due to the increase in grain boundaries hindering dislocation motion.[85] The yield strength is related to the grain size according to Hall-Petch equation: $\sigma_y = \sigma_0 + k/d^{1/2}$, where σ_y is the yield strength, σ_0 the friction stress in the absence of grain boundaries, k a constant and d the grain size.[235] Li *et al.* obtained a precipitated σ phase and nano-twins in SLM-printed CoCrFeMnNi HEA products that had never been observed in their casting or deformed counterparts, which contributed to their enhanced mechanical properties.[90] Zhu *et al.* postulated that the excellent elongation of this HEA was derived from the steady strain hardening capability at high stress levels, maintained by complicated dislocation configurations from the extensive interactions between the slip bands and grain structures.[92]

Table 8. Tensile and compressive properties of 3D-printed HEA products, compared with those manufactured by conventional processes. UTS, UCS, YS and EI represent ultimate tensile strength, ultimate compressive strength, yield strength and elongation, respectively.

HEA	Printing process	Tensile property			Compressive property			Ref.
		YS (MPa)	UTS (MPa)	EI (%)	YS (MPa)	UCS (MPa)	EI (%)	
CoCrFeMnNi	DED	518	660	19.8	-	-	-	[174]
		-	-	-	260	1400	52	[157]
		290	535	55	-	-	-	[173]
		346	566	27	-	-	-	[228]
		517	650	16	-	-	-	[175]
		424	651	48	-	-	-	[229]
CoCrFeMnNi	DED + Annealing	232	647	58	-	-	-	
$Al_{0.3}$CoCrFeNi	DED	194	-	38	194	1400	-	[171]
Al_xCoCrFeNi		-	-	-	200–1400	1400–2100	2.5–10	[153]
$Al_{0.3}$CoCrFeNi	DED + HIP	-	825	6	183	-	-	[230]
$Al_{0.6}$CoCrFeNi		400	952	1	-	1595	74	
$Al_{0.85}$CoCrFeNi		-	-	-	1300	-	3	
AlCoCrFeNi	DED + Aging	-	-	-	1070–1310	2600–3020	16.8–24.9	[151]
$Al_{0.5}$CoCrFeNi	SLM	579	721	22	-	-	-	[85]
AlCoCrFeNi		-	-	-	1342	1471	6.4	[196]
AlCoCrFeNi	SLM + Annealing	-	-	-	744–766	1292–1600	11–16	
AlCrCuFeNi	SLM	-	-	-	-	2053	6.8	[197]
CoCrFeNi		402–600	480–745	8–32	-	-	-	[187]
		572	691	17.9	-	-	-	[200]
CoCrFeMnNi		519	601	34	-	-	-	[90]
		510	609	34	-	-	-	[92]
		-	-	-	703.5–778.4	-	-	[194]
$CoCrFeNiC_{0.05}$		656	797	13.5	-	-	-	[93]
		638	795	13.5	-	-	-	[202]
$Co_{1.5}CrFeNi_{1.5}Ti_{0.5}Mo_{0.1}$		773	1178	25.8	-	-	-	[203]
$Ni_6Cr_4WFe_9Ti$		742	972	12.2	-	-	-	[205]
		630–710	920–983	8.6–12.9	-	-	-	[206]
AlCoCrFeNi	EBM	769	1074	1.2	944–1015	1447–1668	14.5–26	[81, 82]

CoCrFeMnNi		205	497	63	-	-	-	[75]
$Co_{1.5}CrFeNi_{1.5}Ti_{0.5}Mo_{0.1}$		743.4	932	4	-	-	-	[203]
CoCrFeNi	3D extrusion + Sintering	250–388	598–864	33.8–37.6	-	-	-	[217]
AlCoCrFeNi	Binder jetting + Annealing	-	-	-	1203–1461	1996–2272	31.5–32.3	[218]
	Cast	-	-	-	1308.3	1425	5.6	[81]
CoCrFeMnNi		205	493	55	-	-	-	[231]
CoCrFeNi		188	457	50	-	-	-	[187]
AlCrCuFeNi		-	-	-	-	1750	1.8	[232]
$Al_{0.5}CoCrFeNi$		334	709	43	-	-	-	[233]
CoCrFeMnNi	Weld	270	565	30	-	-	-	[234]
	Sintering	312	613	27	-	-	-	[88]
CoCrFeNi	Hot extrusion	359	713	56	-	-	-	[87]

Additionally, strain hardening leads to the asymmetry in the tensile and compressive properties of printed HEA products. Joseph *et al.* discovered a significant asymmetry in the strain hardening rates and ductility of DED-printed $Al_{0.3}$CoCrFeNi products (**Figure 23**).[171] It was confirmed that the HEAs developed Σ3 twins that could accommodate a large amount of strain along the <001> orientation when compressed at a critical strain level. The absence of twinning in tension indicated that the minimum stress was not enough for the initial twinning. The progressive formation of fine compression twinning increased the flow stress due to two factors. One was the grain size refinement resulting from the twins creating high angle boundaries within the parent grains and the other was the increase in the global dislocation density, which provided unique high strain hardening rates of the HEA products during compression. The <001> direction was oriented suitably for twinning in compression, but poorly oriented for twinning in tension. High and sustained work hardening rates were obtained for orientations promoting deformation twinning in compression rather than in tension. This asymmetry between tension and compression was the result of the strong texture in the HEA products combined with the activation of deformation twinning. Similar asymmetry phenomena could also be observed in the study of Kuwabara *et al.*[82]

The constituent elements, processing conditions and working temperature are important factors in determining the mechanical properties of 3D-printed HEA products. The incorporation of additional elements into existing HEAs may refine their microstructures and promote the formation of precipitates to achieve a strengthening effect. Zhou *et al*. proved that the addition of carbon led to the improved tensile strength of SLM-printed CoCrFeNi HEA products.[93] Wu *et al.* further explained that such a strengthening mechanism was a combination of dislocation networks strengthening and nano-sized carbides strengthening.[202] Luo *et al.* developed Co-free AlCrCuFeNi HEA products by SLM and investigated the anisotropy in their compressive properties.[197] The fracture strength and ductility of HEAs perpendicular to the build direction were higher than those aligned in parallel, which was

attributed to the anisotropy in crystal features. In the perpendicular direction, grains preferentially grown along the <100> orientation contributed to the superior ductility, and an abundant precipitation of Cu-rich nano-scale precipitates at the grain boundary resulted in an increase in fracture strength.

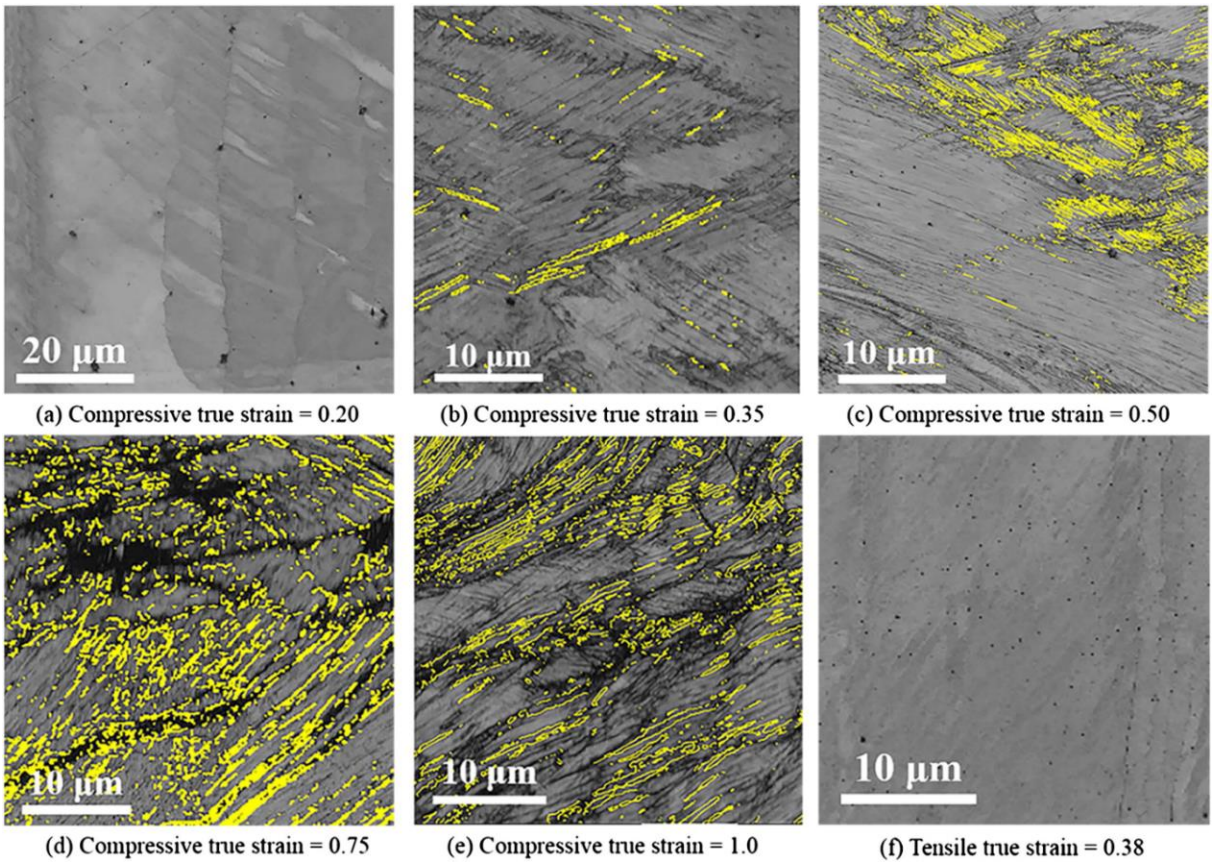

Figure 23. EBSD map of the DED-printed $Al_{0.3}CoCrFeNi$ HEA products deformed to various strain levels in compression and tension. Boundaries within 5° of the twin orientation have been highlighted in yellow.[171] Reproduced with permission.[171] Copyright 2017, Elsevier.

With regard to processing conditions, the optimization of energy density results in the increase in the relative densities, change of crystallographic directions, reduction of grain sizes and improvement on mechanical properties of printed HEA products.[80, 90, 92, 93, 173, 193, 197] Besides, heat treatment is often adopted to improve the mechanical properties of HEA products by removing various defects and releasing the residual stress existing in DED- and SLM-printed HEA products. Annealing is able to facilitate recrystallization and reduce residual stress effectively. In the study of Zhang *et al.*, the fracture strength and plastic strain

of SLM-printed AlCoCuFeNi HEA products were improved but their compressive yield strength showed a 47 % reduction after annealing.[196] A similar reduction in yield strength was also observed in annealed SLM-printed CoCrFeNi and DED-printed CoCrFeMnNi products.[187, 228] Heat treatment also brings about grain coarsening of the printed HEA products. The influences of grain coarsening and tensile residual stress relaxation on the tensile properties of the HEA products may offset against each other.

Hot isostatic pressing (HIP) improves the densification of HEAs and increases the coarsening of grains and precipitates. Joseph *et al.* found that HIP induced microstructural coarsening, facilitated chemical homogenization and resulted in improvements in certain mechanical properties of DED-printed $Al_{0.3}$CoCrFeNi HEA products.[230] The relative density of the printed products was 99.4%, and increased to 99.5% after HIP. HIP was found to possess a smaller number of large pores with size greater than 5 μm in the printed products, leading to a slight increase in density. However, other mechanical properties of $Al_{0.85}$CoCrFeNi HEA products were compromised due to the formation of an σ phase that induced brittle fractures under tension and compression and the coarsening of hard BCC precipitates at the grain boundaries. The coarse grain boundary particles that developed during HIP of the HEAs were responsible for their loss of ductility. Similarly, Li *et al.* obtained an 8 % improvement of tensile strength but a 49 % drop in the elongation of SLM-printed CoCrFeMnNi HEA products after HIP.[90]

The responses of 3D-printed HEA products to the heat treatments of both HIP and annealing are similar to those of conventionally manufactured products. For instance, the DED-printed AlCoCrFeNi HEA products after HIP exhibited the grain coarsening, chemical homogenization and relieving of residual stresses, similar to HIP-processed casted AlCoCrFeNi products.[236] Both HIP and annealing treatments led to the precipitation of σ phase in the printed HEA products, which was also reported for their treated casted counterparts.

Solution treatment is beneficial to the strength enhancement of printed HEA products. Fujieda *et al.* studied the effects of water quenching and air cooling on the mechanical properties of $Co_{1.5}CrFeNi_{1.5}Ti_{0.5}Mo_{0.1}$ products printed by SLM and EBM.[203] Both of them contributed to the improvement of the ultimate tensile strength of the products (**Figure 24**a). The difference in grain sizes could not completely explain the variation of yield strength since they were also affected by cooling conditions (Figure 24b). It was found that the yield strength increased proportionally with the square root of the product of radius and volume fraction of ordered (Ni, Ti)-rich precipitates (Figure 24c). Therefore, the yield strength of solution-treated printed HEA products strongly depends on the precipitation morphology of ordered particles that act as weak obstacles to dislocation motion.

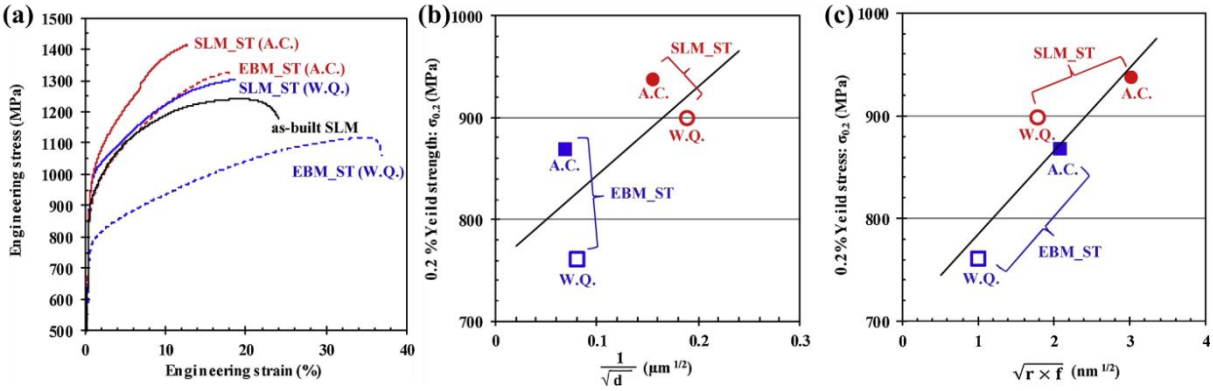

Figure 24. The comparison of mechanical properties of $Co_{1.5}CrFeNi_{1.5}Ti_{0.5}Mo_{0.1}$ HEA products printed by SLM and EBM with the solution treatments of both water quenching and air cooling: (a) tensile stress-strain curves, (b) relationship between yield strength and grain size (*d*: average grain diameter), and (c) dependence of size and volume fraction of ordered particles on yield strength (*f*: volume fraction of ordered particles, *r*: radius of ordered particles).[203] Reproduced with permission.[203] Copyright 2019, Elsevier.

Chew *et al.* evaluated the tensile properties of DED-printed CoCrFeMnNi HEA products at different temperatures of -130°C, 0 and 25 °C.[174] As the temperature decreased, the products exhibited simultaneous enhancements of yield strength, ultimate tensile strength and elongation (**Figure 25**a), steadier work hardening behaviors (Figure 25b), and an increase in dislocation densities indicated by the rising kernel average misorientation (Figure 25c). For the product which fractured at -130 °C, its value of kernel average misorientation reached as

high as 3°, indicating significant dislocation trapping. The blue and red lines in Figure 25d represent the high angle grain boundaries and deformation twins respectively. The formation of deformation twins in the HEA products at -130 °C contributed to the steady strain hardening behavior that enhanced their elongation. Similar improvements on the properties of the same printed HEA products were obtained by Xiang *et al.*, showing a 39 %, 64 % and 73 % increase in their yield strength, ultimate tensile strength and ductility, respectively, as the temperature decreased from 293 K to 77 K.[173] The interaction mechanism of dislocation and deformation-induced twinning that contributed to continuous accumulation of dislocations ensured high work hardening rates and good tensile properties for HEAs under cryogenic conditions.[237]

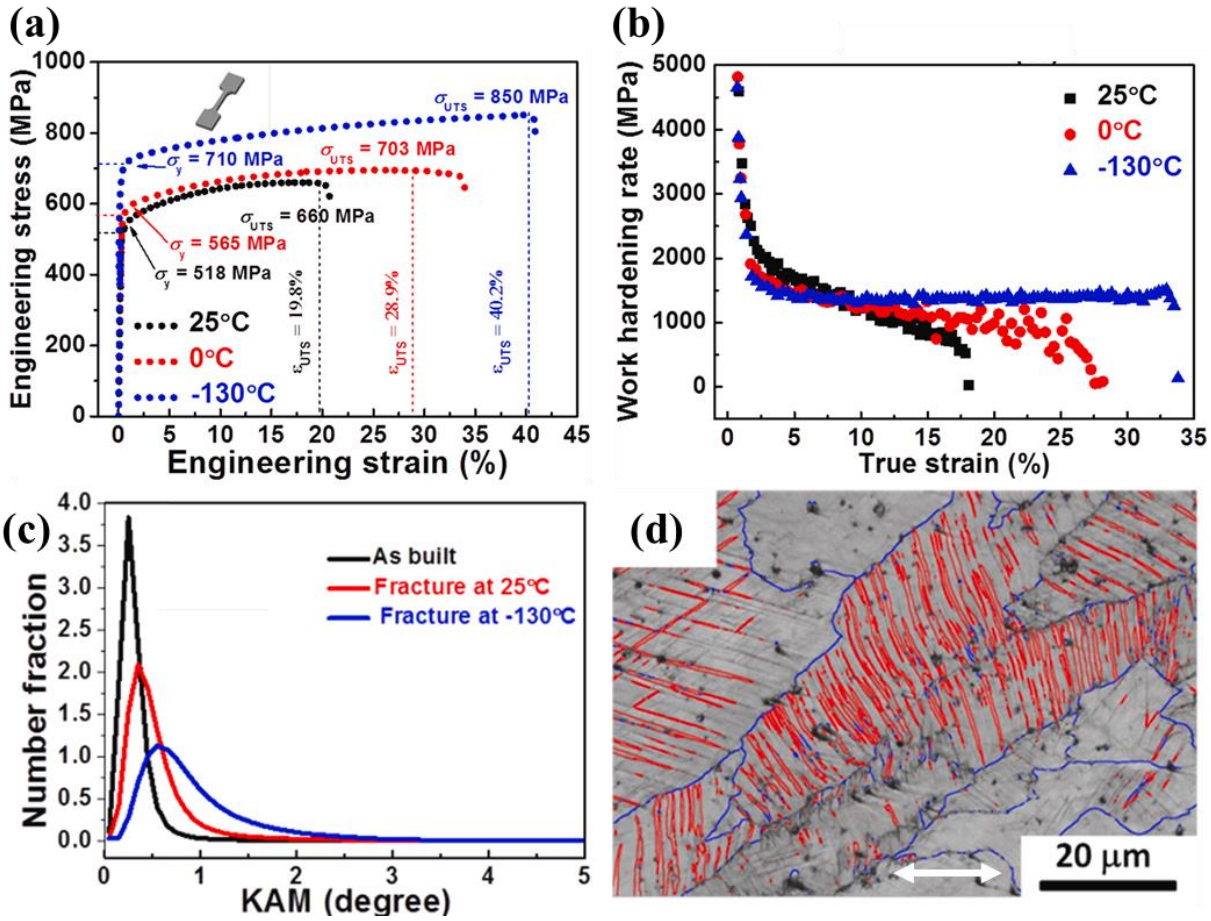

Figure 25. (a) Tensile stress-strain curves of DED-printed CoCrFeMnNi HEA products at 25, 0, and -130 °C, respectively; (b) strain hardening curves deformed at 25, 0, and -130 °C, respectively, (c) kernel average misorientation distributions, and (d) grain boundary map showing the deformation twins at -130 °C. The blue and red lines represented the high angle

grain boundaries and deformation twins, respectively. The white arrow indicated the tensile axis.[174] Reproduced with permission.[174] Copyright 2019, Elsevier.

4.2. Functional properties

There is increasing interest regarding the functional properties of 3D-printed HEA products, including their corrosion properties, magnetic properties and hydrogen storage properties. Promising properties and interesting phenomena pertaining to printed HEA products present attractive research directions to be explored and developed from both theoretical and application-oriented perspectives.

HEAs have been reported to exhibit better corrosion resistance than conventional alloys.[238-240] The concentration and distribution of corrosion-resistant elements, phase transformation, and element segregation determine the corrosion properties of printed HEA products. Fujieda *et al.* investigated the effect of solution treatment on the corrosion properties of $Co_{1.5}CrFeNi_{1.5}Ti_{0.5}Mo_{0.1}$ products printed by EBM and SLM.[203, 213] **Figure 26**a shows the potentiodynamic polarization curves of treated and untreated EBM-printed products, which indicated the passivation state ended at the pitting potential when a sharp increase occurred in the corrosion current. The pitting potentials of the products improved greatly after the solution treatment. The treated HEA products possessed both high strength and high pitting potentials, superior to those of the conventional alloys used in severely corrosive environments (Figure 26b). Incidentally, the pitting potentials of SLM-printed HEA products increased after water quenching (Figure 26c), resulting from the elimination of intermetallic compounds. However, air cooling decreased the pitting potentials, which was ascribed to the larger sizes of ordered particles that formed the Cr-depleted regions.

Figure 26d depicts the dependence of the size and volume ratios of ordered particles on the pitting potentials of treated HEAs. The pitting potentials were inversely proportional to the product of the radii and volume fractions of the ordered particles, indicating that the pitting-corrosion resistance would decrease as the number of ordered particles increases. The

effectiveness of solution treatments on the EBM-printed HEA products was more prominent than the SLM-printed counterparts.

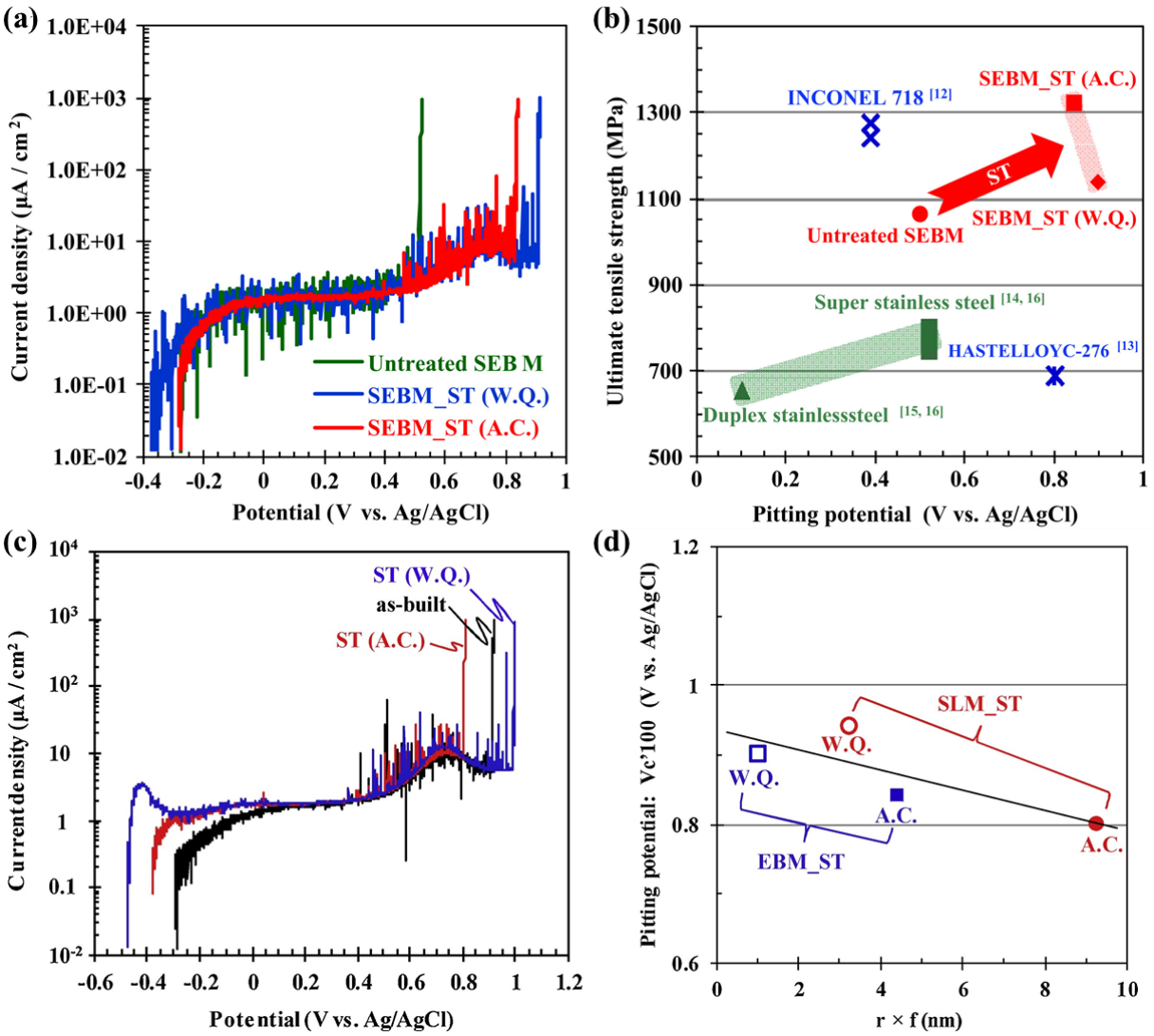

Figure 26. Corrosion properties of $Co_{1.5}CrFeNi_{1.5}Ti_{0.5}Mo_{0.1}$ HEA products printed by EBM and SLM with solution treatments: (a) potentiodynamic polarization curves of EBM-printed HEA products before and after the treatments, (b) comparison of tensile strength and pitting potential between the HEAs and conventional alloys,[213] (c) potentiodynamic polarization curves of SLM-printed HEA products, and (d) dependence of size and volume ratio of ordered particles on pitting potential of solution-treated HEA products (*f*: volume fraction of ordered particles, *r*: radius of ordered particles).[203] Reproduced with permission.[213] Copyright 2017, Elsevier. Reproduced with permission.[203] Copyright 2019, Elsevier.

Sarswat *et al.* conducted a comparative study on the corrosion resistance of AlCoFeNiTiVZr, $AlCoFeNiSm_{0.05}TiV_{0.95}Zr$, $AlCoFeNiV_{0.9}Sm_{0.1}$ and $AlCoFeNiSm_{0.1}TiV_{0.9}$ HEA products printed by SLM.[199] The Zr-based HEA products exhibited better corrosion

resistance than Zr-free products due to their higher corrosion potentials and lower corrosion current densities. Besides, the elevated temperature corrosion behavior of the printed $AlCoFeNiTiSm_{0.1}V_{0.9}$ and $AlCoFeNiSm_{0.1}V_{0.9}$ products were also reported.[241] These products were tested in corrosive syngas atmosphere at elevated temperatures and showed excellent corrosion resistance, indicating their potential applicability in harsh environments. Wang *et al.* evaluated the corrosion properties of DED-printed AlCoCrFeNi HEA products aged at different temperatures.[150] The products aged at 1200 °C showed a better corrosion resistance than those aged at 800 and 1000 °C, which was a consequence of the size differences of the FCC precipitates. Typical electrochemical parameters of 3D-printed HEA products are concluded in **Table 9**.

Table 9. Electrochemical parameters of 3D-printed HEA products.

HEA	**Process**	**Solution**	**Corrosion potential (mV)**	**Pitting potential (mV)**	**Corrosion current density ($\mu A/cm^2$)**	**Ref.**
AlCoCrFeNi	EBM	Artificial seawater	-355	112	1.45	[82]
	DED + Aging (800℃)	0.6 M NaCl	-264.1	5.1	0.117	[150]
	DED + Aging (1000℃)		-259.6	-7.2	0.129	
	DED + Aging (1200℃)		-240.9	35.5	0.089	
CoCrFeMnNi	DED		-250	400	-	[229]
	SLM	3.5 wt% NaCl	-189	197	0.09	[242]
$Co_{1.5}CrFeNi_{1.5}Ti_{0.5}Mo_{0.1}$	EBM		-	500	-	[213]
	EBM + Water quenching		-	900	-	
	EBM + Air cooling		-	840	-	
	SLM		-	880	-	[203]
	SLM + Water quenching		-	1000	-	
	SLM + air cooling		-	800	-	
AlCoFeNiTiVZr	SLM		-755	10	36.31	[199]
$AlCoFeNiSm_{0.05}TiV_{0.95}Zr$			-665.9	10	10.96	
$AlCoFeNiSm_{0.1}V_{0.9}$			-655	-	8.32	
$AlCoFeNiSm_{0.1}TiV_{0.9}$			-628.3	-	6.75	
MoNbTaW			-91.57	-	0.00024	[204]

Kuwubawa *et al.* discovered that the corrosion resistance of EBM-printed AlCoCrFeNi HEA products were inferior to that of their casted counterparts which was illustrated by their different corrosion morphologies.[82] The casted AlCoCrFeNi products showed polygonal shaped stripes that reflected the orientation of the grains (**Figure 27**a), and small pits were found around the grain boundaries with residual island-like regions (Figure 27b). On the contrary, pits on the EBM-printed AlCoCrFeNi products presented mesh-like holes (Figure 27c) that were distributed at the interfaces between BCC and B2 phases (Figure 27d).

The pitting initiation and dissolution were observed to preferentially exist in Cr-deficient regions that offered sites for local pitting. The Cr-depleted regions formed around the grain boundaries of the casted AlCoCrFeNi, while appearing along the edges of the dark regions in the EBM-printed products. The Cl ion in the electrolyte solution severely attacked the (Al, Ni)-rich B2 phase, while the (Fe, Cr)-rich FCC phase remained unattacked. The corrosion preference of the B2 phase could be primarily attributed to galvanic coupling of the FCC precipitate and the B2 matrix. This potential difference provided a strong driving force for the dissolution of the less noble Cr-depleted B2 matrix.

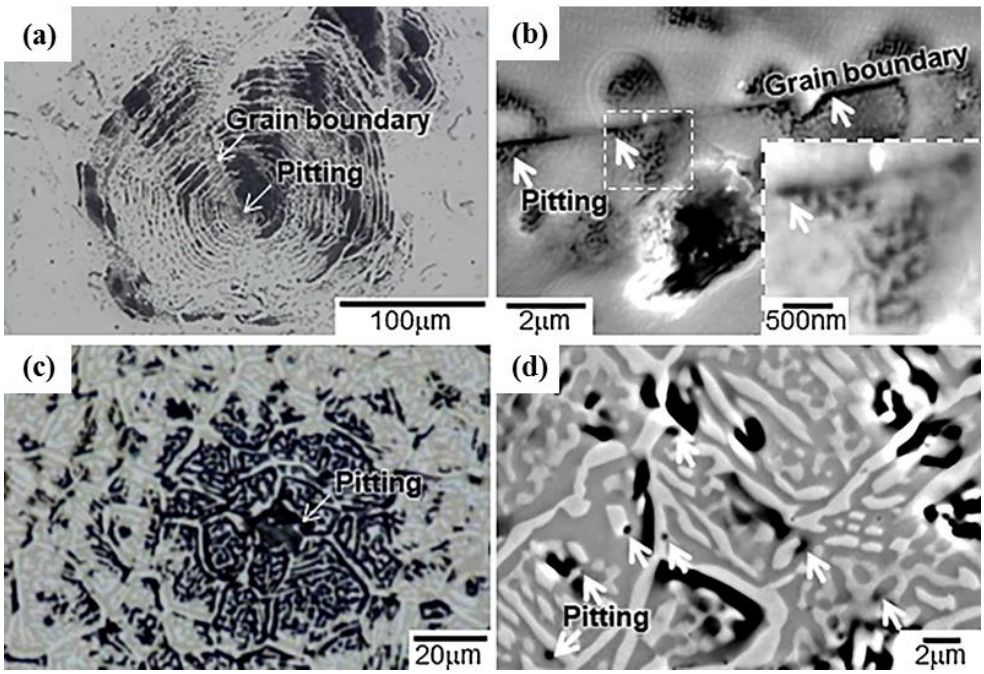

Figure 27. Corrosion morphologies of AlCoCrFeNi HEA products printed by EBM and casting: (a) and (b) casted product, (c) and (d) EBM-printed product.[82] Reproduced with permission.[82] Copyright 2018, Elsevier.

HEAs containing Co, Fe and Ni elements usually possess electromagnetic wave absorbing and magnetic properties.[243-246] The composition coupled with the microstructures of the 3D-printed HEA products can substantially influence their magnetization behaviors and magnetic properties. Borkar *et al.* evaluated the magnetic properties of DED-printed $AlCo_xCr_{1-x}FeNi$ HEA products with varying Co content (**Figure 28)**.[152] The saturation magnetization of the HEA was strongly dependent on its composition in contrast to its microstructure. It decreased from 117.8 emu/g to 18.48 emu/g with decreasing Co content, due to the ferromagnetic nature of Co and the antiferromagnetic nature of Cr. Increasing the Cr content of the products reduced ferromagnetic interactions between Fe, Ni and Co, and resulted in a lower temperature for ferromagnetic to paramagnetic transition (Figure 28a). In contrast, the coercive force of the products appeared to be strongly dominated by its microstructure (Figure 28b). The severe spinodal decomposition in the BCC matrix affected the pinning of magnetic domains and the coercive force. The well-developed spinodally decomposed B2 + BCC phases exhibited a high coercive force because its phase boundaries acted as pinning sites for the domains. Besides, the difference in lattice diameter between the B2 and BCC phases was accommodated by coherency stresses that could counteract against the orientation of elementary magnetic domains imposed by an external magnetic field.

Figure 28c shows the temperature dependence of magnetization within an applied field of 1000 Oe, while Figure 28d reveals the change in Curie temperature T_c with respect to the Co content. The reduction of T_c was consistent with the mean-field model $T_c = J_{eff}(r) Z_T S(S+1)/3k_B$, where $J_{eff}(r)$ is the effective exchange interaction, Z_T the coordination number, S the atomic spin quantum number, and k_B the Boltzmann constant. Due to the

antiferromagnetic ordering of Cr, the effective exchange interaction of the HEA decreased with the increase in its Cr content.

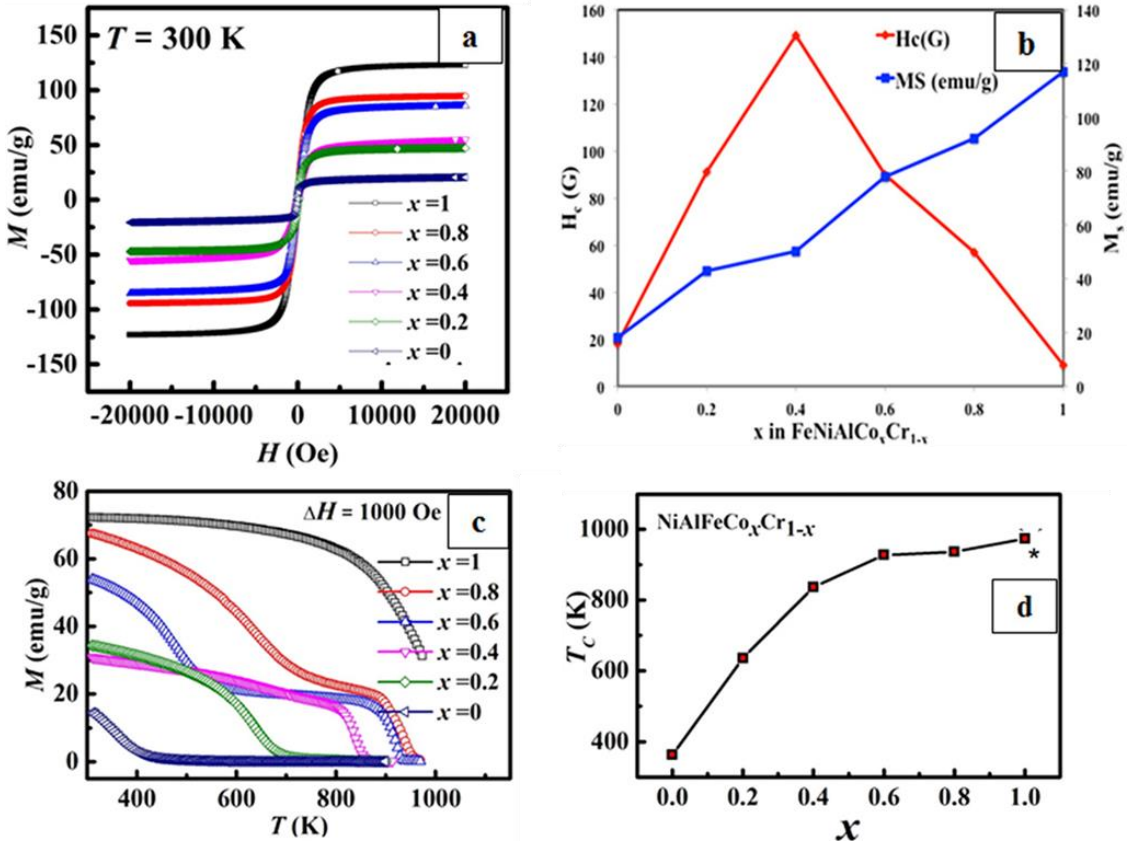

Figure 28. Magnetic properties of DED-printed $AlCo_xCr_{1-x}FeNi$ HEA products: (a) magnetizations M as a function of applied magnetic field H at 300 K, (b) saturation magnetization M_s and coercive force H_c as a function of Co concentration, (c) saturation magnetization as a function of temperature at a magnetic field of 0.1 T at temperatures ranging from room temperature to 973 K, and (d) variation of T_c with the Co concentration.[152] Reproduced with permission.[152] Copyright 2017, Wiley-VCH.

HEAs have been used as hydrogen storage materials due to their high storage capacity per volume, high absorption/desorption reversibility and low cost benefit.[247-249]. Kunce *et al.* conducted a series of research work on DED-printed HEA products for hydrogen storage.[159-161]. The hydrogen storage curves and hydrogen absorption/desorption isotherms of printed HEA products, including LaNiFeVMn, TiZrNbMoV and ZrTiVCrFeNi, are displayed in **Figure 29**. The activated HEAs absorbed more hydrogen and exhibited shorter incubation periods before hydrogen absorption. As shown in Figure 29a, the maximum hydrogen storage capacity of LaNiFeVMn HEA products was proportional to the atomic content of La.

Particularly, the hydrogen dissolved in σ-type phase matrices with lower La contents acted as hydrogen traps and thus decreased the effective hydrogen diffusion coefficient of the HEAs. In addition, the HEA products exhibited different hydrogen absorption/desorption equilibrium pressures (Figure 29b). The element segregation strongly influenced the equilibrium pressure due to different lattice expansions, but further investigations are still required for the underlying mechanisms.

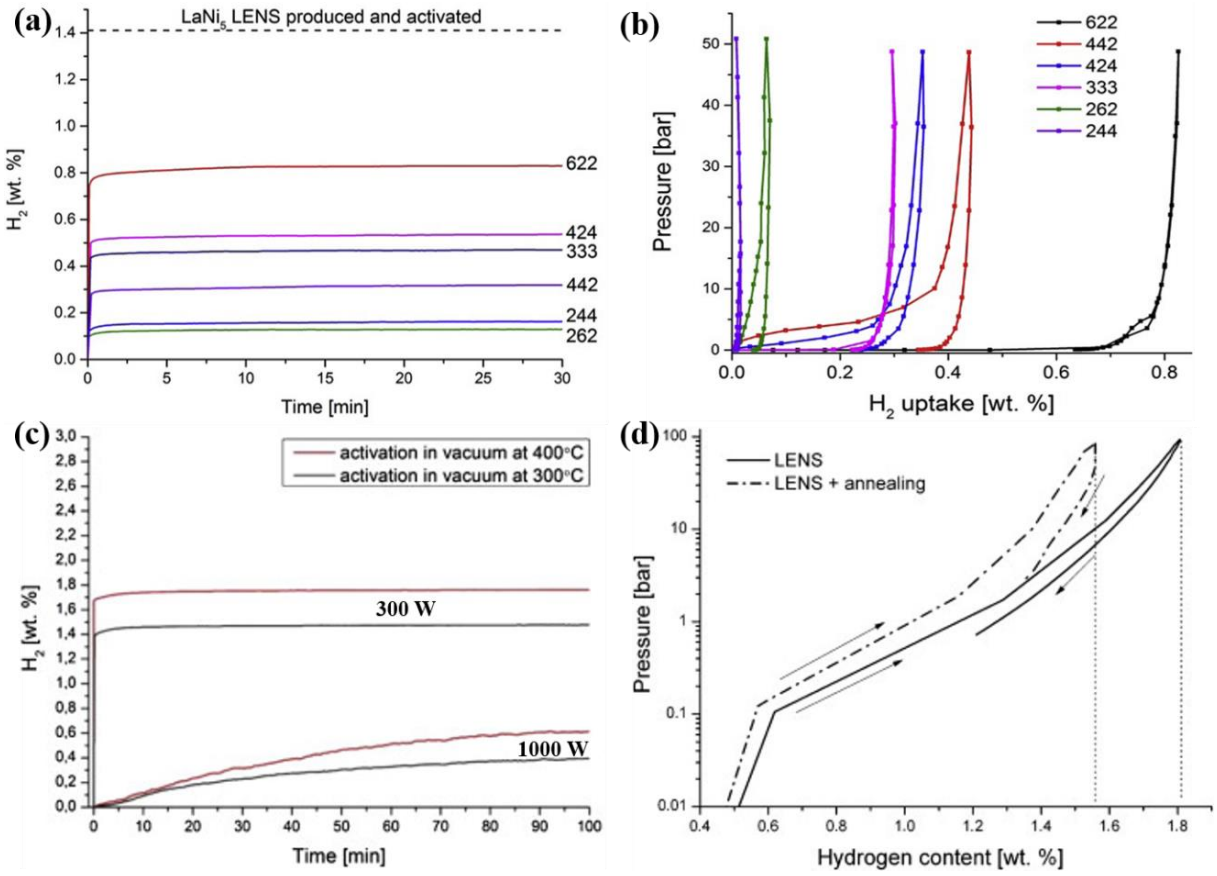

Figure 29. Hydrogen storage properties of DED-printed HEA products: (a) hydrogen absorption kinetics curves of LaNiFeVMn products taken at 35 ℃ after activation, (b) hydrogen absorption and desorption isotherms for the products. Code 622, 442, 424, 333, 262 and 244 represent for $La_{0.1}Ni_{0.5}Fe_{0.1}V_{0.1}Mn_{0.2}$, $La_{0.07}Ni_{0.33}Fe_{0.2}V_{0.2}Mn_{0.2}$, $La_{0.07}Ni_{0.33}Fe_{0.1}V_{0.1}Mn_{0.4}$, $La_{0.06}Ni_{0.28}Fe_{0.16}V_{0.16}Mn_{0.33}$, $La_{0.03}Ni_{0.17}Fe_{0.3}V_{0.3}Mn_{0.2}$ and $La_{0.03}Ni_{0.17}Fe_{0.2}V_{0.2}Mn_{0.4}$, respectively,[161] (c) hydrogen absorption curves of TiZrNbMoV HEA products produced using the laser power of 300 and 1000 W after activation at 300 and 400 °C,[159] and (d) hydrogen absorption and desorption isotherms for ZrTiVCrFeNi HEA products before and after annealing at 1000 °C for 24 h.[160] Reproduced with permission.[161] Copyright 2017, Elsevier. Reproduced with permission.[159] Copyright 2014, Elsevier. Reproduced with permission.[160] Copyright 2013, Elsevier.

A low laser power substantially improved the hydrogen absorption properties of TiZrNbMoV HEA products (Figure 29c), which was determined by their phases and structural stability. FCC + BCC + $NbTi_4$-type phases were obtained using a low power laser at a maximum hydrogen capacity of 2.3 wt%. In addition to the hydrogen absorption of Ti and Nb, BCC structures are particularly advantageous for hydrogen storage.[250, 251] However, the hydrogen absorption of HEA products was small (0.59 wt%) even when they exhibited a stable BCC phase and no element segregations at the dendrites. The severe lattice distortion effect in HEAs reduced the number of interstices available for hydrogen atoms, which was proved by the evaluation of ZrTiVCrFeNi HEA products that underwent heat treatment (Figure 29d). The variation in the hydrogen storage properties of the products with and without annealing at 1000 °C is reflected by the difference in the volumetric lattice expansion of C14 phase. The annealing process improved the compositional homogeneity of the products and resulted in a relaxed crystal lattice, which reduced the deformation of interstitial holes for the storage of hydrogen atoms and thus lowering their hydrogen capacity.[252]

Hydrogen is detrimental to metals due to hydrogen-induced embrittlement. FCC HEAs were reported to be hydrogen tolerant materials.[253, 254] Particularly, CoCrFeMnNi HEAs were demonstrated to enhance their hydrogen embrittlement resistance through the nano-twin gradients by a self-accommodation mechanism.[255] The high local hydrogen content resulted in a high twin formation rate as hydrogen reduced the stacking fault energies in the HEAs. Dislocations accumulated along the twin boundaries promoted a more uniform plastic deformation, enhancing ductility. The high density of partial dislocations and their interactions, together with the small average twin spacing both enabled strain hardening. This hydrogen resistant property of CoCrFeMnNi HEAs opens a pathway to develop 3D-printed HEA products that withstand heavy mechanical loading under hydrogen-rich conditions.

4.3. Potential applications of printed HEAs

The novel properties of HEAs, such as superb specific strength, excellent mechanical performance at high temperature, exceptional ductility and fracture toughness at cryogenic temperatures, superparamagnetism and superconductivity, pave the way to various applications in aerospace, transportation, energy, electronics, biomedical, molds and tools sectors. HEAs can be used as hydrogen storage materials, radiation resistant materials, diffusion barriers for electronics, precision resistors, electromagnetic shielding materials, thermal-sprayed, hard, low-friction and biomedical coatings, binders, and soft magnetic and thermoelectric materials.[45, 246, 248, 256-259]

The recent advancements in powder development, printing processes and printed product performances as discussed in the previous sections, establishing 3D printing as a valuable technology for manufacturing HEA products. Compared to conventional manufacturing processes, the rapid solidification in DED and PBF results in outstanding properties of printed HEA products due to their refined microstructures. 3D printing of HEAs allows for a combination of material selection, design and manufacturing freedoms for lightweight, customizable and non-assembly required products. New advances in material development and structural optimization enable the printing of HEA products with complex geometries for applications in the aerospace, energy, molding, tooling, and other industries.

3D-printed HEA products show great potential in the aerospace industry due to the increasing requirements and demand for lightweight materials. There are ongoing efforts on the development of lightweight HEAs based on elements with lower densities such as Al, Mg, Be and Ti.[59, 151, 260] However, lightweight HEAs with single solid solution phases are difficult to synthesize as most of the lightweight elements are immiscible with other transition metals like Cr, Fe, Cu, which tend to form intermetallic compounds among themselves. In addition to element selection, lightweight designs can be achieved through the structural optimization of printed HEA products.

To validate the practical usage of the $Al_{0.5}$CoCrFeNi HEA powder, a small turbine blade with complex geometries was printed by SLM without any macroscopic defects (**Figure 30**a). Moreover, a refractory WNbTaMo blade was produced without warping or cracking deformations by optimizing the printing parameters of SLM (Figure 30b), which was achieved through an interpretation of thermal and mechanical models of the system, coupled with the finite difference-finite element approach. DED was also successfully employed in printing a vane prototype using CoCrFeMnNi HEA powder (Figure 30c). Other applications in the aerospace industry can be valve trains, compressor blades, combustion chambers, exhaust nozzle and gas turbine of aero-engine, where printed HEA products are able to combine their advantages of high strength-to-weight ratio, good oxidation resistance, fatigue resistance, hot consumption opposition, elevated temperature strength, lightweight, wear and creep resistance.

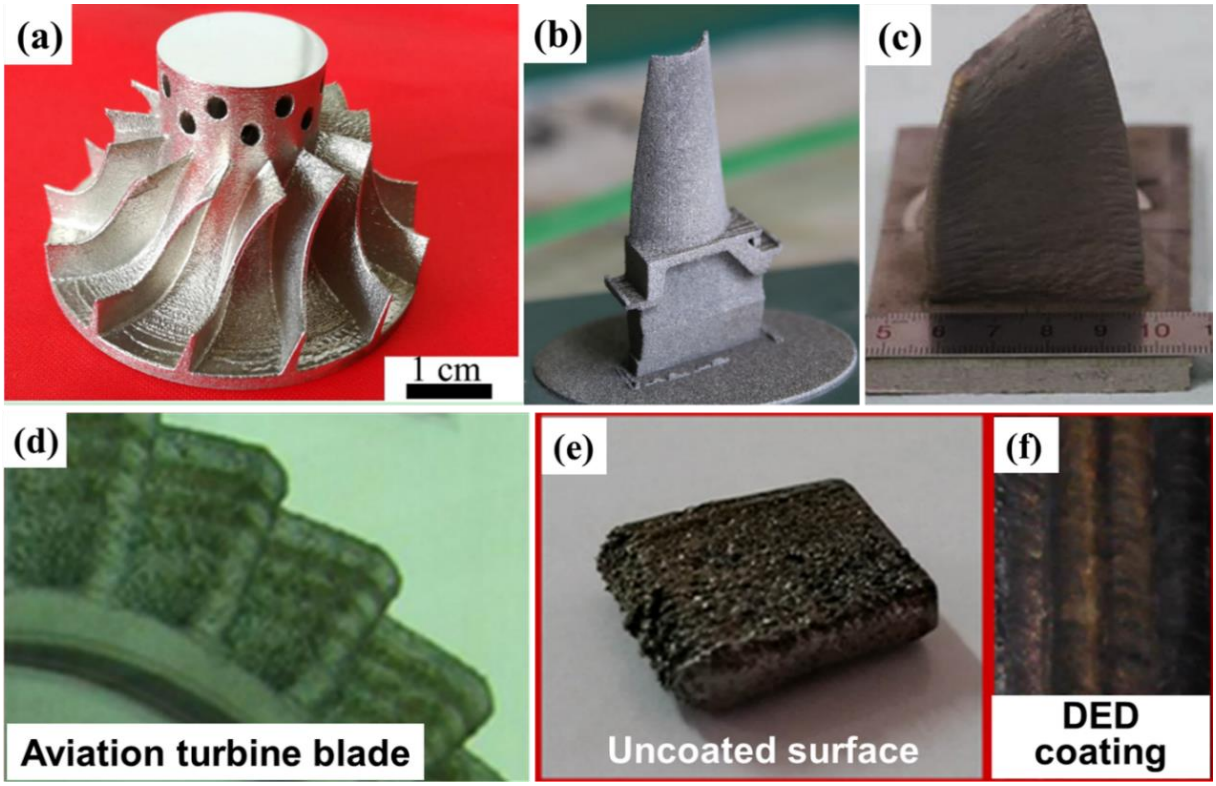

Figure 30. Validation of HEA products by DED and PBF printing processes in the aerospace industry: (a) a SLM-printed $Al_{0.5}$CoCrFeNi turbine blade,[85] (b) a SLM-printed WNbTaMo blade,[208] (c) a DED-printed CoCrFeMnNi vane prototype,[173] (d) a DED-printed titanium aviation turbine blade, (e) uncoated surface of the blade, and (f) modified surface with HEA coating by DED.[155] Reproduced with permission.[85] Copyright 2019, Elsevier. Reproduced

with permission.[208] Copyright 2018, Springer. Reproduced with permission.[173] Copyright 2019, Elsevier. Reproduced with permission.[155] Copyright 2017, Elsevier.

HEAs have been used as heat- and wear-resistant coatings to improve the surface properties of printed products against tough environmental conditions, especially in the aerospace industry.[261] In particular, DED can prepare uniform, functional, highly cohesive coatings on the printed products. Li *et al.* developed an integrated method to prepare an ultrafine nanocrystal modified HEA coating for a titanium aviation turbine blade using DED (Figure 30e and f), which improves the wear resistance of the blade.[155]

HEAs are employed as irradiation-resistant materials for nuclear energy industries.[262-264] A potential application of 3D-printed HEA products is the in-vessel components of international thermo-nuclear experimental reactors, which consist of different sub-components. These reactors present an opportunity to develop high-pressure vessel HEA products with improved irradiation and corrosion resistance,[265] as the first wall panels of one of the reactors were printed using SLM and EBM of the stainless steel powder.[266] Refractory HEAs that offer a low thermal neutron absorption, i.e. TiVCrNbMo,[267] TiVZrTa and TiVCrTa,[268] can be proposed for these components.

On another note, thermoelectric HEAs, such as $Al_xCoCrFeNi$,[269] $BiSbTe_{1.5}Se_{1.5}$ [270] and PbSnTeSe,[271] were proved to be effective in converting waste heat into electricity. Printed HEA products can be extended to components within high-temperature thermoelectric generators that recycle a large portion of waste heat efficiently.

By incorporating multiple elements at either the powder development or processing stage, 3D printing offers an effective strategy to engineer porous HEA architecture used for heat transfer in the heat exchangers from the macro- to micro-scale. Besides, the CoCrFeNi HEA micro-lattices printed by 3D ink-extrusion can be applied at cryogenic temperatures, within components that require high ductility and fracture toughness (**Figure 31**). Combined with the geometrical freedom of extrusion printing to create micro-lattices at low cost, this material-

process combination could be scaled up for the mass production of lightweight, high ductile, impact-absorbing HEA products that can operate reliably at temperatures ranging from -210 °C to 1000 °C.[217]

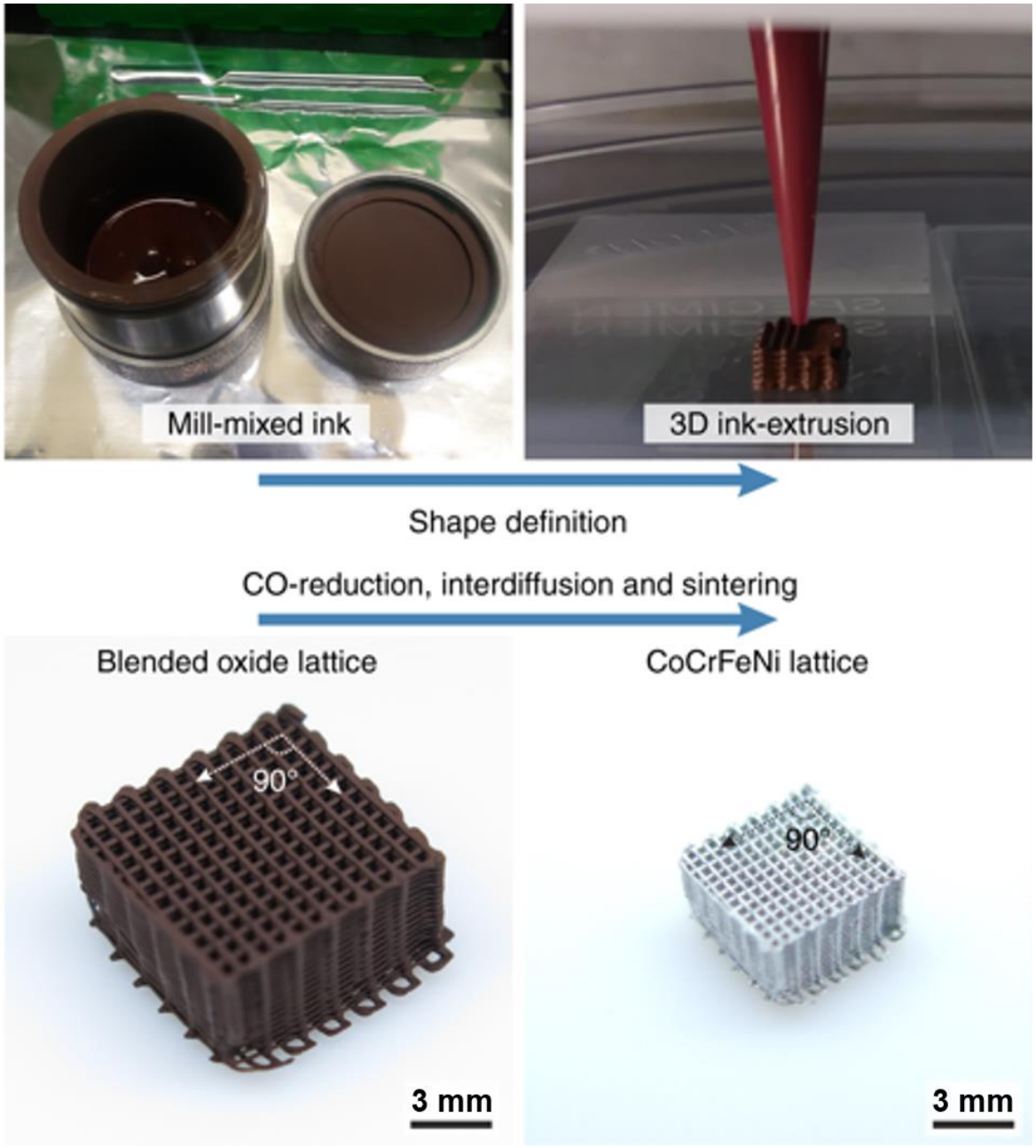

Figure 31. A CoCrFeNi HEA micro-lattice printed using 3D ink-extrusion from mill-mixed ink. The ink for ink-extrusion was mill-mixed and thickened for the shape-defining first step, which defined the architecture. The blended oxide lattice were co-reduced, inter-diffused and sintered to yield a CoCrFeNi HEA lattice with much smaller overall dimensions and strut diameter, without warping or cracking.[217] Reproduced with permission.[217] Copyright 2019, Nature Research.

3D-printed HEA products can be utilized in tooling and molding industries, such as manufacturing tools and injection molding, due to their high hardness, wear resistance, high-temperature softening resistance and anticorrosion. The HEA products of tools and their inserts can be printed from pre-designed models. Besides, HEA hard coatings can be developed to improve the performance and durability of the cutting tools.[272] To maximize their strength and minimize their weight, cellular lattices that lower both the material and manufacturing cost can be designed.[273] Furthermore, 3D-printed HEA products can be applied as hot working molds able to withstand at a temperature of 1200 °C.[58] In particular, 3D printing enables the fabrication of free-form cooling channels in HEA molds or inserts within prefabricated mold blocks, which align along the mold cavity surface and provide a homogeneous heat transfer and adaptive cooling. It provides better quality injected parts than the straight cooling channels obtained by conventional drilling in mold fabrication.

3D printing of HEAs can also have potential biomedical, automotive and catalyst applications. HEAs with negligible cytotoxicity, excellent biocompatibility, mechanical, electrochemical and anticorrosion properties, such as TiNbTaZrMo, TiZrHfCrMo, and TiNbTaZrHf, were reported for potential use as orthopedic implants.[274-276] Compared to conventional manufacturing processes such as casting and powder metallurgy, 3D printing is outstanding in manufacturing a gradient, functional and controlled architecture with both micro- and macro-porosity, which can provide 3D supports with pores to attach, grow and differentiate into functional tissues or organs. Therefore, 3D printing of biocompatible HEA implants with porosity gradients can be envisioned to promote osseointegration, reduce stress shielding and extend service life.

HEAs with a combination of high strength, good heat transfer properties and low density can be used to reduce the overall weight of engines in the automotive sector.[277] Especially for electric vehicles, their cruising range can be extended through the lightweight design of both materials and structures for 3D-printed HEA products. Besides, HEAs with a shape

memory effect, such as TiZrHfNiCoCu,[278] can be explored for 3D printing, providing the feasibility designs and accelerating the development of prototypes for automotive actuators.

The thermodynamically metastable state of HEAs have been suggested as potential catalysts owing to their significant stability in corrosive media as well as their highly catalytic activity.[279] The AlCoCrTiZn, AlCoCrFeNi and CoCrFeMnNi HEAs exhibited a prominent efficiency in degradation of the azo dye, which is attributed to the unique atomic structure with severe lattice distortion, chemical composition effect, residual stresses and high specific surface areas.[280] Porous structures manufactured by 3D printing have been demonstrated to improve the catalytic activity better than conventional 2D ribbons or powders.[281] Large specific surface areas in the porous structures are promising for achieving high effective 3D HEA catalysts with extraordinary catalytic activities.

Not limited to the exemplified applications, 3D printing of HEAs is expected to be able to overcome bottlenecks encountered by conventional manufacturing processes, thus leading to possible breakthroughs in other sectors.

5. Conclusion and perspectives

Inspired by the exciting prospects of HEAs and the unique advantages of 3D printing processes, explosive growth has been achieved in 3D printing of HEAs. This article has provided a review of the recent achievements of 3D printing of HEAs, in the aspects of their powder development, printing processes, phases, crystal features, mechanical properties, functionalities and potential applications. Atomization and mechanical alloying are popular choices in the development of HEA powders for 3D printing. The morphologies, particle size distributions and element distributions of the developed powders critically determine their printability. DED and PBF (SLM and EBM) are mainly used for printing HEA products from pre-developed powders due to their rapid solidification and the capability of producing complex geometries. Compared to PBF, DED can additionally utilize pristine elemental

powders from the multiple powder-feeding channels to print HEA products through *in situ* alloying, which circumvents the lengthy process of developing HEA powders.

A comparative summary of DED, SLM and EBM processes for printing HEA products is presented in **Table 10**. DED is the most popular process to print HEA products using HEA powders or pristine elemental powders. The lower scanning speed in DED results in a lower cooling rate, which leads to larger grain sizes in the printed products. Therefore, HEA products printed by DED exhibit lower strength than those printed by SLM and EBM. On a different note, large temperature gradients exist in the printing processes due to highly localized heat inputs and short interaction times. The rapid heating and cooling rates cause high residual stresses in DED- and SLM-printed products. These affect the microstructure, which govern the macroscopic performances of the products. Comparatively, residual stresses are negligible in EBM products due to the unique preheating process for the powder layers, which is beneficial in reducing cracks. The wide ranges of strength and elongation of the products are more dependent on the compositions of HEAs than the process parameters for these printing processes.

The microstructure of 3D-printed HEA products strongly depends on their compositions and process parameters. Despite the ultrafast cooling rate, undesirable intermetallic compound precipitates can still be observed in the solid solution matrix. Therefore, heat treatments such as annealing, solution treatments and hot isotropic pressing, are often carried out to avoid the formation of these adverse precipitates. Compared to conventional manufacturing processes, 3D-printed HEA products exhibit finer grains and simpler phases, resulting in superior mechanical properties and functionalities. Different printing processes induce substantial differences in both the strength and plasticity of their products, and subsequently, proper heat treatments are beneficial for enhancing the properties of HEA products by reducing various defects and releasing their internal residual stresses. 3D printing of HEAs allows for a combination of material selection, design and manufacturing freedoms for lightweight,

customizable and non-assembly required products. New advances in material development and structural optimization enable the printing of HEA products with complex geometries for applications in the aerospace, energy, molding and tooling industries.

Table 10. A comparative summary of DED, SLM and EBM processes for printing HEA products.

	DED	**SLM**	**EBM**
Number of HEA types	17	15	4
Environment	Argon	Argon	Vacuum
Feedstock	Pre-alloyed powder, elemental powder	Pre-alloyed powder	Pre-alloyed powder
Powder feed	Brown powder	Powder bed	Powder bed
Energy source	Laser	Laser	Electron beam
Scanning speed (mm/s)	1–20	10–2000	215–3446
Preheating (°C)	-	-	900–1253
Residual stress	High	High	Very low
Tensile yield strength (MPa)	194–518	402–773	205–769
Ultimate tensile strength (MPa)	535–660	480–1178	497–1074
Elongation (%)	19.8–55	8–34	1.2–63
Microhardness (HV)	195–860	212–829	157–500

The perspectives regarding the future of 3D printing of HEAs are outlined as follows.

Novel HEA powders for 3D printing can be developed through the optimization of powder production processes. In addition to the commonly used elements mentioned in Section 1, precious metal elements (Ag, Au, Pd, Pt, Rh, Ru, etc.), low-density metal elements (Be, Li, Mg, Sc, Si, Sn, Zn, etc.) and lanthanide elements (Dy, Gd, Lu, Tb, Tm, etc.) can be considered for the composition design of novel HEA powders. In particular, the constituent elements should have sufficient strength to resist residual stresses and be resistant to cracks caused by the rapid solidification of the printing processes. Optimization of powder production processes can be performed to develop novel HEA powders with high purity, high

degrees of sphericity, low oxygen contents and homogeneous elemental distributions for printing purposes. The printing performances of the developed HEA powders can then be evaluated.

Development and optimization of printing processes can be initiated to improve the quality of printed HEA products. Printing processes such as binder jetting and material extrusion can be employed to avoid thermal stresses existing in DED- and SLM-printed HEA products, thus contributing to the reduction in cracks and deformation. Properties of the printed products, such as fracture toughness, fatigue properties, creep properties, oxidation resistance and irradiation resistance, can be exploited for different purposes. The correlations between material-processing and the product properties need to be established, and the underlying mechanisms can be explored. For DED and PBF printing processes using pre-developed HEA powders, *in situ* monitoring for geometrical signatures of melt pools can be used to inspect the quality of each printed layer, which provides guidance to the optimization of printing processes. The 3D surface topography and contour data of HEA melt pools can be monitored using vision sensing methods to assess the surface quality and improve it through optimizing the printing parameters. The powder-spreading process in PBF can be monitored to detect uneven powder beds caused by defects in each powder layer. Feedback loops can be utilized to mitigate such uneven surface by adjusting the powder spreading parameters.

In addition to using pre-developed HEA powders, DED can use pristine constituent elemental powders to print HEA products through *in situ* alloying. The powder delivery from the different channels can be monitored to ensure that the constituent element ratios are consistent. The focus point for the flow of different powders should also be monitored and aligned to the laser beam. Besides, the solidification behaviors of melt pools in DED will be different for HEA powders and elemental powders, which should be monitored to obtain insight on the underlying metallurgical mechanisms.

Numerical modelling on the phase stability of designed HEAs, flow behavior of developed HEA powders, solidification of melt pools in printing processes and mechanical properties of printed HEA products can be conducted at different scales. The prediction on the phase stability of the designed HEAs at the atomic-scale via density functional theory using CALPHAD modelling is a promising strategy to screen out unqualified HEAs. The flow behavior of HEA powder particles during the powder spreading process of PBF can be predicted by the discrete element method at the meso-scale, with regard to the contact forces and cohesion forces between neighboring particles. Incidentally, the thermodynamic behavior of HEA melt pools in DED and PBF can be predicted by computational fluid dynamics at the meso-scale to understand each printing process and provide feedback to the process optimization. Particularly for DED, the thermodynamic behavior of the melt pools generated from elemental powders are distinct to those generated from HEA powders, which requires the development of new computational models for a better understanding.

HEA phase diagrams on quaternary or higher systems can be developed to provide guidance regarding the solidification behaviors of the HEAs during 3D printing. The crystal growth and phase transformations in HEA melt pools can be simulated through cellular automata and phase field methods respectively at the micro-scale. Thermo-mechanical models for calculating the residual stress present in printed products can be established using the finite element method at the macro-scale to comprehend the complex interaction between the transient thermal history and build-up of stress within the products. The mechanical properties of printed products, such as tensile, compressive, fatigue and wear properties, can be predicted by finite element analysis at the macro-scale to estimate the failure mechanisms of printed HEA products.

Machine learning can be introduced to accelerate the development of new HEAs for 3D printing. A comprehensive database consisting of HEA information (atomic size difference, mixing entropy, mixing enthalpy, valence electron concentration, electronegativity difference,

etc.), printing methods (DED, SLM, EBM, etc.), printing process parameters (laser/electron beam power, scanning speed, hatch space, layer thickness, etc.) and mechanical properties of printed HEA products (strength, ductility, fatigue life, wear resistance, etc.) can be established for the training of machine learning models. Machine learning can be used for fast prediction of new 3D-printed HEA products, based on the database generated from numerical modelling predictions, and experimental printing and characterizations. A model will be developed or selected from the exsisting well-known models (linear regression model, polynomial regression model, support vector regression with a linear kernel, polynomial kernel or radial basis function kernel, regression tree model, back propagation neural network model, k-nearest neighbor model, etc.) to train the machine with the database towards specific industrial applications, so that the machine is capable of linking 3D printing and new HEA products with superb mechanical properties for ranking and selection.

It is hoped that the recent progress on the 3D printing of HEAs would induce more research interest and efforts into the topic, thereby refining its applicapability in a broad range of industries.

Acknowledgement

This review is supported by the National Research Foundation, Prime Minister's Office, Singapore under its Medium-Sized Centre funding scheme through the Marine and Offshore Program..

Received: ((will be filled in by the editorial staff))
Revised: ((will be filled in by the editorial staff))
Published online: ((will be filled in by the editorial staff))

References

[1] Y. Kim, H. Yuk, R. Zhao, S. A. Chester, X. Zhao, *Nature* **2018**, *558*, 274.

[2] E. MacDonald, R. Wicker, *Science* **2016**, *353*, aaf2093.

[3] C. K. Chua, K. F. Leong, *3D Printing and Additive Manufacturing: Principles and Applications Fifth Edition of Rapid Prototyping*, World Scientific Publishing, River Edge, NJ, USA **2017**.

[4] Z. X. Khoo, J. E. Teoh, Y. Liu, C. K. Chua, S. Yang, J. An, K. F. Leong, W. Y. Yeong, *Virtual Phys. Prototyping* **2015**, *10*, 103.

[5] S. Yuan, C. K. Chua, K. Zhou, *Adv. Mater. Technol*. **2019,** *4*, 1800419.

[6] J. Y. Lee, W. S. Tan, J. An, C. K. Chua, C. Y. Tang, A. G. Fane, T. H. Chong, *J. Membr. Sci.* **2016,** *499*, 480.

[7] J. Y. Lee, J. An, C. K. Chua, *Appl. Mater. Today.* **2017**, *7*, 120.

[8] H. W. Tan, T. Tran, C. K. Chua, *Virtual Phys. Prototyping* **2016**, *11*, 271.

[9] N. Saengchairat, T. Tran, C. K. Chua, *Virtual Phys. Prototyping* **2017**, *12*, 31.

[10] X. Tian, J. Jin, S. Yuan, C. K. Chua, S. B. Tor, K. Zhou, *Adv. Energy Mater*. **2017**, *7*, 1700127.

[11] C. Y. Yap, C. K. Chua, Z. L. Dong, Z. H. Liu, D. Q. Zhang, L. E. Loh, S. L. Sing, *Appl. Phys. Rev.* **2015**, *2*, 041101.

[12] I. ASTM, *Standard Terminology for Additive Manufacturing-General Principles-Terminology*, ASTM International, West Conshohocken, USA **2015**.

[13] D. Bourell, J. P. Kruth, M. Leu, G. Levy, D. Rosen, A. M. Beese, A. Clare, *CIRP Ann* **2017**, *66*, 659.

[14] H. W. Tan, J. An, C. K. Chua, T. Tran, *Adv. Electron. Mater.* **2019**, *5*, 1800831.

[15] H. W. Tan, N. Saengchairat, G. L. Goh, J. An, C. K. Chua, T. Tran, *Adv. Mater. Technol*. **2019**, 1900897.

[16] S. Yuan, F. Shen, C. K. Chua, K. Zhou, *Prog. Polym. Sci.* **2019**, *91*, 141.

[17] J. E. M. Teoh, J. An, C. K. Chua, M. Lv, V. Krishnasamy, Y. Liu, *Virtual Phys. Prototyping* **2017**, *12*, 61.

[18] W. H. Yu, S. L. Sing, C. K. Chua, C. N. Kuo, X. L. Tian, *Prog. Mater. Sci*. **2019**, *104*, 330.

[19] C. Han, Q. Wang, B. Song, W. Li, Q. Wei, S. Wen, J. Liu, Y. Shi, *J. Mech. Behav. Biomed. Mater.* **2017**, *71*, 85.

[20] C. Han, Y. Li, Q. Wang, D. Cai, Q. Wei, L. Yang, S. Wen, J. Liu, Y. Shi, *Mater. Des.* **2018**, *141*, 256.

[21] M. Vaezi, S. Chianrabutra, B. Mellor, S. Yang, *Virtual Phys. Prototyping* **2013**, *8*, 19.

[22] A. Mostafaei, K. A. Kimes, E. L. Stevens, J. Toman, Y. L. Krimer, K. Ullakko, M. Chmielus, *Acta Mater.* **2017**, *131*, 482.

[23] R. R. Dehoff, S. S. Babu, *Acta Mater.* **2010**, *58*, 4305.

[24] A. Salmi, F. Calignano, M. Galat, E. Atzeni, *Virtual Phys. Prototyping* **2018**, *13*, 191.

[25] S. Zhao, S. Li, S. Wang, W. Hou, Y. Li, L. Zhang, Y. Hao, R. Yang, R. D. K. Misra, L. E. Murr,

Acta Mater. **2018**, *150*, 1.

[26] L. Liu, Q. Ding, Y. Zhong, J. Zou, J. Wu, Y. Chiu, J. Li, Z. Zhang, Q. Yu, Z. Shen, *Mater. Today* **2018**, *21*, 354.

[27] A. S. Sharma, S. Yadav, K. Biswas, B. Basu, *Mater. Sci. Eng. R* **2018**, *131*, 1.

[28] M. J. Bermingham, D. Kent, H. Zhan, D. H. StJohn, M. S. Dargusch, *Acta Mater.* **2015**, *91*, 289.

[29] B. E. Carroll, T. A. Palmer, A. M. Beese, *Acta Mater.* **2015**, *87*, 309.

[30] T. DebRoy, H. Wei, J. S. Zuback, T. Mukherjee, J. W. Elmer, J. O. Milewski, A. M. Beese, A. Wilson-Heid, A. De, W. Zhang, *Prog. Mater. Sci.* **2018**, *92*, 112.

[31] D. Herzog, V. Seyda, E. Wycisk, C. Emmelmann, *Acta Mater.* **2016**, *117*, 371.

[32] S. Liu, Y. C. Shin, *Mater. Des.* **2019**, *164*, 107552.

[33] B. Song, X. Zhao, S. Li, C. Han, Q. Wei, S. Wen, J. Liu, Y. Shi, *Front. Mech. Eng.* **2015**, *10*, 111.

[34] M. Das, V. K. Balla, D. Basu, S. Bose, A. Bandyopadhyay, *Scr. Mater.* **2010**, *63*, 438.

[35] B. Cheng, J. Lydon, K. Copper, V. Cole, P. Northrop, K. Chou, *Virtual Phys. Prototyping* **2018**, *13*, 8.

[36] D. Gu, W. Meiners, K. Wissenbach, R. Poprawe, *Int. Mater. Rev.* **2012**, *57*, 133.

[37] J. O. Milewski, *Additive Manufacturing of Metals*, Springer, New York, NJ, USA **2017**.

[38] W. L. Ng, C. K. Chua, Y. F. Shen, *Prog. Polym. Sci.* **2019**, *97*, 101145.

[39] S. Guo, C. Ng, J. Lu, C. Liu, *J. Appl. Phys.* **2011**, *109*, 103505.

[40] X. Gao, Y. Lu, B. Zhang, N. Liang, G. Wu, G. Sha, J. Liu, Y. Zhao, *Acta Mater.* **2017**, *141*, 59.

[41] S. Wu, G. Wang, Q. Wang, Y. Jia, J. Yi, Q. Zhai, J. Liu, B. Sun, H. Chu, J. Shen, P. K. Liaw, C. Liu, T. Zhang, *Acta Mater.* **2019**, *165*, 444.

[42] O. El-Atwani, N. Li, M. Li, A. Devaraj, J. K. S. Baldwin, M. M. Schneider, D. Sobieraj, J. S. Wróbel, D. Nguyen-Manh, S. A. Maloy, E. Martinez, *Sci. Adv.* **2019**, *5*, eaav2002.

[43] S. Shafeie, S. Guo, P. Erhart, Q. Hu, A. Palmqvist, *Adv. Mater.* **2019**, *31*, 1805392.

[44] F. He, D. Chen, B. Han, Q. Wu, Z. Wang, S. Wei, D. Wei, J. Wang, C. Liu, J. Kai, *Acta Mater.* **2019**, *167*, 275.

[45] M. C. Gao, *High-Entropy Alloys*, Springer, New York, NJ, USA **2016**.

[46] O. N. Senkov, G. B. Wilks, J. M. Scott, D. B. Miracle, *Intermetallics* **2011**, *19*, 698.

[47] Y. Yuan, Y. Wu, X. Tong, H. Zhang, H. Wang, X. Liu, L. Ma, H. Suo, Z. Lu, *Acta Mater.* **2017**, *125*, 481.

[48] J. Yeh, S. Chen, S. Lin, J. Gan, T. S. Chin, T. Shun, C. H. Tsau, S. Chang, *Adv. Eng. Mater.* **2004**, *6*, 299.

[49] J. Yeh, *JOM* **2013**, *65*, 1759.

[50] Z. Lei, X. Liu, Y. Wu, H. Wang, S. Jiang, S. Wang, X. Hui, Y. Wu, B. Gault, P. Kontis, D. Raabe, L. Gu, Q. Zhang, H. Chen, H. Wang, J. Liu, K. An, Q. Zeng, T. Nie, Z. Lu, *Nature* **2018**, *563*, 546.

[51] D. B. Miracle, O. N. Senkov, *Acta Mater.* **2017**, *122*, 448.

[52] S. Praveen, H. S. Kim, *Adv. Eng. Mater.* **2018**, *20*, 1700645.

[53] Z. Li, K. G. Pradeep, Y. Deng, D. Raabe, C. C. Tasan, *Nature* **2016**, *534*, 227.

[54] Y. Ye, Q. Wang, J. Lu, C. T. Liu, Y. Yang, *Mater. Today* **2016**, *19*, 349.

[55] P. Koželj, S. Vrtnik, A. Jelen, S. Jazbec, Z. Jagličić, S. Maiti, M. Feuerbacher, W. Steurer, J. Dolinšek, *Phys. Rev. Lett.* **2014**, *113*, 107001.

[56] B. Gludovatz, A. Hohenwarter, D. Catoor, E. H. Chang, E. P. George, *Science* **2014**, *345*, 1153.

[57] S. Xia, Z. Wang, T. Yang, Y. Zhang, *J. Iron Steel Res. Int.* **2015**, *22*, 879.

[58] J. W. Yeh, S. J. Lin, *J. Mater. Res.* **2018**, *33*, 3129.

[59] A. Kumar, M. Gupta, *Metals* **2016**, *6*, 199.

[60] Y. Zhang, T. Zuo, Z. Tang, M. C. Gao, K. A. Dahmen, P. K. Liaw, Z. P. Lu, *Prog. Mater. Sci.* **2014**, *61*, 1.

[61] Y. Zou, *J. Mater. Res.* **2018**, *33*, 3035.

[62] J. Chen, X. Zhou, W. Wang, B. Liu, Y. Lv, W. Yang, D. Xu, Y. Liu, *J. Alloy. Compd.* **2018**, *760*, 15.

[63] J. W. Yeh, *Ann. Chim. Sci. Mat.* **2006**, *31*, 633.

[64] X. Li, *Adv. Eng. Mater.* **2018**, *20*, 1700874.

[65] S. Chen, Y. Tong, P. K. Liaw, *Entropy* **2018**, *20*, 937.

[66] W. Zhang, P. K. Liaw, Y. Zhang, *Sci. China Mater.* **2018**, *61*, 2.

[67] E. O. Olakanmi, *J. Mater. Process. Technol.* **2013**, *213*, 1387.

[68] A. Mostafaei, J. Toman, E. L. Stevens, E. T. Hughes, Y. L. Krimer, M. Chmielus, *Acta Mater.* **2017**, *124*, 280.

[69] M. C. H. Karg, A. Munk, B. Ahuja, M. V. Backer, J. P. Schmitt, C. Stengel, S. V. Kuryntsev, M. Schmidt, *J. Mater. Process. Technol.* **2019**, *264*, 155.

[70] X. Li, K. Yang, H. Lin, H. Ma, Y. Han, Q. He, *J. Mater. Eng. Perform.* **2019**, *28*, 12.

[71] C. Si, X. Tang, X. Zhang, J. Wang, W. Wu, *Mater. Des.* **2017**, *118*, 66.

[72] Y. Yu, G. Li, Y. Wang, J. Ding, *Appl. Math Model.* **2016**, *40*, 268.

[73] J. Shinjo, A. Umemura, *Int. J. Multiph Flow* **2011**, *37*, 1294.

[74] D. Yim, M. J. Jang, J. W. Bae, J. Moon, C. H. Lee, S. J. Hong, S. Hong, H. S. Kim, *Mater. Chem. Phys.* **2018**, *210*, 95.

[75] P. Wang, P. Huang, F. L. Ng, W. J. Sin, S. Lu, M. L. S. Nai, Z. Dong, J. Wei, *Mater. Des.* **2019**, *168*, 107576.

[76] P. Ding, A. Mao, X. Zhang, X. Jin, B. Wang, M. Liu, X. Gu, *J. Alloy. Compd.* **2017**, *721*, 609.

[77] C. Yang, J. L. H. Chau, C. Weng, C. Chen, Y. Chou, *Mater. Chem. Phys.* **2017**, *202*, 151.

[78] T. Li, Y. Liu, B. Liu, W. Guo, L. Xu, *Coatings* **2017**, *7*, 151.

[79] S. Zhou, P. Zhang, Y. Xue, F. Wang, W. Lu, T. Cao, Z. Tan, B. Cheng, B. Wang, *Trans. Nonferrous Met. Soc. China* **2018**, *28*, 939.

[80] I. Kunce, M. Polanski, K. Karczewski, T. Plocinski, K. J. Kurzydlowski, *J. Alloy. Compd.* **2015**, *648*, 751.

[81] T. Fujieda, H. Shiratori, K. Kuwabara, T. Kato, K. Yamanaka, Y. Koizumi, A. Chiba, *Mater. Lett.* **2015**, *159*, 12.

[82] K. Kuwabara, H. Shiratori, T. Fujieda, K. Yamanaka, Y. Koizumi, A. Chiba, *Addit. Manuf.* **2018**, *23*, 264.

[83] H. Shiratori, T. Fujieda, K. Yamanaka, Y. Koizumi, K. Kuwabara, T. Kato, A. Chiba, *Mater. Sci. Eng. A* **2016**, *656*, 39.

[84] P. Zhou, D. Xiao, P. Zhou, T. Yuan, *Ceram. Int.* **2018**, *44*, 17160.

[85] P. Zhou, D. Xiao, Z. Wu, X. Ou, *Mater. Sci. Eng. A* **2019**, *739*, 86.

[86] C. Li, K. C. Chang, A. C. Yeh, *J. Alloy. Compd.* **2019**, *782*, 440.

[87] B. Liu, J. Wang, Y. Liu, Q. Fang, Y. Wu, S. Chen, C. Liu, *Intermetallics* **2016**, *75*, 25.

[88] N. Eißmann, B. Klöden, T. Weißgärber, B. Kieback, *Powder Metall.* **2017**, *60*, 184.

[89] Y. Liu, J. Wang, Q. Fang, B. Liu, Y. Wu, S. Chen, *Intermetallics* **2016**, *68*, 16.

[90] R. Li, P. Niu, T. Yuan, P. Cao, C. Chen, K. Zhou, *J. Alloy. Compd.* **2018**, *746*, 125.

[91] T. G. Park, S. H. Lee, B. Lee, H. M. Cho, W. J. Cho, B. S. Kim, K. S. Shin, T. S. Kim, *Arch. Metall. Mater.* **2018**, *63*, 1055.

[92] Z. Zhu, Q. B. Nguyen, F. L. Ng, X. An, X. Liao, P. K. Liaw, S. M. L. Nai, J. Wei, *Scr. Mater.* **2018**, *154*, 20.

[93] R. Zhou, Y. Liu, C. Zhou, S. Li, W. Wu, M. Song, B. Liu, X. Liang, P. K. Liaw, *Intermetallics* **2018**, *94*, 165.

[94] A. E. Berkowitz, J. C. Grande, S. A. Miller, R. J. Murphy, J. L. Walter, *Mater. Sci. Eng.* **1984**, *62*, 217.

[95] Y. F. Kao, T. J. Chen, S. K. Chen, J. W. Yeh, *J. Alloy. Compd.* **2009**, *488*, 57.

[96] H. P. Chou, Y. S. Chang, S. K. Chen, J. W. Yeh, *Mater. Sci. Eng. B* **2009**, *163*, 184.

[97] W. R. Wang, W. L. Wang, S. C. Wang, Y. C. Tsai, C. H. Lai, J. W. Yeh, *Intermetallics* **2012**, *26*, 44.

[98] M. Boisvert, D. Christopherson, P. Beaulieu, G. L'Espérance, *Mater. Des.* **2017**, *116*, 644.

[99] A. Mostafaei, C. Hilla, E. L. Stevens, P. Nandwana, A. M. Elliott, M. Chmielus, *Powder Technol.* **2018**, *333*, 180.

[100] T. Durejko, J. Aniszewska, M. Ziętala, A. Antolak-Dudka, T. Czujko, R. A. Varin, V. Paserin, *Materials* **2018**, *11*, 12.

[101] S. Hoeges, A. Zwiren, C. Schade, *Metal Powder Rep.* **2017**, *72*, 111.

[102] D. Gu, Z. Wang, Y. Shen, Q. Li, Y. Li, *Appl. Surf. Sci.* **2009**, *255*, 9230.

[103] C. Ma, D. Gu, D. Dai, W. Chen, *J. Mater. Res.* **2015**, *30*, 2816.

[104] H. Wang, D. Gu, *J. Compos Mater.* **2015**, *49*, 1639.

[105] S. Varalakshmi, M. Kamaraj, B. S. Murty, *J. Alloy. Compd.* **2008**, *460*, 253.

[106] Y. L. Chen, Y. H. Hu, C. A. Hsieh, J. W. Yeh, S. K. Chen, *J. Alloy. Compd.* **2009**, *481*, 768.

[107] Y. Tong, P. Qi, X. Liang, Y. Chen, Y. Hu, Z. Hu, *Materials* **2018**, *11*, 1250.

[108] B. Zhang, Y. Duan, Y. Cui, G. Ma, T. Wang, X. Dong, *Mater. Des.* **2018**, *149*, 173.

[109] V. Shivam, J. Basu, Y. Shadangi, M. K. Singh, N. K. Mukhopadhyay, *J. Alloy. Compd.* **2018**, *757*, 87.

[110] M. Vaidya, G. M. Muralikrishna, B. S. Murty, *J. Mater. Res.* **2019**, *34*, 664.

[111] S. H. Joo, H. Kato, M. J. Jang, J. Moon, E. B. Kim, S. J. Hong, H. S. Kim, *J. Alloy. Compd.* **2017**, *698*, 591.

[112] C. Suryanarayana, *Prog. Mater. Sci.* **2001**, *46*, 1.

[113] W. R. Wang, W. L. Wang, J. W. Yeh, *J. Alloy. Compd.* **2014**, *589*, 143.

[114] R. Zhao, B. Ren, G. Zhang, Z. Liu, J. Zhang, *J. Magn. Magn. Mater.* **2018**, *468*, 14.

[115] C. Sun, P. Li, S. Xi, Y. Zhou, S. Li, X. Yang, *Mater. Sci. Eng. A* **2018**, *728*, 144.

[116] S. Praveen, B. S. Murty, R. S. Kottada, *Mater. Sci. Eng. A* **2012**, *534*, 83.

[117] M. D. Alcalá, C. Real, I. Fombella, I. Trigo, J. M. Córdoba, *J. Alloy. Compd.* **2018**, *749*, 834.

[118] L. Tian, M. Fu, W. Xiong, *Materials* **2018**, *11*, 320.

[119] S. Nam, M. J. Kim, J. Y. Hwang, H. Choi, *J. Alloy. Compd.* **2018**, *762*, 29.

[120] M. Murali, S. P. Kumaresh Babu, J. Majhi, A. Vallimanalan, R. Mahendran, *Powder Metall.* **2018**, *61*, 139.

[121] A. Raza, B. Kang, J. Lee, H. J. Ryu, S. H. Hong, *Mater. Des.* **2018**, *145*, 11.

[122] B. Zhang, Y. Duan, Y. Cui, G. Ma, T. Wang, X. Dong, *RSC Adv.* **2018**, *8*, 14936.

[123] T. Lu, S. Scudino, W. Chen, P. Wang, D. Li, M. Mao, L. Kang, Y. Liu, Z. Fu, *Mater. Sci. Eng. A* **2018**, *726*, 126.

[124] W. Wang, B. Li, S. Zhai, J. Xu, Z. Niu, J. Xu, Y. Wang, *Met. Mater. Int.* **2018**, *24*, 1112.

[125] P. Wang, X. Cheng, H. Cai, Y. Xue, Y. Zhang, *Mater. Sci. Eng. A* **2017**, *708*, 523.

[126] C. D. Gómez-Esparza, F. Baldenebro-López, L. González-Rodelas, J. Baldenebro-López, R. Martínez-Sánchez, *Mater. Res.* **2016**, *19*, 39.

[127] F. Salemi, M. H. Abbasi, F. Karimzadeh, *J. Alloy. Compd.* **2016**, *685*, 278.

[128] D. Kumar, O. Maulik, A. S. Bagri, Y. Prasad, V. Kumar, *Mater. Today Proc.* **2016**, *3*, 2926.

[129] S. Yadav, A. Kumar, K. Biswas, *Mater. Chem. Phys.* **2018**, *210*, 222.

[130] W. Ge, B. Wu, S. Wang, S. Xu, C. Shang, Z. Zhang, Y. Wang, *Adv. Powder Technol.* **2017**, *28*, 2556.

[131] G. M. Karthik, S. Panikar, G. D. J. Ram, R. S. Kottada, *Mater. Sci. Eng. A* **2017**, *679*, 193.

[132] S. Praveen, B. S. Murty, R. S. Kottada, *JOM* **2013**, *65*, 1797.

[133] Z. Szklarz, J. Lekki, P. Bobrowski, M. B. Szklarz, L. Rogal, *Mater. Chem. Phys.* **2018**, *215*, 385.

[134] H. Cheng, W. Chen, X. Liu, Q. Tang, Y. Xie, P. Dai, *Mater. Sci. Eng. A* **2018**, *719*, 192.

[135] R. K. Mishra, R. R. Shahi, *J. Magn. Magn. Mater.* **2017**, *442*, 218.

[136] I. Moravcik, J. Cizek, J. Zapletal, Z. Kovacova, J. Vesely, P. Minarik, M. Kitzmantel, E.

Neubauer, I. Dlouhy, *Mater. Des.* **2017**, *119*, 141.

[137] B. Kang, J. Lee, H. J. Ryu, S. H. Hong, *Mater. Sci. Eng. A* **2018**, *712*, 616.

[138] Y. Long, K. Su, J. Zhang, X. Liang, H. Peng, X. Li, *Materials* **2018**, *11*, 669.

[139] D. Oleszak, A. Antolak-Dudka, T. Kulik, *Mater. Lett.* **2018**, *232*, 160.

[140] J. Wang, Z. Zheng, J. Xu, Y. Wang, *J. Magn. Magn. Mater.* **2014**, *355*, 58.

[141] J. Xu, E. Axinte, Z. F. Zhao, Y. Wang, *J. Magn. Magn. Mater.* **2016**, *414*, 59.

[142] Y. Y. Kaplanskii, A. V. Korotitskiy, E. A. Levashov, Z. A. Sentyurina, A. V. Samokhin, I. A. Logachev, *Mater. Sci. Eng. A* **2018**, *729*, 398.

[143] J. W. Murray, M. Simonelli, A. Speidel, D. M. Grant, A. T. Clare, *Powder Technol.* **2019**, *350*, 100.

[144] S. J. Wolff, S. Lin, E. J. Faierson, W. K. Liu, G. J. Wagner, J. Cao, *Acta Mater.* **2017**, *132*, 106.

[145] G. Garechana, R. Río-Belver, I. Bildosola, E. Cilleruelo-Carrasco, *PloS one* **2019**, *14*, e0210441.

[146] M. Galati, L. Iuliano, *Addit. Manuf.* **2018**, *19*, 1.

[147] N. Raghavan, R. Dehoff, S. Pannala, S. Simunovic, M. Kirka, J. Turner, N. Carlson, S. S. Babu, *Acta Mater.* **2016**, *112*, 303.

[148] M. L. Griffith, D. M. Keicher, C. L. Atwood, J. A. Romero, J. E. Smugeresky, L. D. Harwell, D. L. Greene, presented at 1996 Int. Solid Freeform Fabrication Symp., Austin, Texas, USA, August, **1996**.

[149] H. Dobbelstein, E. L. Gurevich, E. P. George, A. Ostendorf, G. Laplanche, *Addit. Manuf.* **2019**, *25*, 252.

[150] R. Wang, K. Zhang, C. Davies, X. Wu, *J. Alloy. Compd.* **2017**, *694*, 971.

[151] V. Ocelik, N. Janssen, S. N. Smith, J. T. M. De Hosson, *JOM* **2016**, *68*, 1810.

[152] T. Borkar, V. Chaudhary, B. Gwalani, D. Choudhuri, C. V. Mikler, V. Soni, T. Alam, R. V. Ramanujan, R. Banerjee, *Adv. Eng. Mater.* **2017**, *19*, 1700048.

[153] J. Joseph, T. Jarvis, X. H. Wu, N. Stanford, P. Hodgson, D. M. Fabijanic, *Mater. Sci. Eng. A* **2015**, *633*, 184.

[154] Q. Chao, T. Guo, T. Jarvis, X. Wu, P. Hodgson, D. M. Fabijanic, *Surf. Coat. Technol.* **2017**, *332*, 440.

[155] J. Li, W. Craeghs, C. Jing, S. Gong, F. H. Shan, *Mater. Des.* **2017**, *117*, 363.

[156] B. Gwalani, V. Soni, O. A. Waseem, S. A. Mantri, R. Banerjee, *Opt. Laser Technol.* **2019**, *113*, 330.

[157] C. Haase, F. Tang, M. B. Wilms, A. Weisheit, B. Hallstedt, *Mater. Sci. Eng. A* **2017**, *688*, 180.

[158] B. A. Welk, M. A. Gibson, H. L. Fraser, *JOM* **2016**, *68*, 1021.

[159] I. Kunce, M. Polanski, J. Bystrzycki, *Int. J. Hydrog. Energy* **2014**, *39*, 9904.

[160] I. Kunce, M. Polanski, J. Bystrzycki, *Int. J. Hydrog. Energy* **2013**, *38*, 12180.

[161] I. Kunce, M. Polanski, T. Czujko, *Int. J. Hydrog. Energy* **2017**, *42*, 27154.

[162] M. E. Glicksman, *Principles of solidification*, Springer, New York, NJ, USA **2010**.

[163] T. Borkar, B. Gwalani, D. Choudhuri, C. V. Mikler, C. J. Yannetta, X. Chen, R. V. Ramanujan, M. J. Styles, M. A. Gibson, R. Banerjee, *Acta Mater.* **2016**, *116*, 63.

[164] H. R. Sistla, J. W. Newkirk, F. Frank Liou, *Mater. Des.* **2015**, *81*, 113.

[165] B. Gwalani, S. Gangireddy, S. Shukla, C. J. Yannetta, S. G. Valentin, R. S. Mishra, R. Banerjee, *Mater. Today Commun.* **2019**, *20*, 100602.

[166] A. Mohanty, J. K. Sampreeth, O. Bembalge, J. Y. Hascoet, S. Marya, R. J. Immanuel, S. K. Panigrahi, *Surf. Coat. Technol.* **2019**, *380*, 125028.

[167] H. Dobbelstein, M. Thiele, E. L. Gurevich, E. P. George, A. Ostendorf, *Phys. Procedia* **2016**, *83*, 624.

[168] H. Dobbelstein, E. L. Gurevich, E. P. George, A. Ostendorf, G. Laplanche, *Addit. Manuf.* **2018**, *24*, 386.

[169] A. Amar, J. Li, S. Xiang, X. Liu, Y. Zhou, G. Le, X. Wang, F. Qu, S. Ma, W. Dong, Q. Li, *Intermetallics* **2019**, *109*, 162.

[170] J. Li, S. Xiang, H. Luan, A. Amar, X. Liu, S. Lu, Y. Zeng, G. Le, X. Wang, F. Qu, C. Jiang, *J. Mater. Sci. Technol.* **2019**, *35*, 2430.

[171] J. Joseph, N. Stanford, P. Hodgson, D. M. Fabijanic, *Scr. Mater.* **2017**, *129*, 30.

[172] X. Chen, L. Yan, S. Karnati, Y. Zhang, F. Liou, *Coatings* **2017**, *7*, 47.

[173] S. Xiang, H. Luan, J. Wu, K. Yao, J. Li, X. Liu, Y. Tian, W. Mao, H. Bai, G. Le, Q. Li, *J. Alloy. Compd.* **2019**, *773*, 387.

[174] Y. Chew, G. J. Bi, Z. Zhu, F. L. Ng, F. Weng, S. Liu, S. M. L. Nai, B. Y. Lee, *Mater. Sci. Eng. A* **2019**, *744*, 137.

[175] S. Guan, D. Wan, K. Solberg, F. Berto, T. Welo, T. M. Yue, K. C. Chan, *Mater. Sci. Eng. A* **2019**, *761*, 138056.

[176] S. Saedi, N. S. Moghaddam, A. Amerinatanzi, M. Elahinia, H. E. Karaca, *Acta Mater.* **2018**, *144*, 552.

[177] C. Han, Y. Li, Q. Wang, S. Wen, Q. Wei, C. Yan, L. Hao, J. Liu, Y. Shi, *J. Mech. Behav. Biomed. Mater.* **2018**, *80*, 119.

[178] C. N. Kuo, C. K. Chua, P. C. Peng, Y. W. Chen, S. L. Sing, S. Huang, Y. L. Su, *Virtual Phys. Prototyping* **2020**, *15*, 120.

[179] Z. Sun, X. Tan, S. B. Tor, C. K. Chua, *NPG Asia Mater.* **2018**, *10*, 127.

[180] Y. Li, K. Zhou, P. Tan, S. B. Tor, C. K. Chua, K. F. Leong, *Int. J. Mech. Sci.* **2018**, *136*, 24.

[181] P. Tan, F. Shen, B. Li, K. Zhou, *Mater. Des.* **2019**, *168*, 107642.

[182] J. Wang, W. J. Wu, W. Jing, X. Tan, G. J. Bi, S. B. Tor, K. F. Leong, C. K. Chua, E. Liu, *Mater. Sci. Eng. A* **2019**, *746*, 300.

[183] C. Han, Y. Yao, X. Cheng, J. Luo, P. Luo, Q. Wang, F. Yang, Q. Wei, Z. Zhang, *Biomacromolecules* **2017**, *18*, 3776.

[184] C. Han, C. Yan, S. Wen, T. Xu, S. Li, J. Liu, Q. Wei, Y. Shi, *Rapid Prototyping J.* **2017**, *23*, 16.

[185] Y. Wang, T. Voisin, J. T. McKeown, J. Ye, N. P. Calta, Z. Li, Z. Zeng, Y. Zhang, W. Chen, T. T. Roehling, R. T. Ott, M. K. Santala, P. J. Depond, M. J. Matthews, A. V. Hamza, T. Zhu, *Nat. Mater.* **2018**, *17*, 63.

[186] J. H. Martin, B. D. Yahata, J. M. Hundley, J. A. Mayer, T. A. Schaedler, T. M. Pollock, *Nature* **2017**, *549*, 365.

[187] Y. Brif, M. Thomas, I. Todd, *Scr. Mater.* **2015**, *99*, 93.

[188] A. Piglione, B. Dovgyy, C. Liu, C. M. Gourlay, P. A. Hooper, M. S. Pham, *Mater. Lett.* **2018**, *224*, 22.

[189] L. Johnson, M. Mahmoudi, B. Zhang, R. Seede, X. Huang, J. T. Maier, H. J. Maier, I. Karaman, A. Elwany, R. Arróyave, *Acta Mater.* **2019**, *176*, 199.

[190] S. A. Khairallah, A. T. Anderson, A. Rubenchik, W. E. King, *Acta Mater.* **2016**, *108*, 36.

[191] M. T. Andani, R. Dehghani, M. R. Karamooz-Ravari, R. Mirzaeifar, J. Ni, *Addit. Manuf.* **2018**, *20*, 33.

[192] M. Simonelli, C. Tuck, N. T. Aboulkhair, I. Maskery, I. Ashcroft, R. D. Wildman, R. Hague, *Metall. Mater. Trans. A* **2015**, *46*, 3842.

[193] P. Niu, R. Li, T. Yuan, S. Zhu, C. Chen, M. Wang, L. Huang, *Intermetallics* **2019**, *104*, 24.

[194] Y. K. Kim, J. Choe, K. A. Lee, *J. Alloy. Compd.* **2019**, *805*, 680.

[195] D. Karlsson, A. Marshal, F. Johansson, M. Schuisky, M. Sahlberg, J. M. Schneider, U. Jansson, *J. Alloy. Compd.* **2019**, *784*, 195.

[196] M. Zhang, X. Zhou, D. Wang, W. Zhu, J. Li, Y. Zhao, *Mater. Sci. Eng. A* **2019**, *743*, 773.

[197] S. Luo, P. Gao, H. Yu, J. Yang, Z. Wang, X. Zeng, *J. Alloy. Compd.* **2019**, *771*, 387.

[198] S. Ewald, F. Kies, S. Hermsen, M. Voshage, C. Haase, J. H. Schleifenbaum, *Materials* **2019**, *12*, 1706.

[199] P. K. Sarswat, S. Sarkar, A. Murali, W. K. Huang, W. D. Tan, M. L. Free, *Appl. Surf. Sci.* **2019**, *476*, 242.

[200] Z. Sun, X. Tan, M. Descoins, D. Mangelinck, S. B. Tor, C. S. Lim, *Scr. Mater.* **2019**, *168*, 129.

[201] B. Li, B. Qian, Y. Xu, Z. Liu, F. Xuan, *Mater. Lett.* **2019**, *252*, 88

[202] W. Wu, R. Zhou, B. Wei, S. Ni, Y. Liu, M. Song, *Mater. Charact.* **2018**, *144*, 605.

[203] T. Fujieda, M. Chen, H. Shiratori, K. Kuwabara, K. Yamanaka, Y. Koizumi, A. Chiba, S. Watanabe, *Addit. Manuf.* **2019**, *25*, 412.

[204] H. Zhang, Y. Zhao, S. Huang, S. Zhu, F. Wang, D. Li, *Materials* **2019**, *12*, 720.

[205] X. Yang, Y. Zhou, S. Xi, Z. Chen, P. Wei, C. He, T. Li, Y. Gao, H. Wu, *Mater. Sci. Eng. A* **2019**, *767*, 138394.

[206] X. Yang, Y. Zhou, S. Xi, Z. Chen, P. Wei, C. He, T. Li, Y. Gao, H. Wu, *Mater. Sci. Eng. A* **2019**, *767*, 138382.

[207] Y. Zhou, Z. Zhang, Y. Wang, G. Liu, S. Zhou, Y. Li, J. Shen, M. Yan, *Addit. Manuf.* **2019**, *25*, 204.

[208] H. Zhang, W. Xu, Y. Xu, Z. Lu, D. Li, *Int. J. Adv. Manuf. Technol.* **2018**, *96*, 461.

[209] J. Guo, M. H. Goh, Z. Zhu, X. H. Lee, M. L. S. Nai, J. Wei, *Mater. Des.* **2018**, *153*, 211.

[210] X. Tan, Y. Kok, Y. J. Tan, M. Descoins, D. Mangelinck, S. B. Tor, K. F. Leong, C. K. Chua, *Acta Mater.* **2015**, *97*, 1.

[211] L. E. Murr, S. M. Gaytan, D. A. Ramirez, E. Martinez, J. Hernandez, K. N. Amato, P. W. Shindo, F. R. Medina, R. B. Wicker, *J. Mater. Sci. Technol.* **2012**, *28*, 1.

[212] W. J. Sames, F. A. List, S. Pannala, R. R. Dehoff, S. S. Babu, *Int. Mater. Rev.* **2016**, *61*, 315.

[213] T. Fujieda, H. Shiratori, K. Kuwabara, M. Hirota, T. Kato, K. Yamanaka, Y. Koizumi, A. Chiba, S. Watanabe, *Mater. Lett.* **2017**, *189*, 148.

[214] S. S. Al-Bermani, M. L. Blackmore, W. Zhang, I. Todd, *Metall. Mater. Trans. A* **2010**, *41*, 3422.

[215] A. A. Antonysamy, *Degree of Doctor of Philosophy*, The University of Manchester (UK), **2012**.

[216] V. V. Popov, A. Katz-Demyanetz, A. Koptyug, M. Bamberger, *Heliyon* **2019**, *5*, e01188.

[217] C. Kenel, N. P. M. Casati, D. C. Dunand, *Nat. Commun.* **2019**, *10*, 904.

[218] D. Karlsson, G. Lindwall, A. Lundbäck, M. Amnebrink, M. Boström, L. Riekehr, M. Schuisky, M. Sahlberg, U. Jansson, *Addit. Manuf.* **2019**, *27*, 72.

[219] N. Hrabe, T. Gnäupel-Herold, T. Quinn, *Int. J. Fatigue* **2017**, *94*, 202.

[220] W. Ji, Z. Fu, W. Wang, H. Wang, J. Zhang, Y. Wang, F. Zhang, *J. Alloy. Compd.* **2014**, *589*, 61.

[221] V. Shivam, J. Basu, V. K. Pandey, Y. Shadangi, N. K. Mukhopadhyay, *Adv. Powder Technol.* **2018**, *29*, 2221.

[222] B. Cantor, I. T. H. Chang, P. Knight, A. J. B. Vincent, *Mater. Sci. Eng. A* **2004**, *375*, 213.

[223] J. H. Kim, K. R. Lim, J. W. Won, Y. S. Na, H. S. Kim, *Mater. Sci. Eng. A* **2018**, *712*, 108.

[224] Y. Zhou, Y. Zhang, Y. Wang, G. Chen, *Appl. Phys. Lett.* **2007**, *90*, 181904.

[225] X. Wang, Y. Zhang, Y. Qiao, G. Chen, *Intermetallics* **2007**, *15*, 357.

[226] C. C. Juan, K. K. Tseng, W. L. Hsu, M. H. Tsai, C. W. Tsai, C. M. Lin, S. K. Chen, S. J. Lin, J. W. Yeh, *Mater. Lett.* **2016**, *175*, 284.

[227] A. Zhang, J. Han, B. Su, P. Li, J. Meng, *Mater. Des.* **2017**, *114*, 253.

[228] Z. Tong, X. Ren, J. Jiao, W. Zhou, Y. Ren, Y. Ye, E. A. Larson, J. Gu, *J. Alloy. Compd.* **2019**, *785*, 1144.

[229] M. A. Melia, J. D. Carroll, S. R. Whetten, S. N. Esmaeely, J. Locke, E. White, I. Anderson, M. Chandross, J. R. Michael, N. Argibay, E. J. Schindelholz, *Addit. Manuf.* **2019**, *29*, 100833.

[230] J. Joseph, P. Hodgson, T. Jarvis, X. Wu, N. Stanford, D. M. Fabijanic, *Mater. Sci. Eng. A* **2018**, *733*, 59.

[231] J. He, W. Liu, H. Wang, Y. Wu, X. Liu, T. G. Nieh, Z. Lu, *Acta Mater.* **2014**, *62*, 105.

[232] J. Pi, Y. Pan, H. Zhang, L. Zhang, *Mater. Sci. Eng. A* **2012**, *534*, 228.

[233] J. Wang, S. Niu, T. Guo, H. Kou, J. Li, *J. Alloy. Compd.* **2017**, *710*, 144.

[234] Z. Wu, S. A. David, Z. Feng, H. Bei, *Scr. Mater.* **2016**, *124*, 81.

[235] N. Hansen, *Scr. Mater.* **2004**, *51*, 801.

[236] Z. Tang, O. N. Senkov, C. M. Parish, C. Zhang, F. Zhang, L. J. Santodonato, G. Wang, G. Zhao, F. Yang, P. K. Liaw, *Mater. Sci. Eng. A* **2015**, *647*, 229.

[237] Z. Qiu, C. Yao, K. Feng, Z. Li, P. Chu, *Int. J. Lightweight Mater. Manuf.* **2018**, *1*, 33.

[238] Y. L. Chou, Y. C. Wang, J. W. Yeh, H. C. Shih, *Corrosion Sci.* **2010**, *52*, 3481.

[239] Y. L. Chou, J. W. Yeh, H. C. Shih, *Corrosion Sci.* **2010**, *52*, 2571.

[240] Y. F. Kao, T. D. Lee, S. K. Chen, Y. S. Chan, *Corrosion Sci.* **2010**, *52*, 1026.

[241] S. Sarkar, P. K. Sarswat, M. L. Free, *Addit. Manuf.* **2019**, *30*, 100902.

[242] J. Ren, C. Mahajan, L. Liu, D. Follette, W. Chen, S. Mukherjee, *Metals* **2019**, *9*, 1029.

[243] P. Yang, Y. Liu, X. Zhao, J. Cheng, H. Li, *Adv. Powder Technol.* **2016**, *27*, 1128.

[244] P. Yang, Y. Liu, X. Zhao, J. Cheng, H. Li, *J. Mater. Res.* **2016**, *31*, 2398.

[245] P. Yang, Y Liu, X. Zhao, C. Zhang, *J. Mater. Sci. Mater. Electron.* **2017**, *28*, 9867.

[246] Y. Zhang, B. Zhang, K. Li, G. L. Zhao, S. M. Guo, *J. Alloy. Compd.* **2018**, *734*, 220.

[247] M. Sahlberg, D. Karlsson, C. Zlotea, U. Jansson, *Sci. Rep.* **2016**, *6*, 36770.

[248] Y. F. Kao, S. K. Chen, J. H. Sheu, J. T. Lin, W. E. Lin, J. W. Yeh, S. J. Lin, T. H. Liou, C. W. Wang, *Int. J. Hydrog. Energy* **2010**, *35*, 9046.

[249] C. Zlotea, M. A. Sow, G. Ek, J. P. Couzinié, L. Perrière, I. Guillot, J. Bourgon, K. T. Møller, T. R. Jensen, E. Akiba, M. Sahlberg, *J. Alloy. Compd.* **2019**, *775*, 667.

[250] E. Akiba, H. Iba, *Intermetallics* **1998**, *6*, 461.

[251] M. Uno, K. Takahashi, T. Maruyama, H. Muta, S. Yamanaka, *J. Alloy. Compd.* **2004**, *366*, 213.

[252] J. H. Kim, K. S. Han, K. T. Hwang, B. G. Kim, Y. M. Kang, *Int. J. Hydrog. Energy* **2013**, *38*, 6215.

[253] Y. Zhao, D. H. Lee, M. Y. Seok, J. A. Lee, M. P. Phaniraj, J. Y. Suh, H. Y. Ha, J. Y. Kim, U. Ramamurty, J. I. Jang, *Scr. Mater.* **2017**, *135*, 54.

[254] H. Luo, Z. Li, D. Raabe, *Sci. Rep.* **2017**, *7*, 9892.

[255] H. Luo, W. Lu, X. Fang, D. Ponge, Z. Li, D. Raabe, *Mater. Today* **2018**, *21*, 1003.

[256] T. Nagase, S. Anada, P. D. Rack, J. H. Noh, H. Yasuda, H. Mori, T. Egami, *Intermetallics* **2012**, *26*, 122.

[257] M. H. Tsai, J. W. Yeh, J. Y. Gan, *Thin Solid Films* **2008**, *516*, 5527.

[258] L. Gao, J. Song, Z. Jiao, W. Liao, J. Luan, J. U. Surjadi, J. Li, H. Zhang, D. Sun, C. T. Liu, Y. Lu, *Adv. Eng. Mater.* **2018**, *20*, 1700625.

[259] Y. Zhang, T. Zuo, Y. Cheng, P. K. Liaw, *Sci. Rep.* **2013**, *3*, 1455.

[260] S. Chen, X. Chen, L. Wang, J. Liang, C. Liu, *J. Laser Appl.* **2017**, *29*, 012004.

[261] M. H. Chuang, M. H. Tsai, W. R. Wang, S. J. Lin, J. W. Yeh, *Acta Mater.* **2011**, *59*, 6308.

[262] N. A. P. K. Kumar, C. Li, K. J. Leonard, H. Bei, S. J. Zinkle, *Acta Mater.* **2016**, *113*, 230.

[263] T. Yang, S. Xia, W. Guo, R. Hu, J. D. Poplawsky, G. Sha, Y. Fang, Z. Yan, C. Wang, C. Li, Y. Zhang, S. J. Zinkle, Y. Wang, *Scr. Mater.* **2018**, *144*, 31.

[264] S. Q. Xia, M. C. Gao, T. F. Yang, P. K. Liaw, Y. Zhang, *J. Nucl. Mater.* **2016**, *480*, 100.

[265] C. M. Lin, H. L. Tsai, *Intermetallics* **2011**, *19*, 288.

[266] Y. Zhong, L. E. Rännar, S. Wikman, A. Koptyug, L. Liu, D. Cui, Z. J. Shen, *Fusion Eng. Des.* **2017**, *116*, 24.

[267] C. Xiang, E. Han, Z. Zhang, H. Fu, J. Wang, H. Zhang, G. Hu, *Intermetallics* **2019**, *104*, 143.

[268] A. Kareer, J. C. Waite, B. Li, A. Couet, D. E. J. Armstrong, A. J. Wilkinson, *J. Nucl. Mater.* **2019**, *526*, 151744.

[269] S. Shafeie, S. Guo, Q. Hu, H. Fahlquist, P. Erhart, A. Palmqvist, *J. Appl. Phys.* **2015**, *118*, 184905.

[270] Z. Fan, H. Wang, Y. Wu, X. Liu, Z. Lu, *RSC Adv.* **2016**, *6*, 52164.

[271] Z. Fan, H. Wang, Y. Wu, X. Liu, Z. Lu, *Mater. Res. Lett.* **2017**, *5*, 187.

[272] S. T. Chen, W. Y. Tang, Y. F. Kuo, S. Y. Chen, C. H. Tsau, T. T. Shun, J. W. Yeh, *Mater. Sci. Eng. A* **2010**, *527*, 5818.

[273] R. Mahshid, H. N. Hansen, K. L. Højbjerre, *Mater. Des.* **2016**, *104*, 276.

[274] M. Todai, T. Nagase, T. Hori, A. Matsugaki, A. Sekita, T. Nakano, *Scr. Mater.* **2017**, *129*, 65.

[275] T. Nagase, Y. Iijima, A. Matsugaki, K. Ameyama, T. Nakano, *Mater. Sci. Eng. C* **2020**, *107*, 110322.

[276] A. Motallebzadeh, N. S. Peighambardoust, S. Sheikh, H. Murakami, S. Guo, D. Canadinc, *Intermetallics* **2019**, *113*, 106572.

[277] O. Maulik, D. Kumar, S. Kumar, S. K. Dewangan, V. Kumar, *Mater. Res. Express* **2018**, *5*, 052001.

[278] C. H. Chen, Y. J. Chen, *Scr. Mater.* **2019**, *162*, 185.

[279] A. Inoue, A. Takeuchi, *Acta Mater.* **2011**, *59*, 2243.

[280] Z. Lv, X. Liu, B. Jia, H. Wang, Y. Wu, Z. Lu, *Sci. Rep.* **2016**, *6*, 34213.

[281] C. Yang, C. Zhang, L. Liu, *J. Mater. Chem. A* **2018**, *6*, 20992.

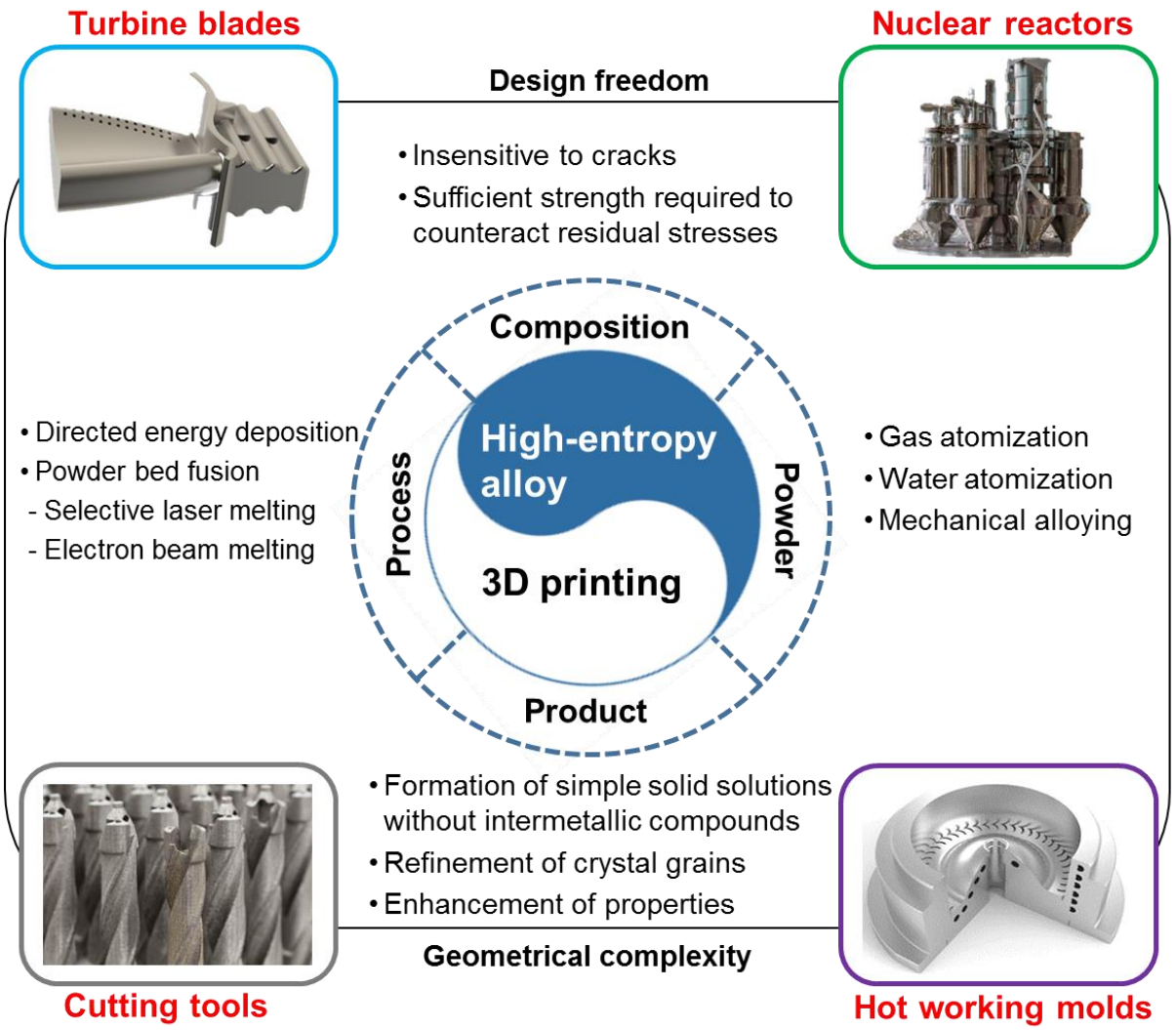

Figure 1. Overview of the relationship between HEAs and 3D printing, with regard to the composition design, powder development, printing processes, product characteristics and potential applications.

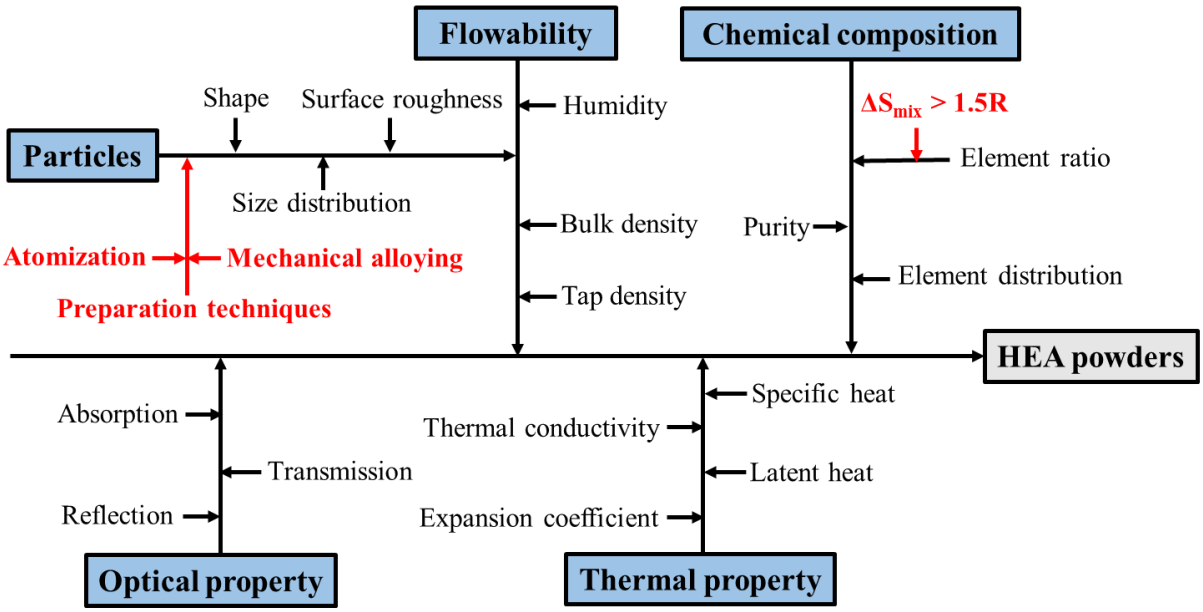

Figure 2. Requirement diagram of HEA powders for DED and PBF printing processes, where ΔS_{mix} denotes the mixing entropy and R the gas constant.

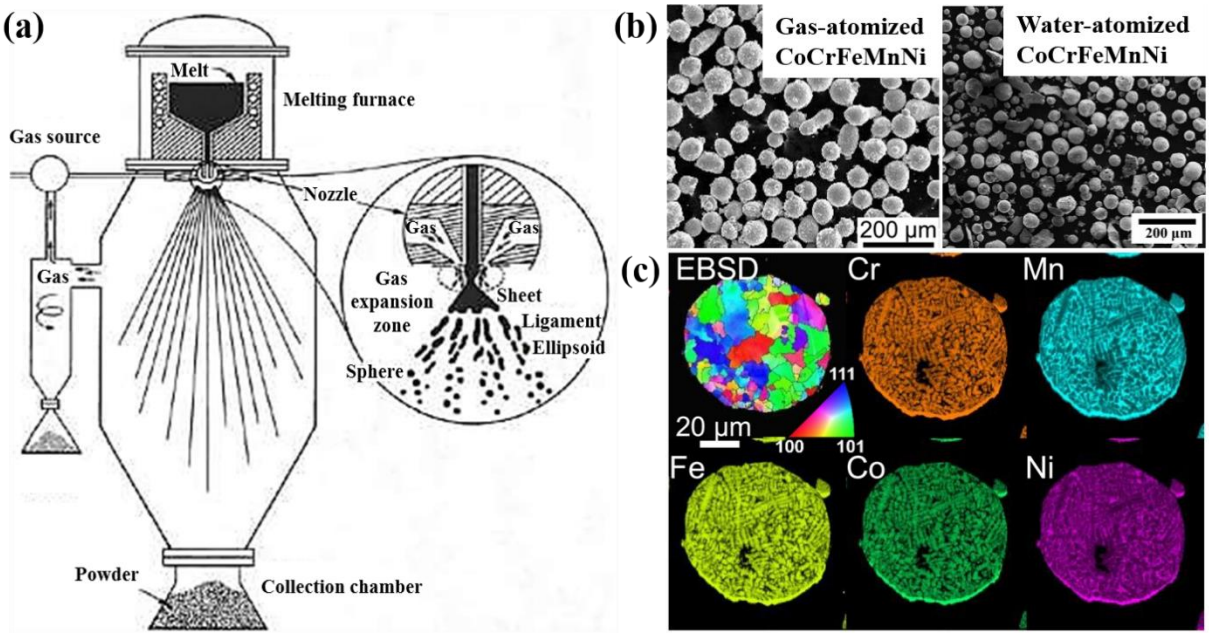

Figure 3. (a) Illustration of a typical experimental setup for gas atomization and its schematic mechanism of atomization stages, (b) morphologies of gas-atomized and water-atomized CoCrFeMnNi HEA powders,[74, 75] and (c) electron backscatter diffraction (EBSD) image and elemental distribution of a powder particle.[75] Reproduced with permission.[74] Copyright 2018, Elsevier. Reproduced with permission.[75] Copyright 2019, Elsevier.

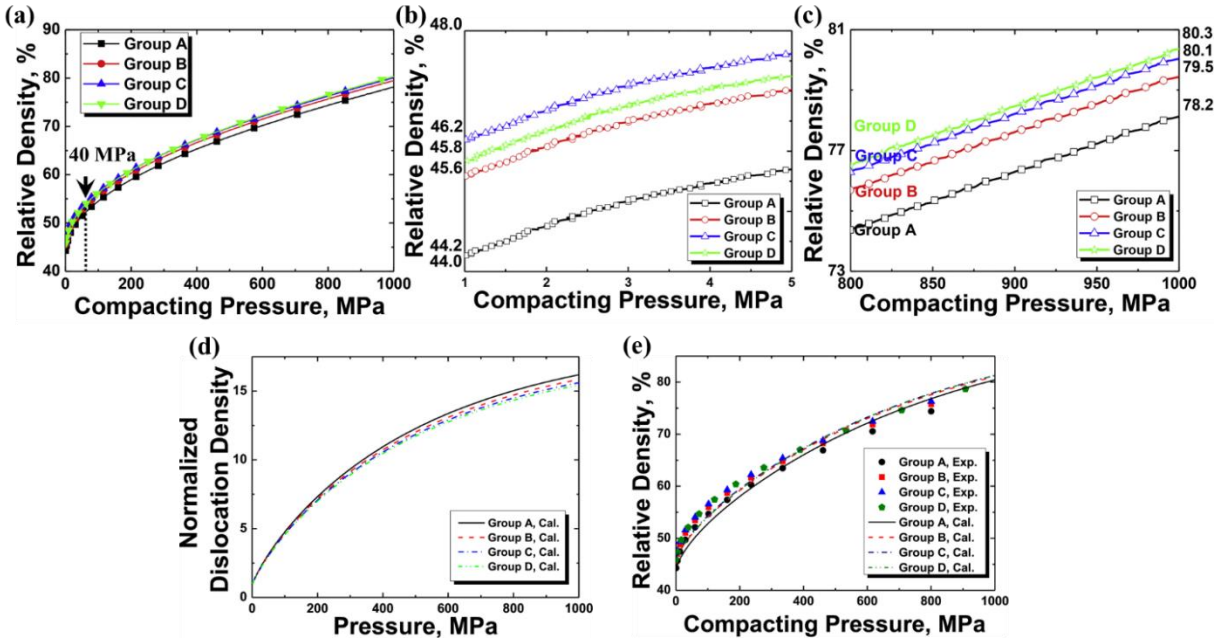

Figure 4. Compacting behaviors of a water-atomized CoCrFeMnNi HEA powder with various particle sizes: (a) compaction curves, (b) tap density, (c) relative density under higher pressure, (d) theoretical and experimental compaction curves, and (e) the calculated dislocation density. Group A, B, C and D represent the particle sizes of 0–45, 45–75, 75–105 and 105–150 μm, respectively.[74] Reproduced with permission.[74] Copyright 2018, Elsevier.

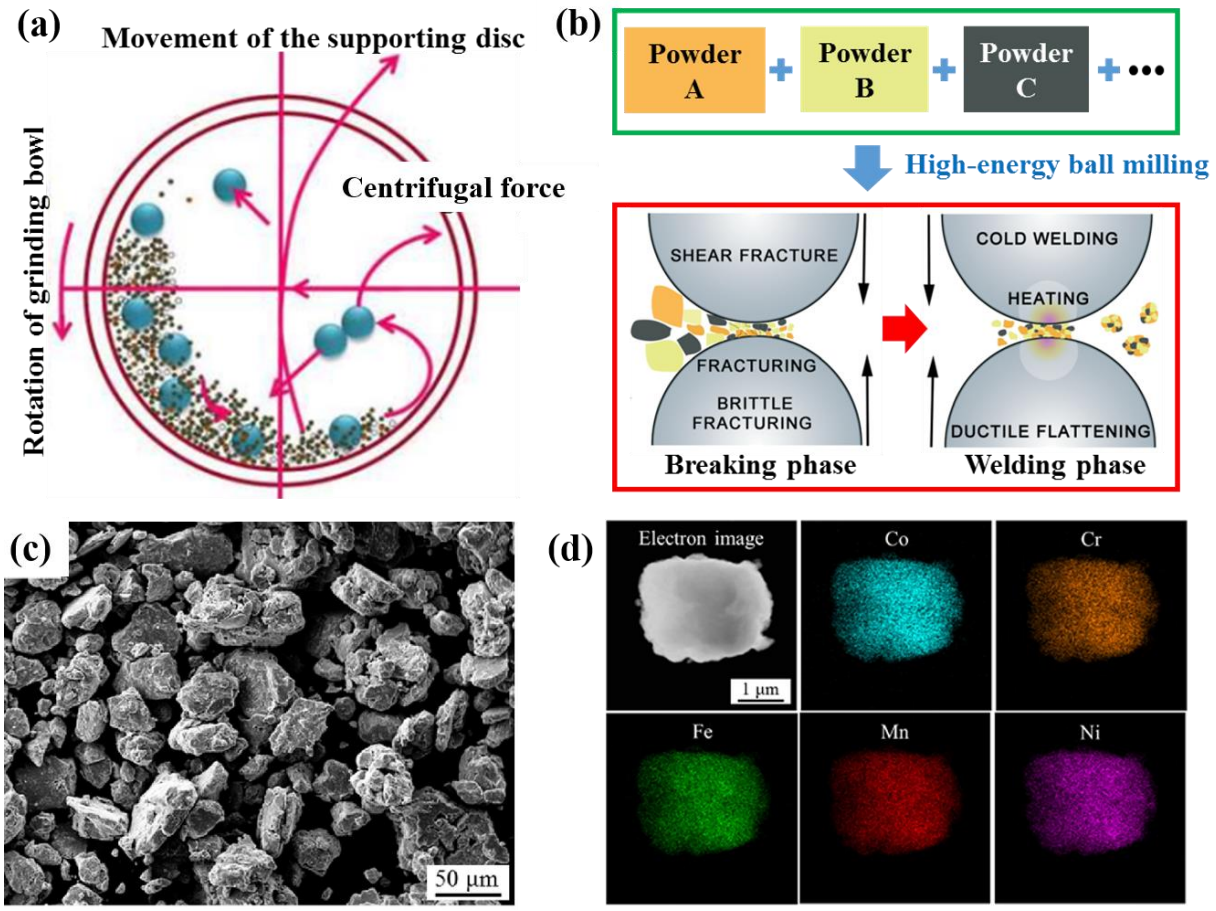

Figure 5. (a) Illustration of the mechanical alloying process, (b) schematic mechanism of mechanical alloying including breaking and welding phases, (c) morphology of a CoCrFeMnNi HEA powder produced by mechanical alloying, and (d) element distributions in a powder particle.[111] Reproduced with permission.[111] Copyright 2017, Elsevier.

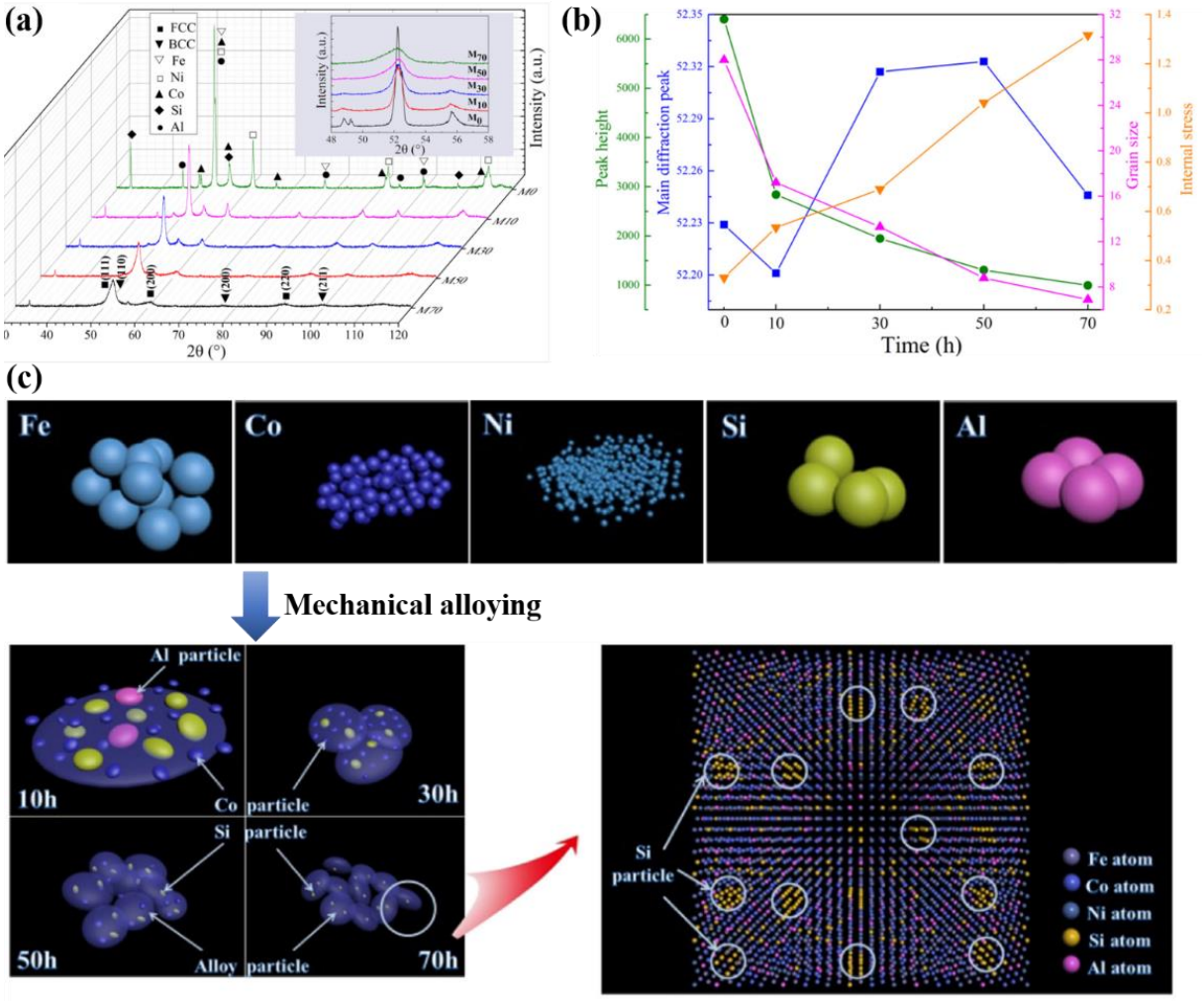

Figure 6. The $Al_{0.4}CoFeNiSi_{0.4}$ HEA powder developed by mechanical alloying with different milling times: (a) X-ray diffraction (XRD) patterns with the enlarged picture from 48° to 58° in the inset, (b) peak height, main diffraction peak angle position, grain size (nm) and internal stress (%) obtained from XRD, and (c) flow schematic illustration for the formation of powders. M0, M10, M30, M50 and M70 represent the milling times of 0, 10, 30, 50 and 70 h, respectively.[108] Reproduced with permission.[108] Copyright 2018, Elsevier.

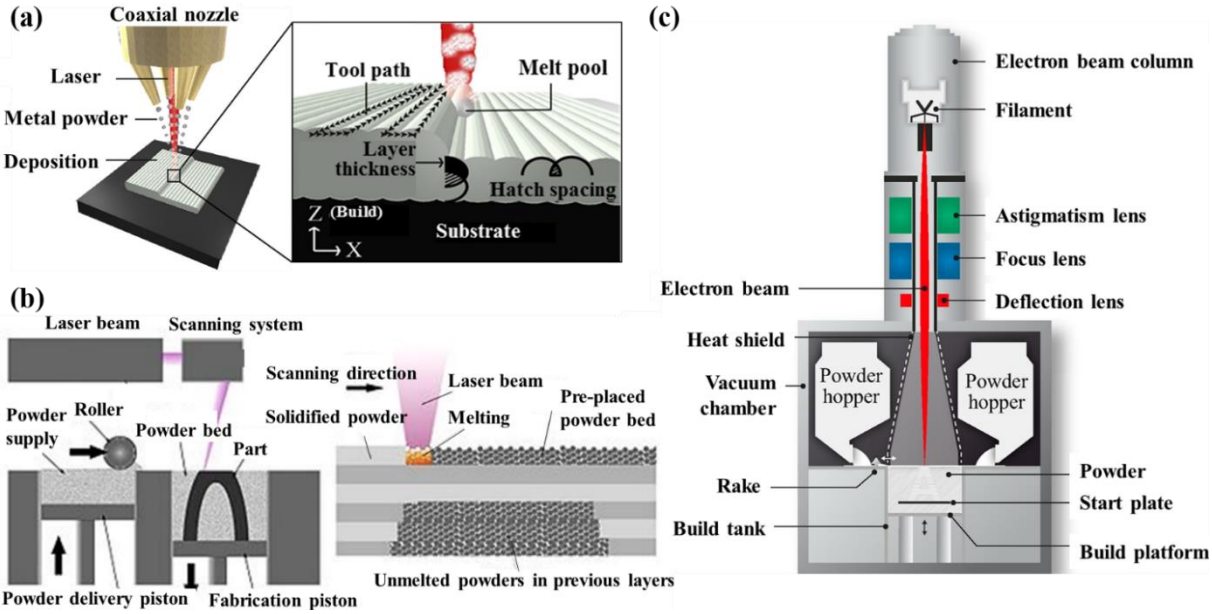

Figure 7. Schematic diagrams of major 3D printing processes for HEAs: (a) DED,[144] (b) SLM,[145] and (c) EBM.[146] Reproduced with permission.[144] Copyright 2017, Elsevier. Reproduced with permission.[145] Copyright 2019, Public Library of Science. Reproduced with permission.[146] Copyright 2018, Elsevier.

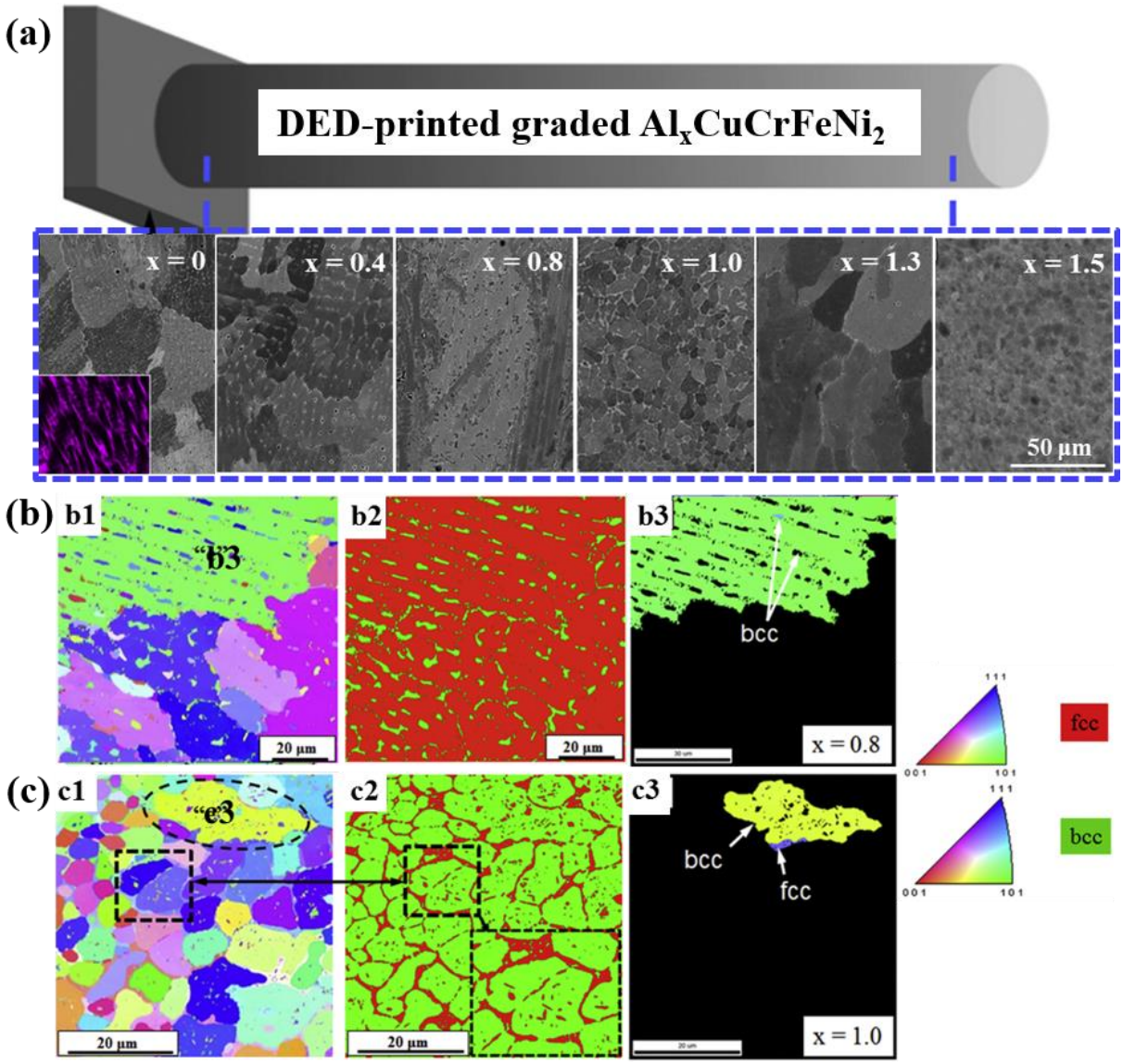

Figure 8. Microstructure of compositionally graded $Al_xCuCrFeNi_2$ HEA products printed by DED: (a) morphologies, (b) EBSD results from $Al_{0.8}CuCrFeNi_2$, (b1) various orientations and the inverse pole figure map, (b2) phase map demarking FCC and BCC regions, (b3) inverse pole figure map of a selected grain in (b1), (c) EBSD results from $AlCuCrFeNi_2$, (c1) various orientations and the inverse pole figure map, (c2) phase map demarking FCC and BCC regions, and (c3) inverse pole figure map of a selected grain in (c1).[163] Reproduced with permission.[163] Copyright 2016, Elsevier.

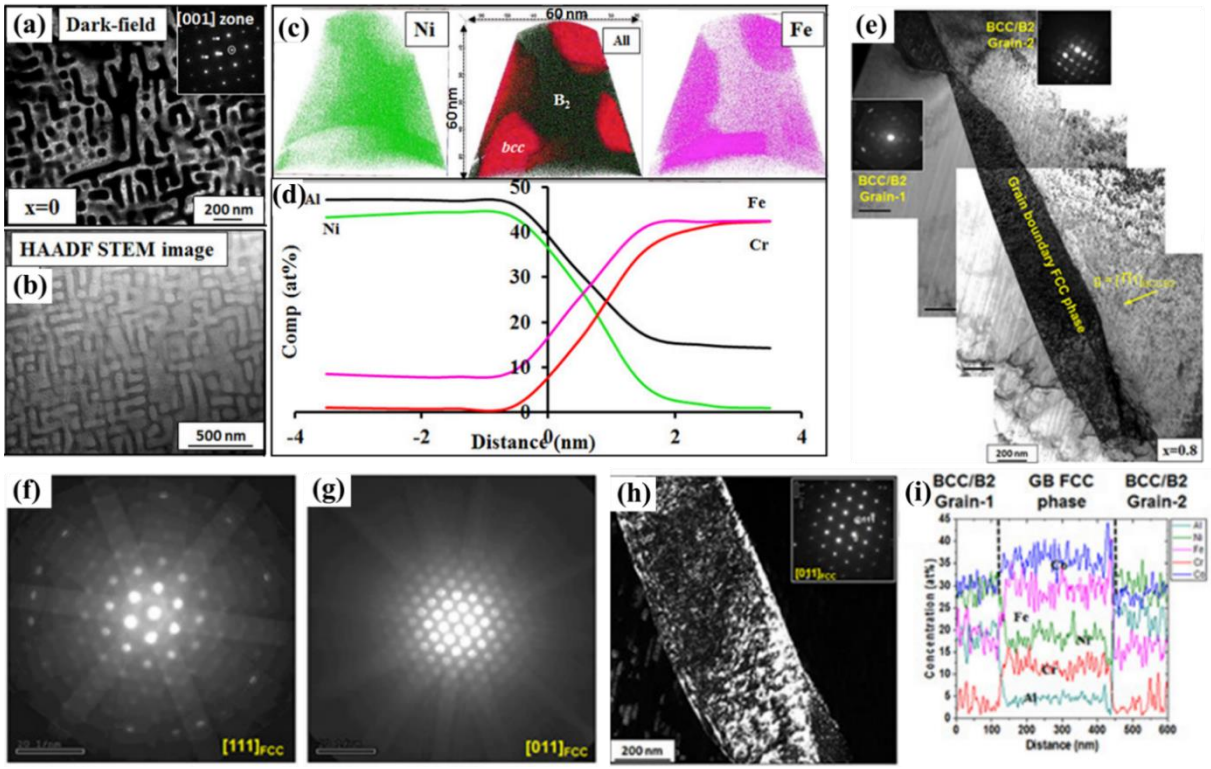

Figure 9 Phase identification in DED-printed graded $AlCo_xCr_{1-x}FeNi$ HEA products: (a) dark-field image from superlattice B2 reflection in a [001] zone axis (x = 0), (b) TEM image, (c) 3D reconstructions of atoms from atom probe tomography measurements, (d) composition profiles across a 12 at% Cr isosurface, (e) grain boundary region (x = 0.8), (f) its dark field image from the grain boundary precipitate, (g) and (h) SAD patterns from [111]FCC and [110]FCC zone axis of the precipitate, respectively, and (i) composition profiles recorded across the precipitate.[152] Reproduced with permission.[152] Copyright 2017, Wiley-VCH.

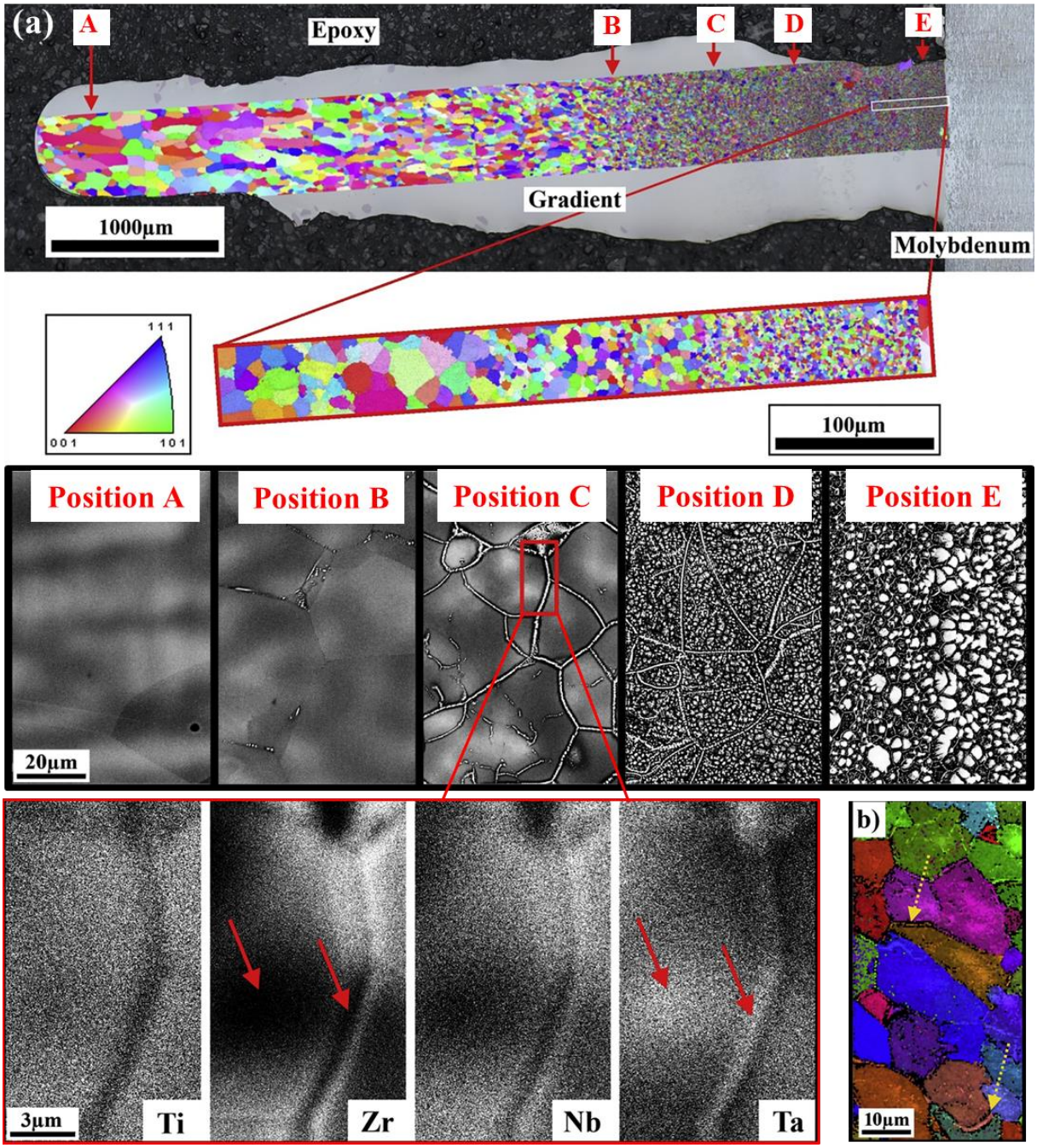

Figure 10. Microstructure of a graded $Ti_{25}Zr_{50-x}Nb_xTa_{25}$ HEA developed by DED: (a) color-coded grain orientation map from EBSD and enlarged backscattered electron images in different positions, and (b) color-coded grain orientation map obtained by EBSD showing both the matrix and the secondary phase at the grain boundaries. From position A to E, *x* varied from 0 to 50. [149] Reproduced with permission.[149] Copyright 2019, Elsevier.

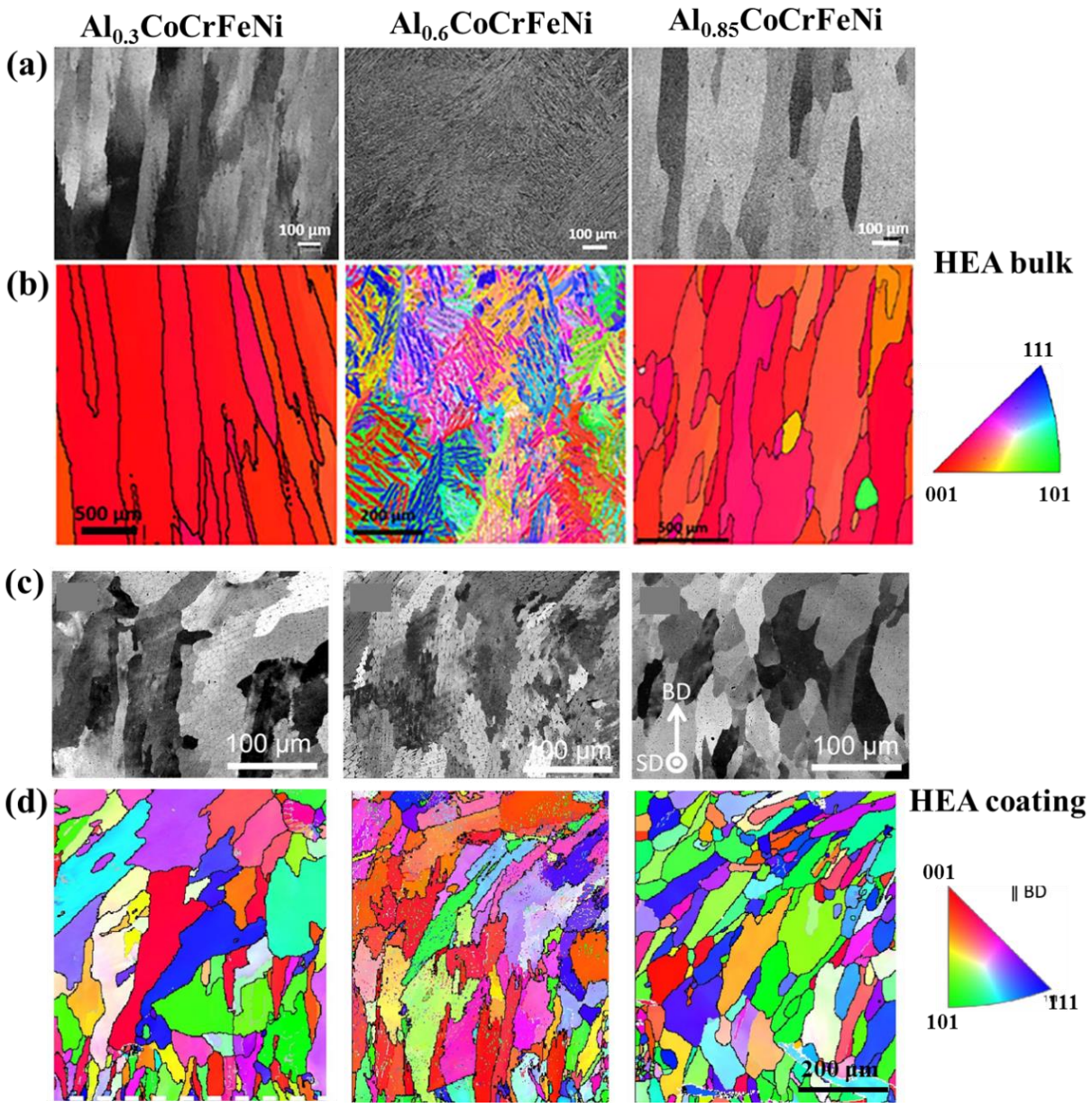

Figure 11. Comparison of the microstructures of DED-printed $Al_xCoCrFeNi$ HEA bulk products and coatings parallel to the build direction: (a) scanning electron microscope (SEM) images showing surface morphologies and (b) corrresponding inverse pole figure map of the products through EBSD,[153] (c) SEM morphology and (d) inverse pole figure map of the deposited coating.[154] Reproduced with permission.[153] Copyright 2015, Elsevier. Reproduced with permission.[154] Copyright 2017, Elsevier.

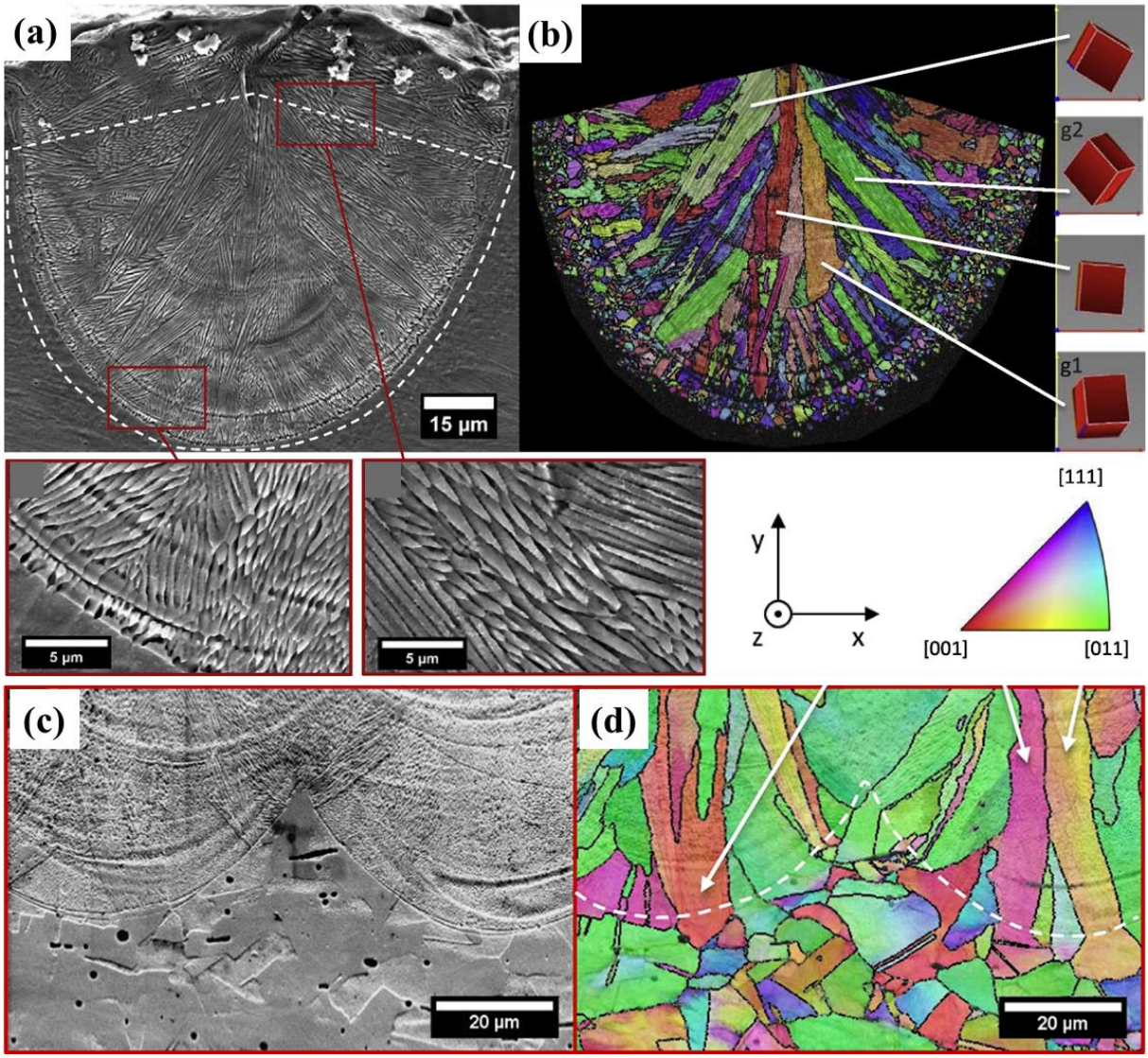

Figure 12. (a) Microstructure and (b) inverse pole figure map of the cross section of one track in the single-layer build produced by SLM from a CoCrFeMnNi HEA powder through EBSD measurement; the cubes showed the crystallographic orientations of selected grains, (c) microstructure and (d) inverse pole figure map of the cross-section in the multi-layer build.[188] Reproduced with permission.[188] Copyright 2018, Elsevier.

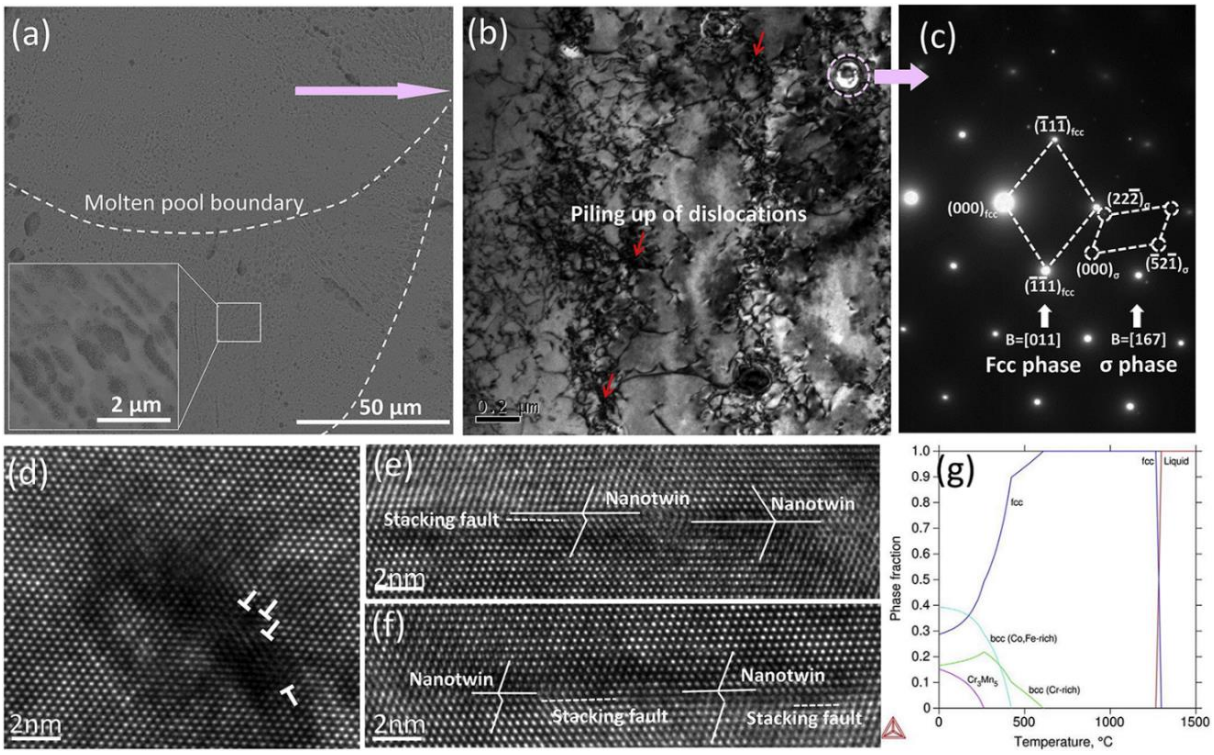

Figure 13. Microstructure of SLM-printed CoCrFeMnNi HEA products: (a) SEM image showing the melt pool boundary and sub-micro cellular grains, (b) TEM bright field showing high density of dislocation piled up and dislocation network, (c) selected area diffraction pattern showing FCC phase and σ precipitate phase, high-resolution transmission electron microscopy images showing (d) dislocations and (e, f) nano-twins coupled with stacking faults, and (g) calculated equilibrium phase fractions.[90] Reproduced with permission.[90] Copyright 2018, Elsevier.

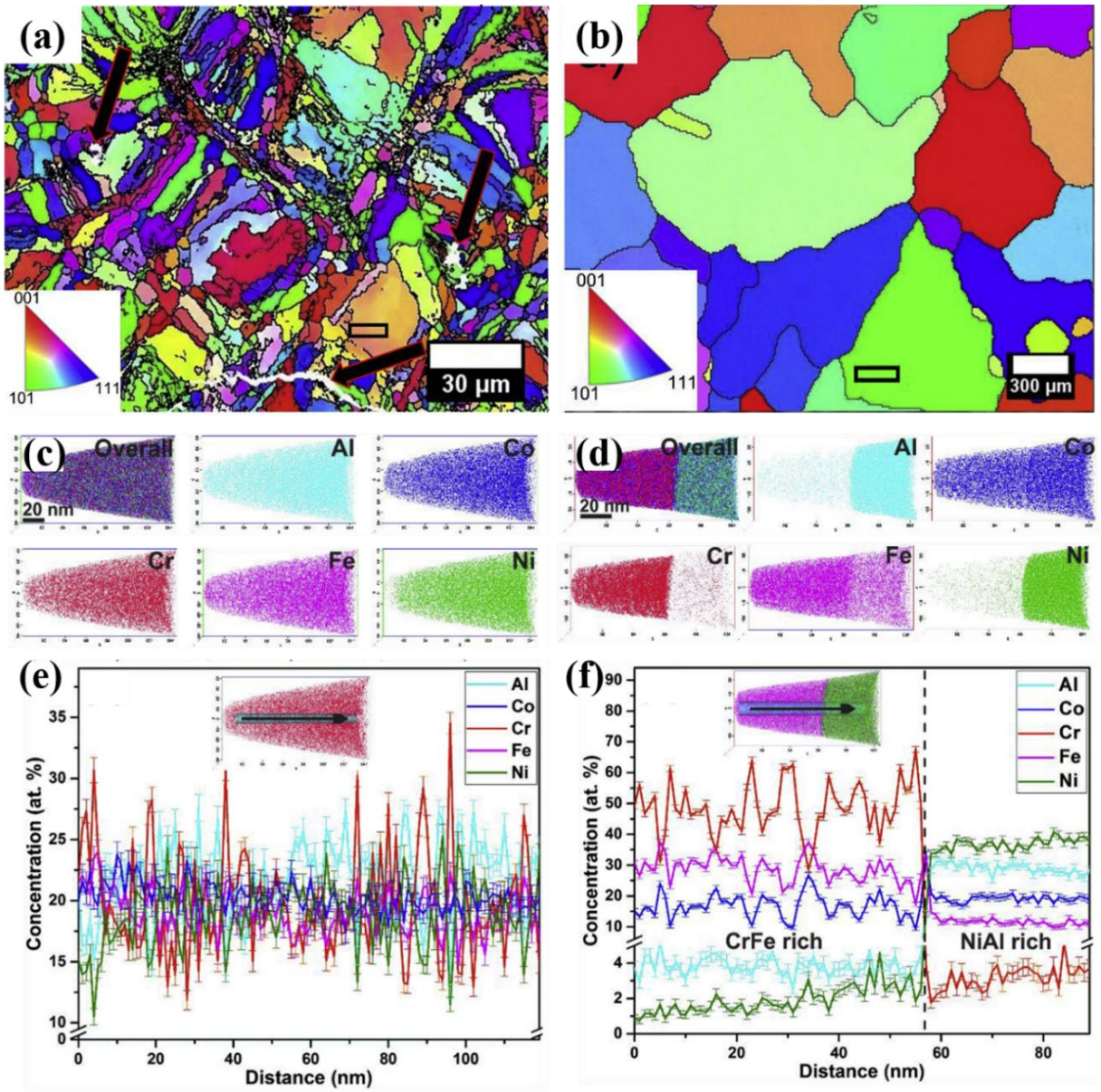

Figure 14. Comparison of microstructure between the SLM-printed AlCoCrFeNi HEA product and the casted counterpart: EBSD images of (a) SLM-printed product and (b) casted counterpart; atom probe tomography analysis showing three-dimensional distribution of Al, Co, Cr, Fe and Ni atoms of (c) SLM-printed product and (d) casted counterpart, one-dimensional concentration profile of elements taken along the cylinder of (e) SLM-printed product and (f) casted counterpart.[195] Reproduced with permission.[195] Copyright 2019, Elsevier.

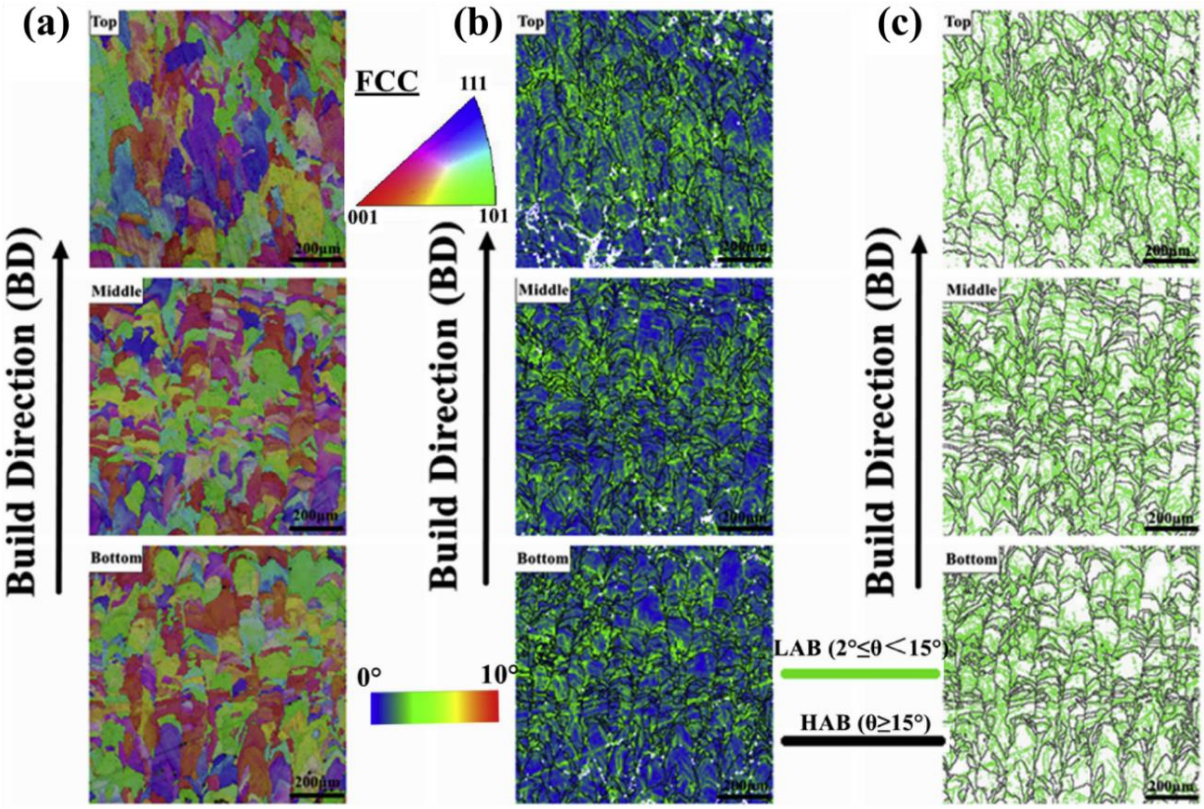

Figure 15. EBSD analyses in different regions of SLM-printed $FeCoCrNiC_{0.05}$ HEA products: (a) inverse pole figure, (b) local misorientation maps, and (c) grain boundary maps.[93] Reproduced with permission.[93] Copyright 2018, Elsevier.

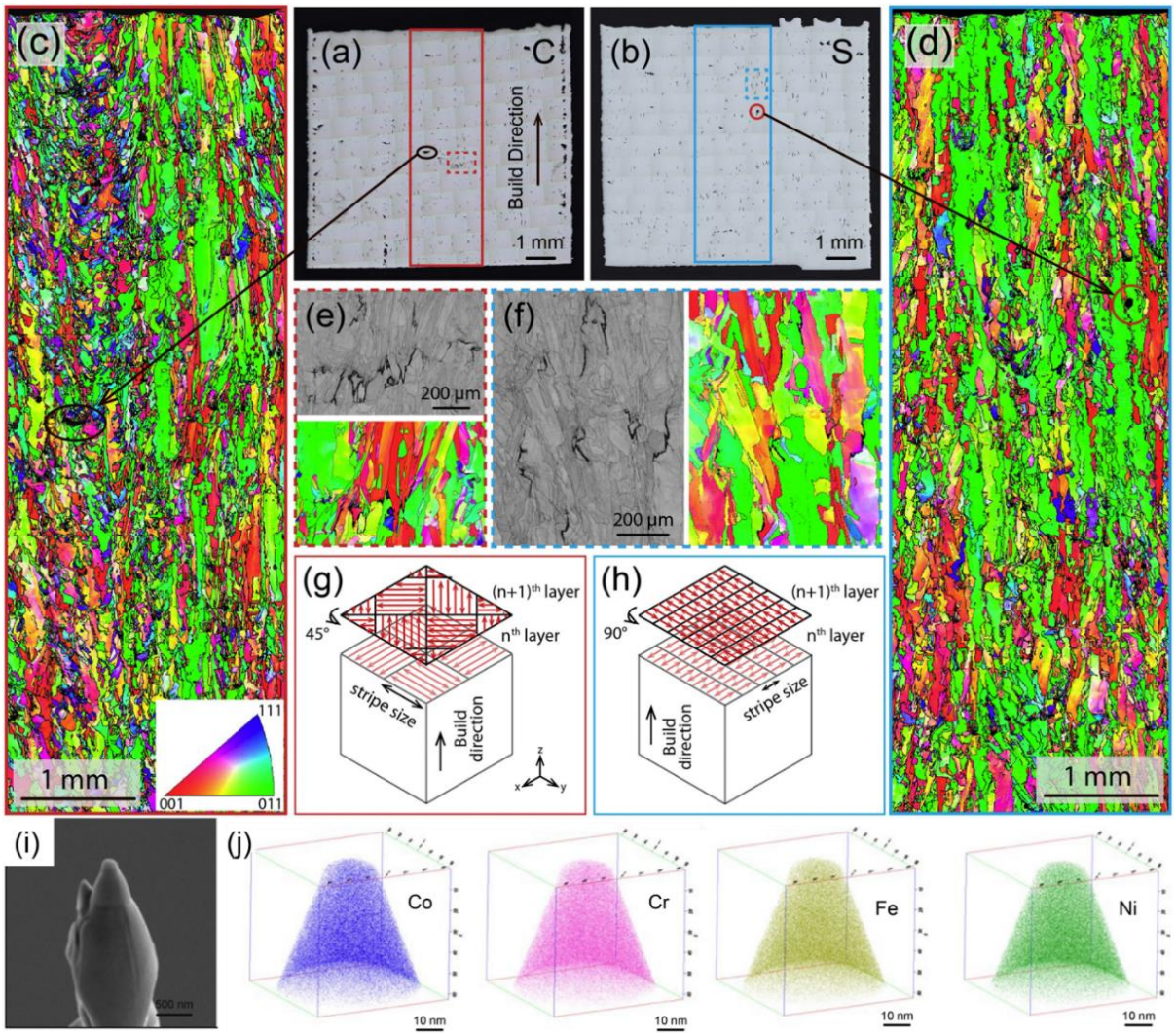

Figure 16. Optical microscope images of SLM-printed CoCrFeNi HEA products with (a) chessboard (denoted as C) and (b) stripe (denoted as S) scanning strategies; EBSD inverse pole figure maps with respect to the build direction of the selected areas for (c) C product and (d) S product; Enlarged EBSD band contrast images and inverse pole figure maps showing intergranular cracks within (e) C product and (f) S product; schematic illustrations of scanning strategy of SLM: (g) chessboard and (h) stripe; (i) SEM image showing a tip of atom probe tomography specimen with a dimension of 50 nm, and (j) atom distribution of the constituting elements.[200] Reproduced with permission.[200] Copyright 2019, Elsevier.

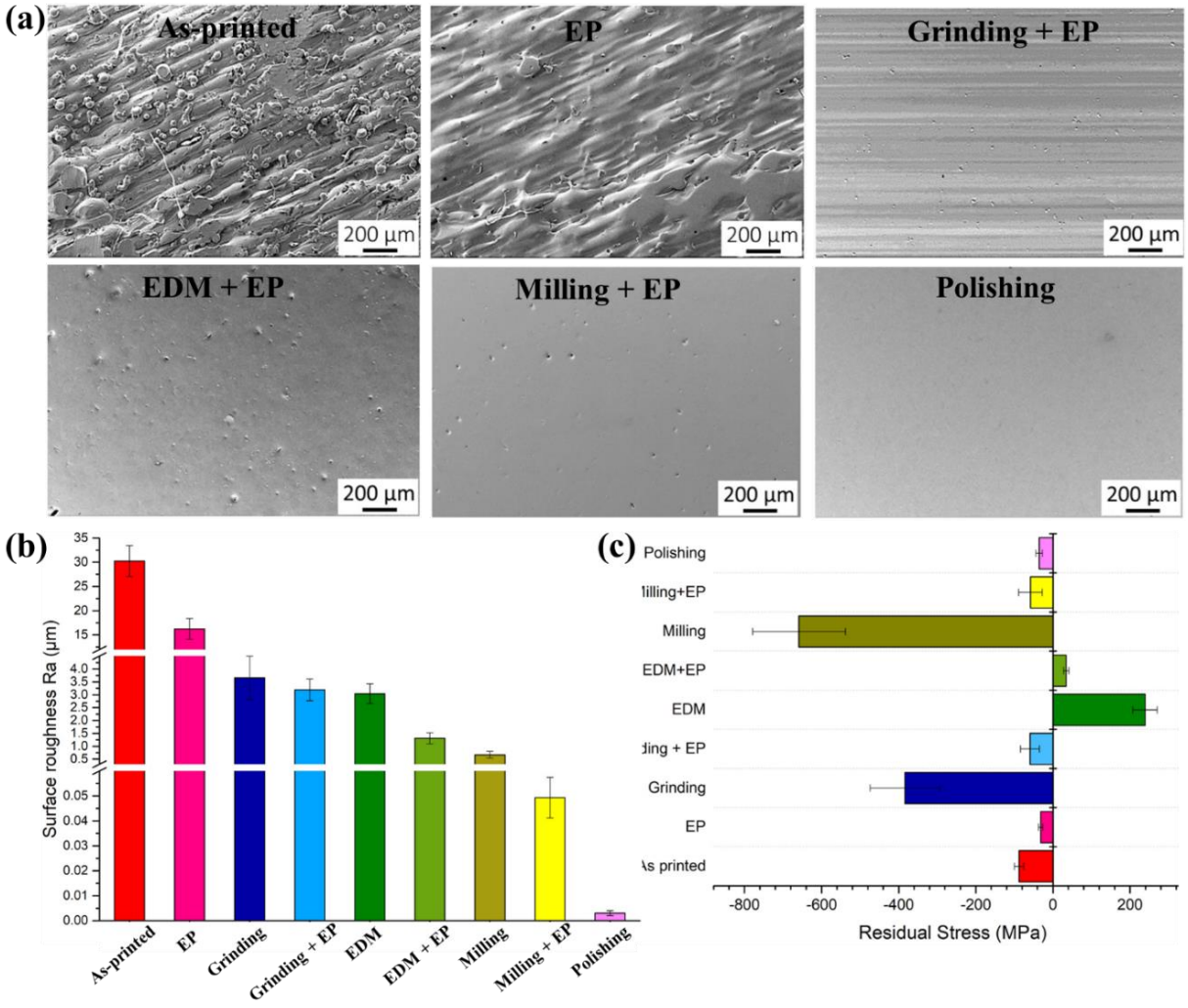

Figure 17. Surface characteristics of SLM-printed CoCrFeMnNi HEA products with different machining processes: (a) secondary electron images of typical surface morphologies, (b) surface roughness, and (c) residual stresses.[209] Reproduced with permission.[209] Copyright 2018, Elsevier.

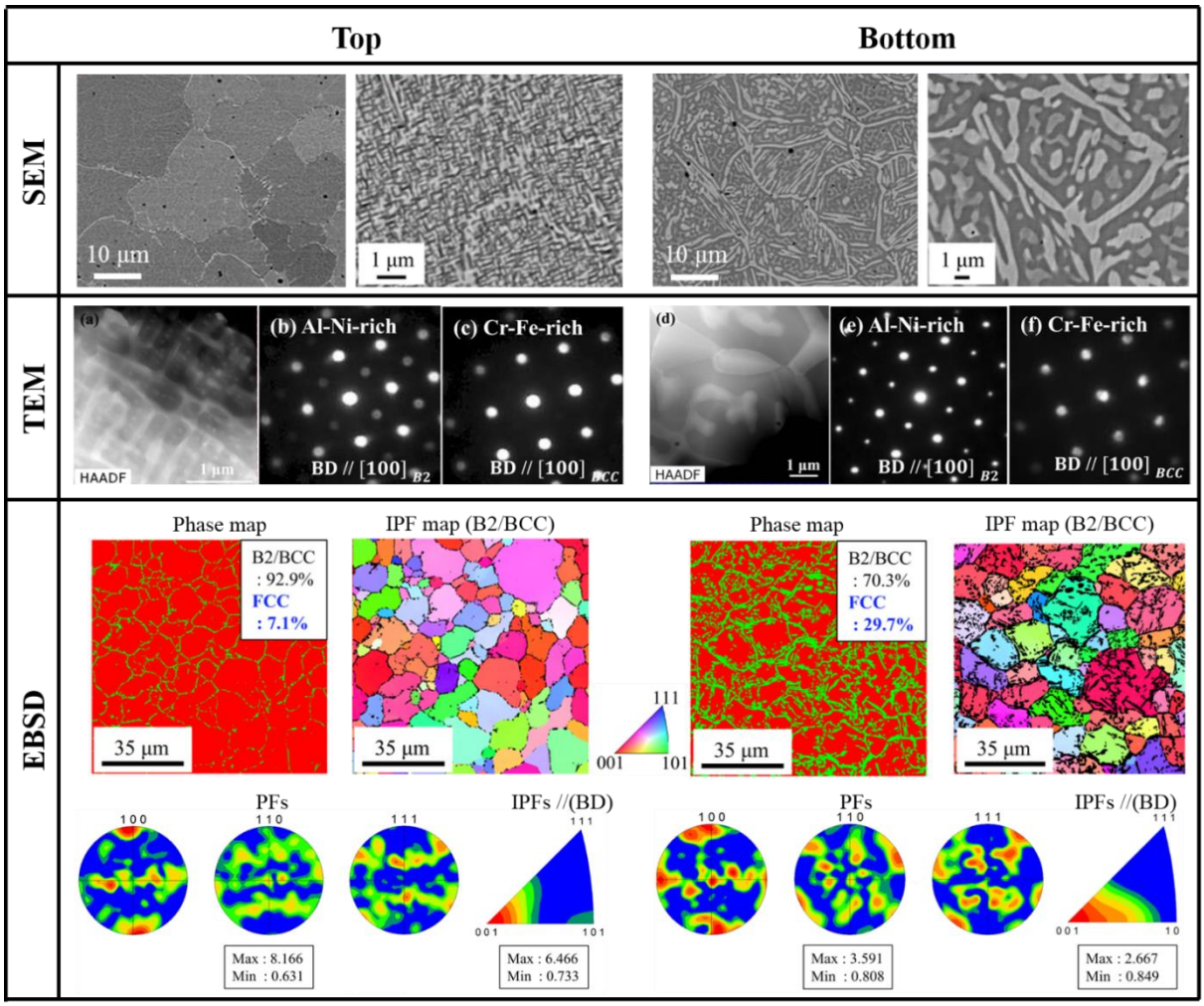

Figure 18. Phase and microstructural characteristics of EBM-printed AlCoCrFeNi HEA products at top and bottom regions from TEM, SEM and EBSD measurements.[83] Reproduced with permission.[83] Copyright 2016, Elsevier.

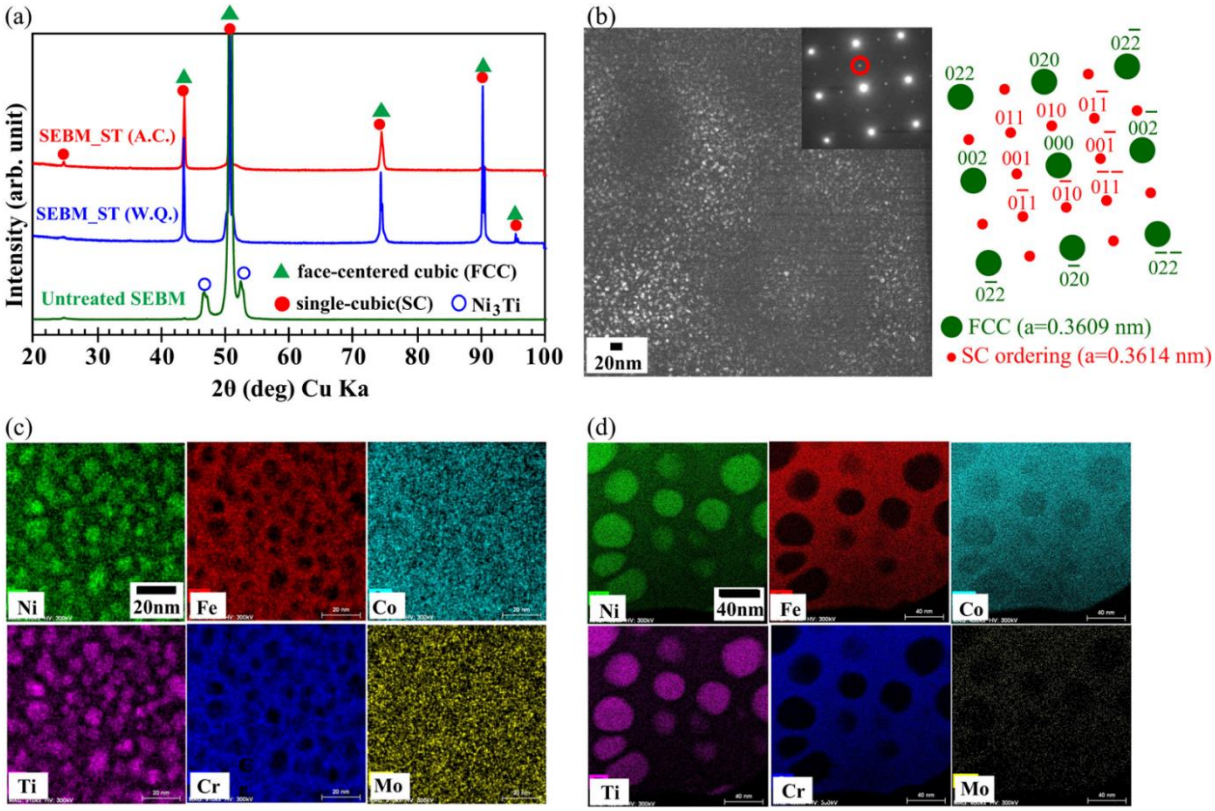

Figure 19. Effects of the solution treatments on the phases of EBM-printed $Co_{1.5}CrFeNi_{1.5}Ti_{0.5}Mo_{0.1}$ HEA products: (a) Phase identification of untreated and solution-treated products, (b) TEM dark field image and corresponding diffraction pattern of EBM products by W.Q., (c) and (d) elemental mappings of EBM products by W.Q. and A.C., respectively.[213] Reproduced with permission.[213] Copyright 2017, Elsevier.

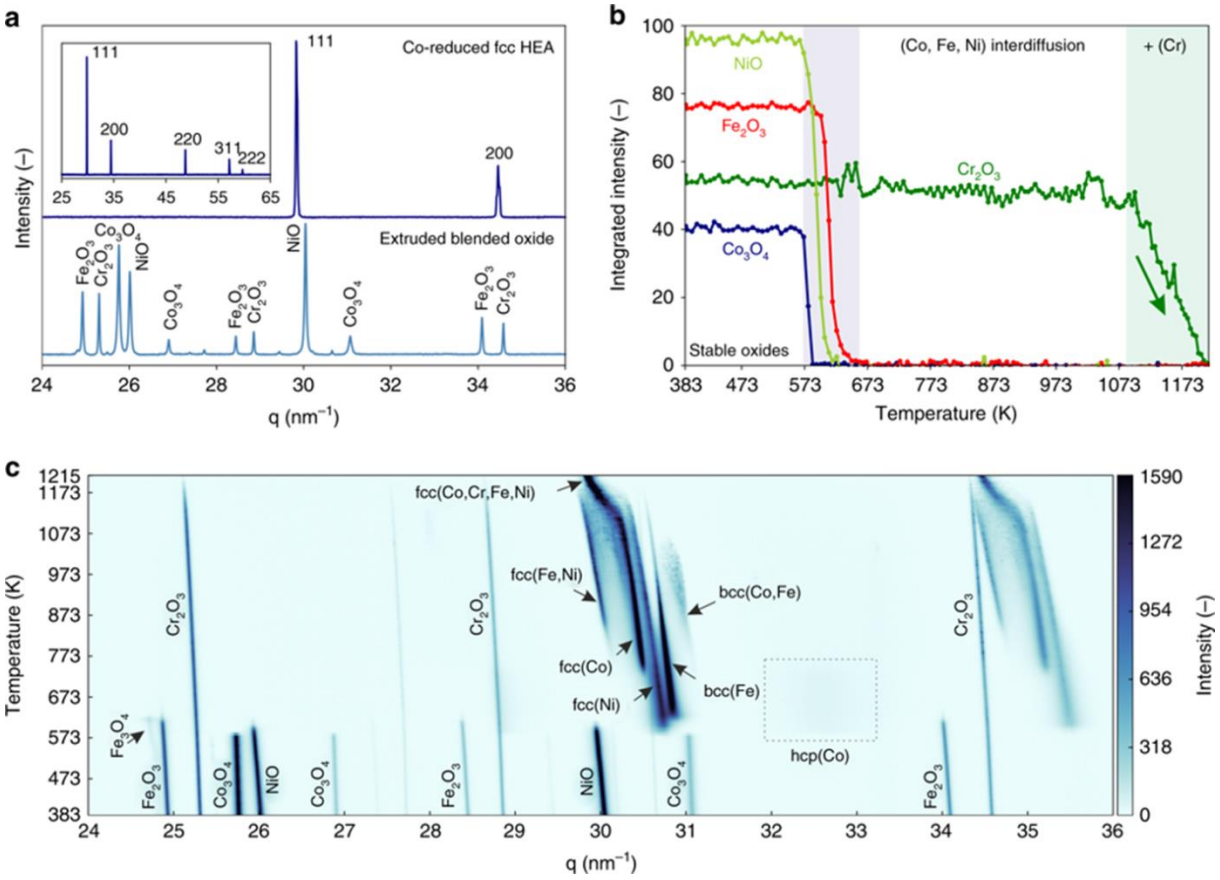

Figure 20. Phase evolution upon co-reduction of 3D-extruded blended oxides by *in situ* synchrotron X-ray diffraction in H_2: (a) X-ray diffraction diffractograms, (b) evolution of the integrated peak intensities for Co_3O_4, Cr_2O_3, Fe_2O_3 and NiO, demonstrating sequential reduction forming Co, Ni, Fe between 573 K and 637 K, followed by reduction of Cr_2O_3 between 1073 K and 1215 K, and (c) 2D phase evolution plot (temperature vs. the scattering vector *q*, with diffraction peak intensity as color map) upon heating and reduction, illustrating the complex pathway to form the CoCrFeNi HEA.[217] Reproduced with permission.[217] Copyright 2019, Nature Research.

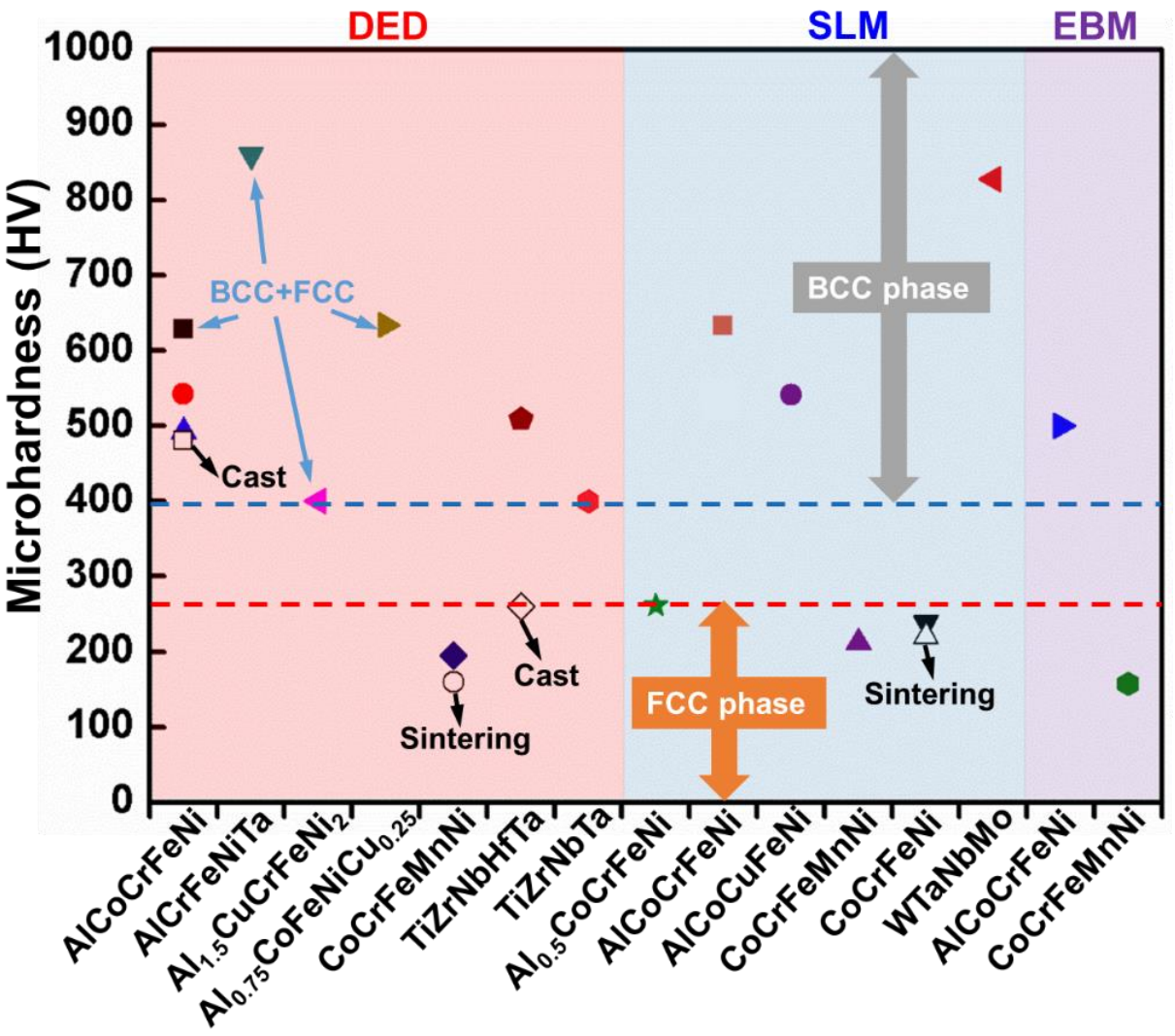

Figure 21. Microhardness of 3D-printed HEA products.[75, 80, 83, 85, 149, 151, 157, 163, 164, 168, 172, 187, 188, 193, 196, 207, 208] Typical HEA counterparts prepared by conventional manufacturing processes are contrastive.[88, 226, 227]

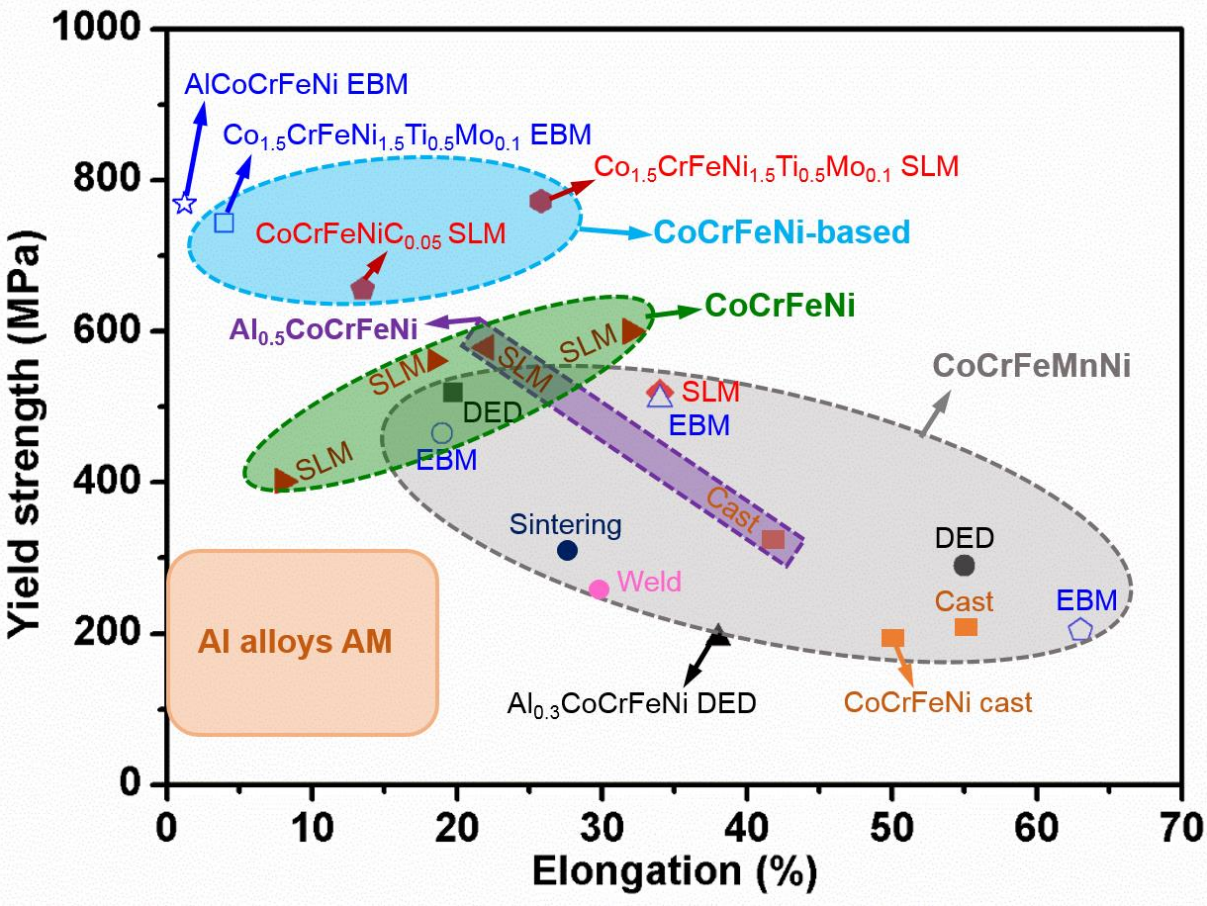

Figure 22. Summary of tensile yield strength versus elongation for 3D-printed HEA products.

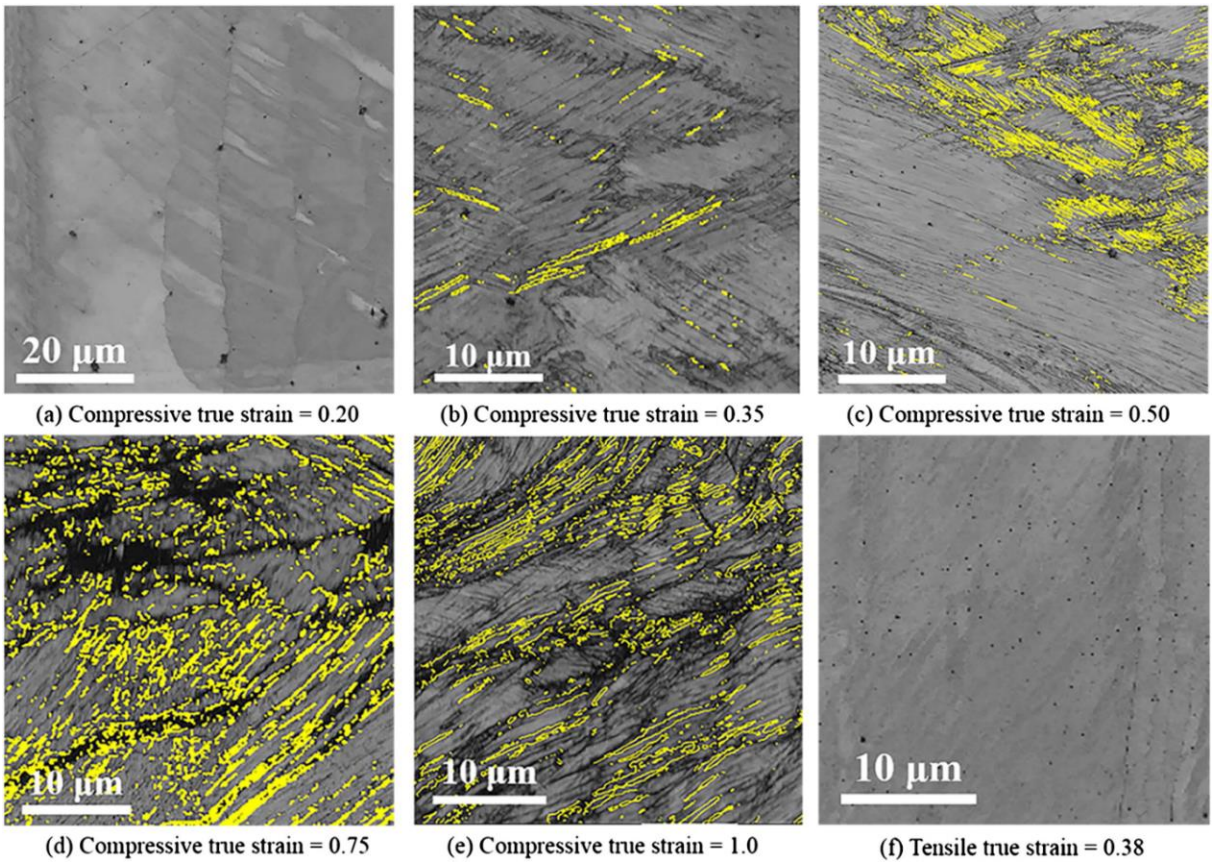

Figure 23. EBSD map of the DED-printed $Al_{0.3}$CoCrFeNi HEA products deformed to various strain levels in compression and tension. Boundaries within 5° of the twin orientation have been highlighted in yellow.[171] Reproduced with permission.[171] Copyright 2017, Elsevier.

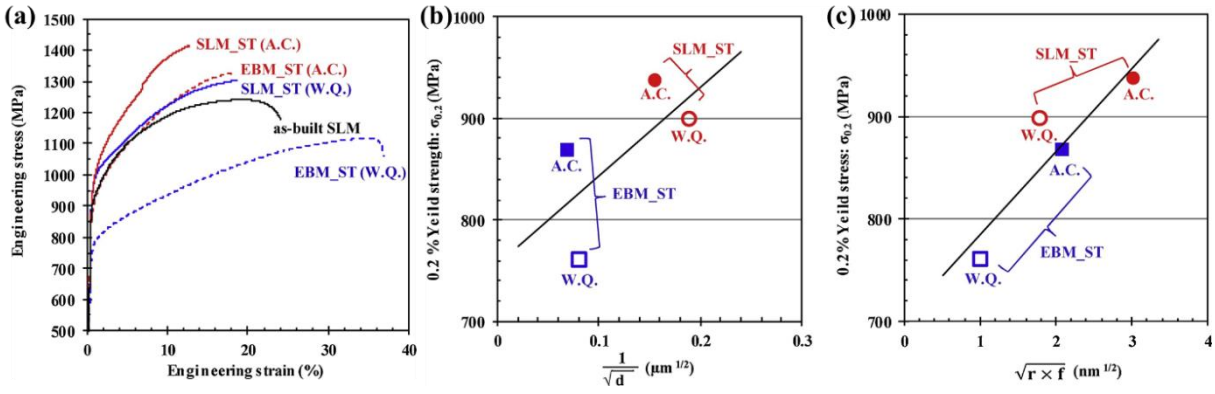

Figure 24 The comparison of mechanical properties of $Co_{1.5}CrFeNi_{1.5}Ti_{0.5}Mo_{0.1}$ HEAs printed by SLM and EBM with the solution treatments of both water quenching and air cooling: (a) tensile stress-strain curves, (b) relationship between yield strength and grain size (*d*: average grain diameter), and (c) dependence of size and volume fraction of ordered particles on yield strength (*f*: volume fraction of ordered particles, *r*: radius of ordered particles).[203] Reproduced with permission.[203] Copyright 2019, Elsevier.

.

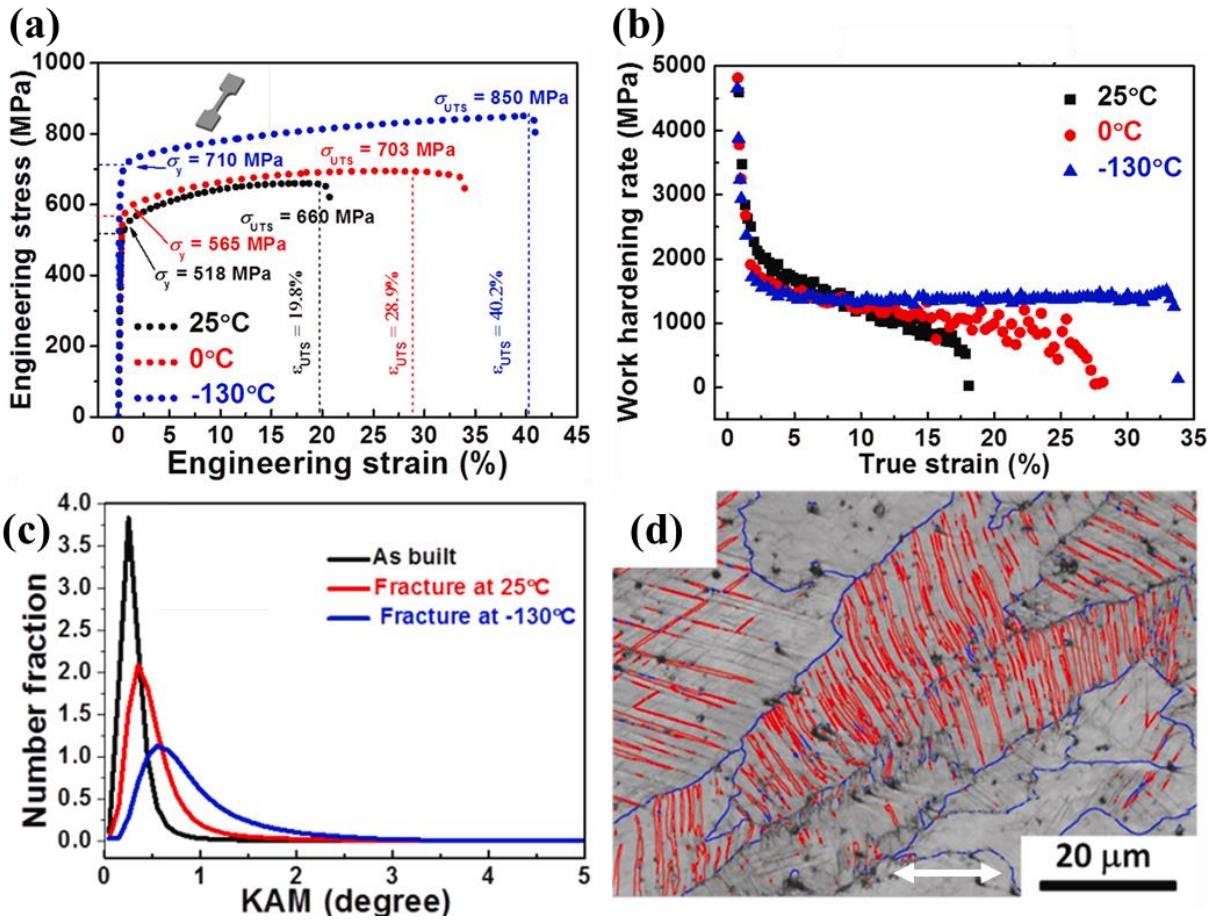

Figure 25. (a) Tensile stress-strain curves of DED-printed CoCrFeMnNi HEA products at 25, 0, and -130 °C, respectively; (b) strain hardening curves deformed at 25, 0, and -130 °C, respectively, (c) kernel average misorientation distributions, and (d) grain boundary map showing the deformation twins at -130 °C. The blue and red lines represented the high angle grain boundaries and deformation twins, respectively. The white arrow indicated the tensile axis.[174] Reproduced with permission.[174] Copyright 2019, Elsevier.

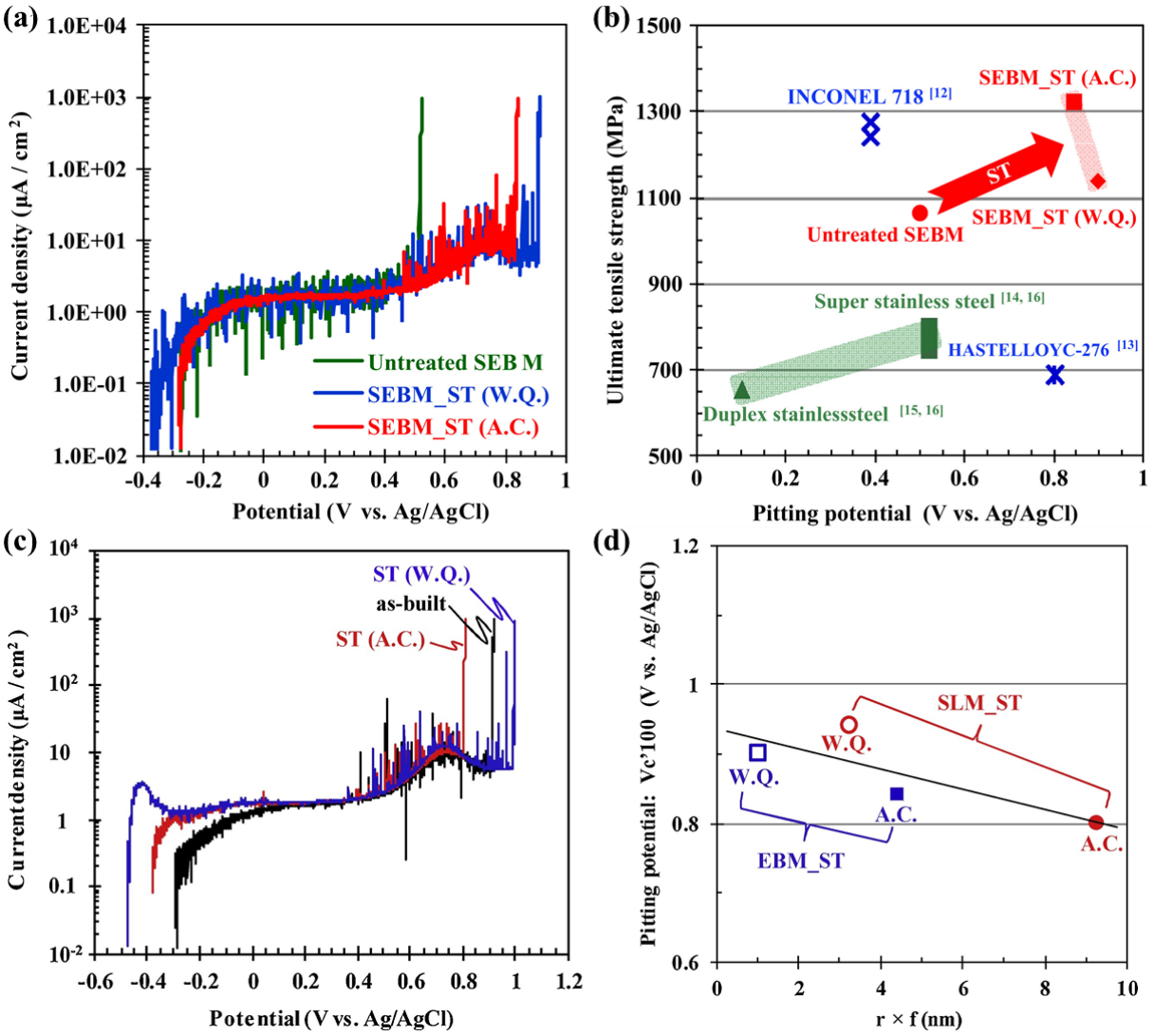

Figure 26. Corrosion properties of $Co_{1.5}CrFeNi_{1.5}Ti_{0.5}Mo_{0.1}$ HEA products printed by EBM and SLM with solution treatments: (a) potentiodynamic polarization curves of EBM-printed HEA products before and after the treatments, (b) comparison of tensile strength and pitting potential between the HEAs and conventional alloys,[213] (c) potentiodynamic polarization curves of SLM-printed HEA products, and (d) dependence of size and volume ratio of ordered particles on pitting potential of solution-treated HEA products (*f*: volume fraction of ordered particles, *r*: radius of ordered particles).[203] Reproduced with permission.[213] Copyright 2017, Elsevier. Reproduced with permission.[203] Copyright 2019, Elsevier.

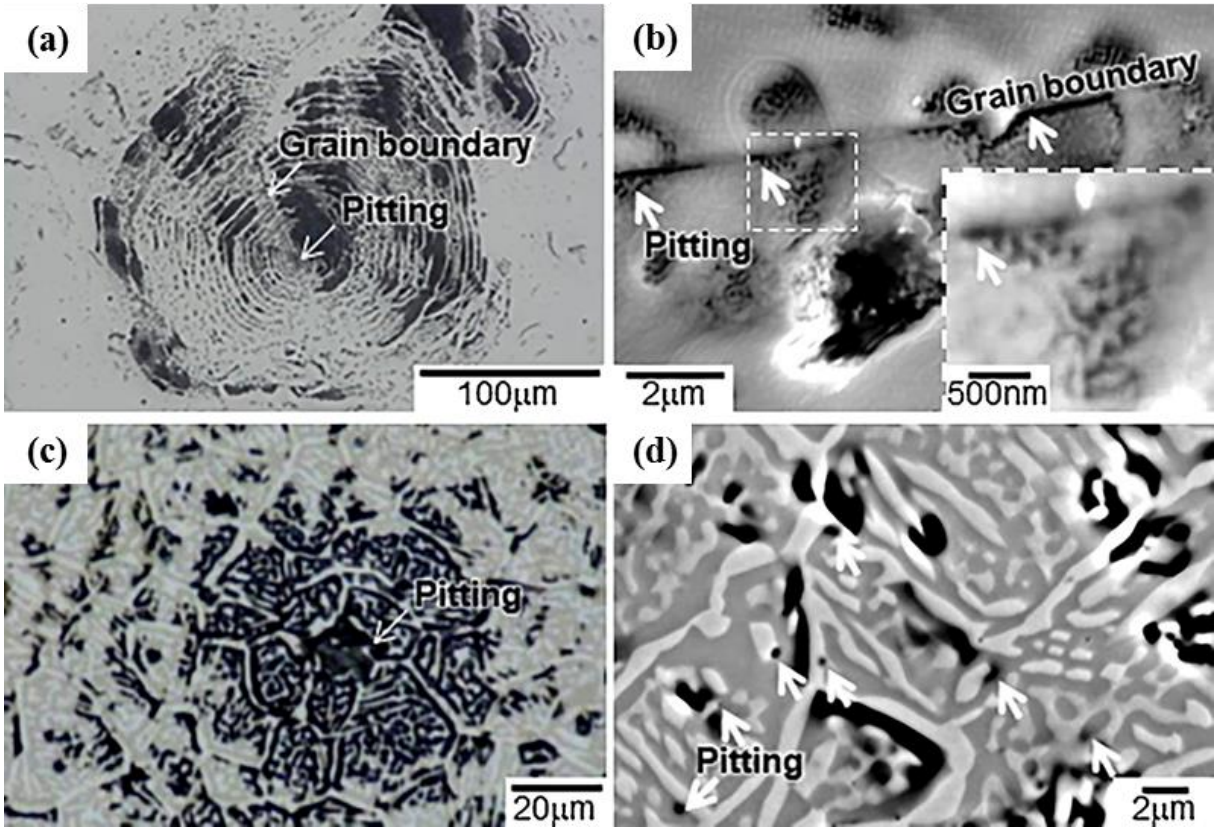

Figure 27. Corrosion morphologies of AlCoCrFeNi HEA products printed by EBM and casting: (a) and (b) casted product, (c) and (d) EBM-printed product.[82] Reproduced with permission.[82] Copyright 2018, Elsevier.

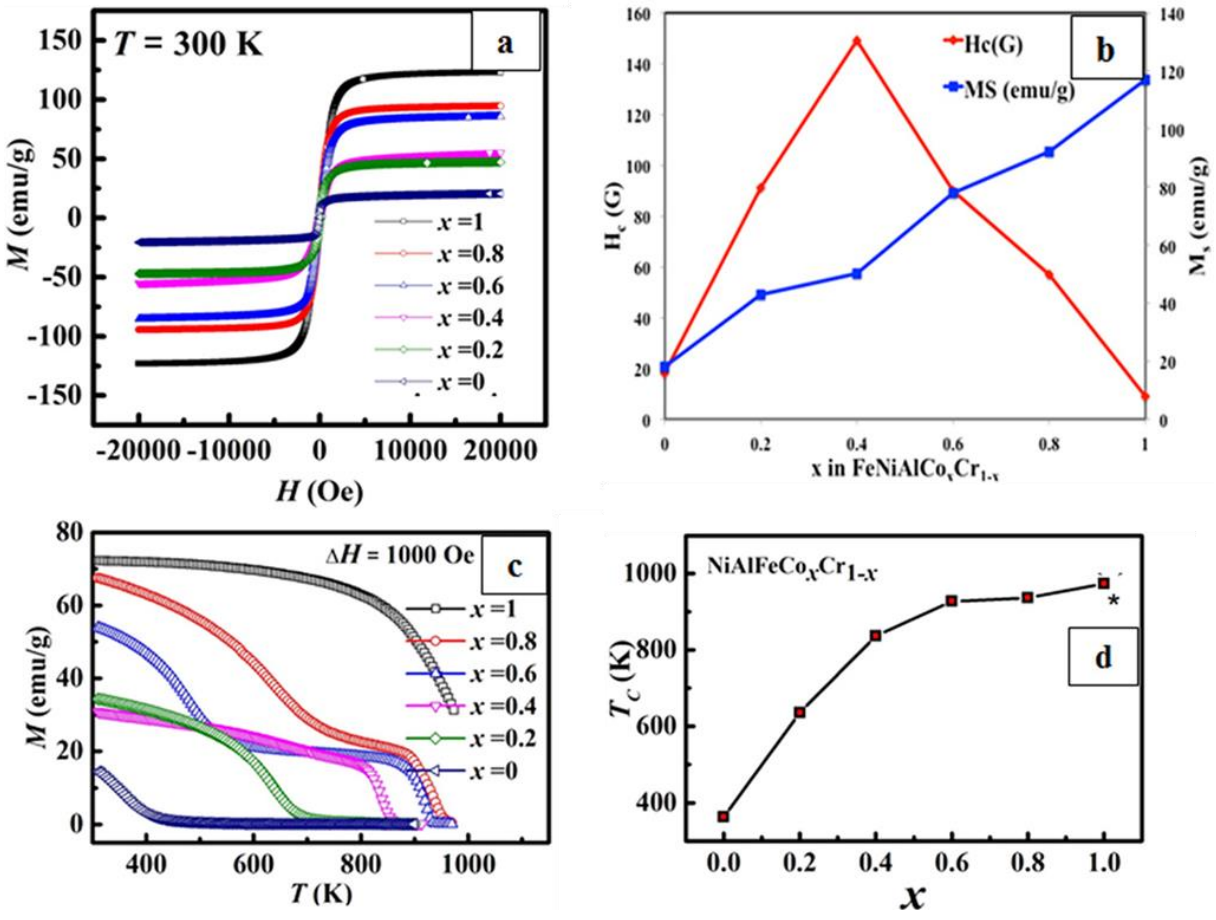

Figure 28. Magnetic properties of DED-printed $AlCo_xCr_{1-x}FeNi$ HEA products: (a) magnetizations M as a function of applied magnetic field H at 300 K, (b) saturation magnetization M_s and coercive force H_c as a function of Co concentration, (c) saturation magnetization as a function of temperature at a magnetic field of 0.1 T at temperatures ranging from room temperature to 973 K, and (d) variation of T_c with the Co concentration.[152] Reproduced with permission.[152] Copyright 2017, Wiley-VCH.

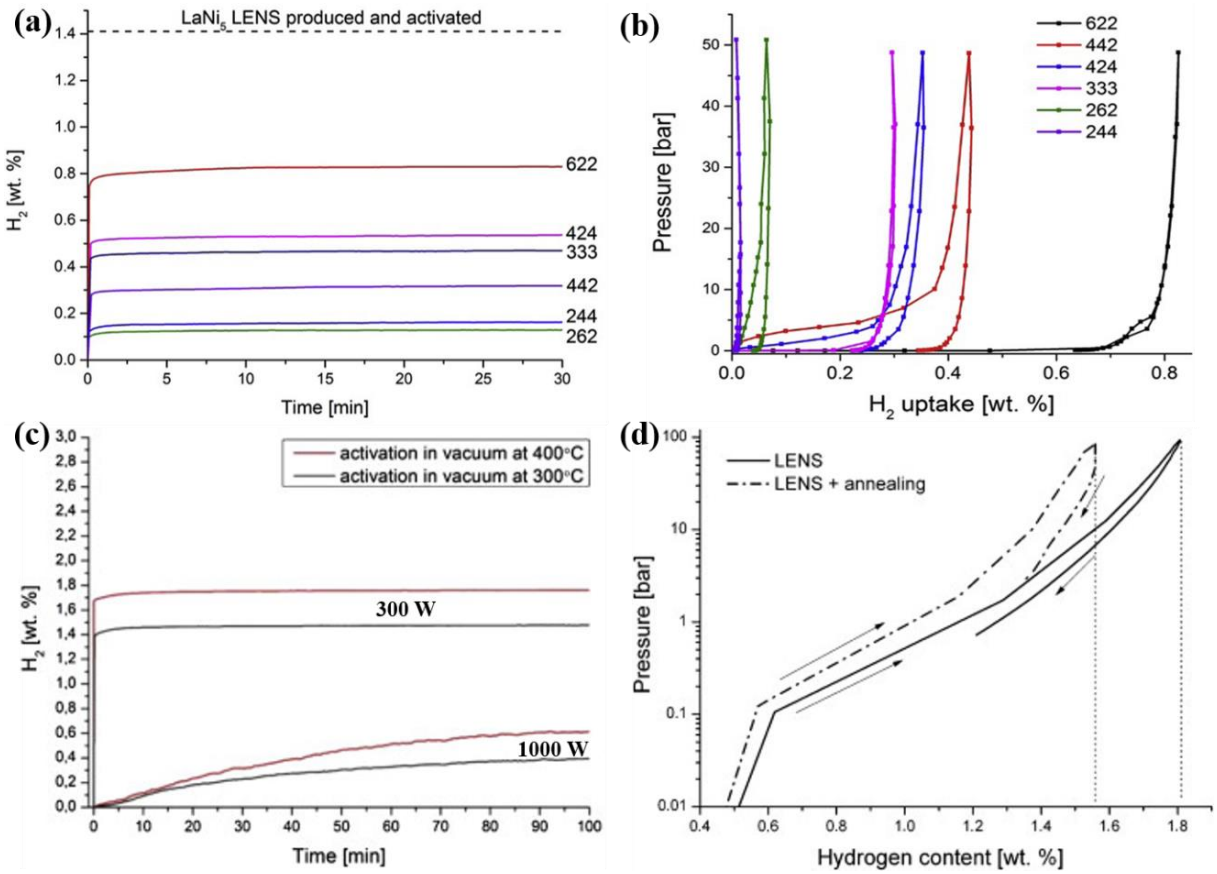

Figure 29. Hydrogen storage properties of DED-printed HEA products: (a) hydrogen absorption kinetics curves of LaNiFeVMn products taken at 35 ℃ after activation, (b) hydrogen absorption and desorption isotherms for the products. Code 622, 442, 424, 333, 262 and 244 represent for $La_{0.1}Ni_{0.5}Fe_{0.1}V_{0.1}Mn_{0.2}$, $La_{0.07}Ni_{0.33}Fe_{0.2}V_{0.2}Mn_{0.2}$, $La_{0.07}Ni_{0.33}Fe_{0.1}V_{0.1}Mn_{0.4}$, $La_{0.06}Ni_{0.28}Fe_{0.16}V_{0.16}Mn_{0.33}$, $La_{0.03}Ni_{0.17}Fe_{0.3}V_{0.3}Mn_{0.2}$ and $La_{0.03}Ni_{0.17}Fe_{0.2}V_{0.2}Mn_{0.4}$, respectively,[161] (c) hydrogen absorption curves of TiZrNbMoV HEA products produced using the laser power of 300 and 1000 W after activation at 300 and 400 °C,[159] and (d) hydrogen absorption and desorption isotherms for ZrTiVCrFeNi HEA products before and after annealing at 1000 °C for 24 h.[160] Reproduced with permission.[161] Copyright 2017, Elsevier. Reproduced with permission.[159] Copyright 2014, Elsevier. Reproduced with permission.[160] Copyright 2013, Elsevier.

.

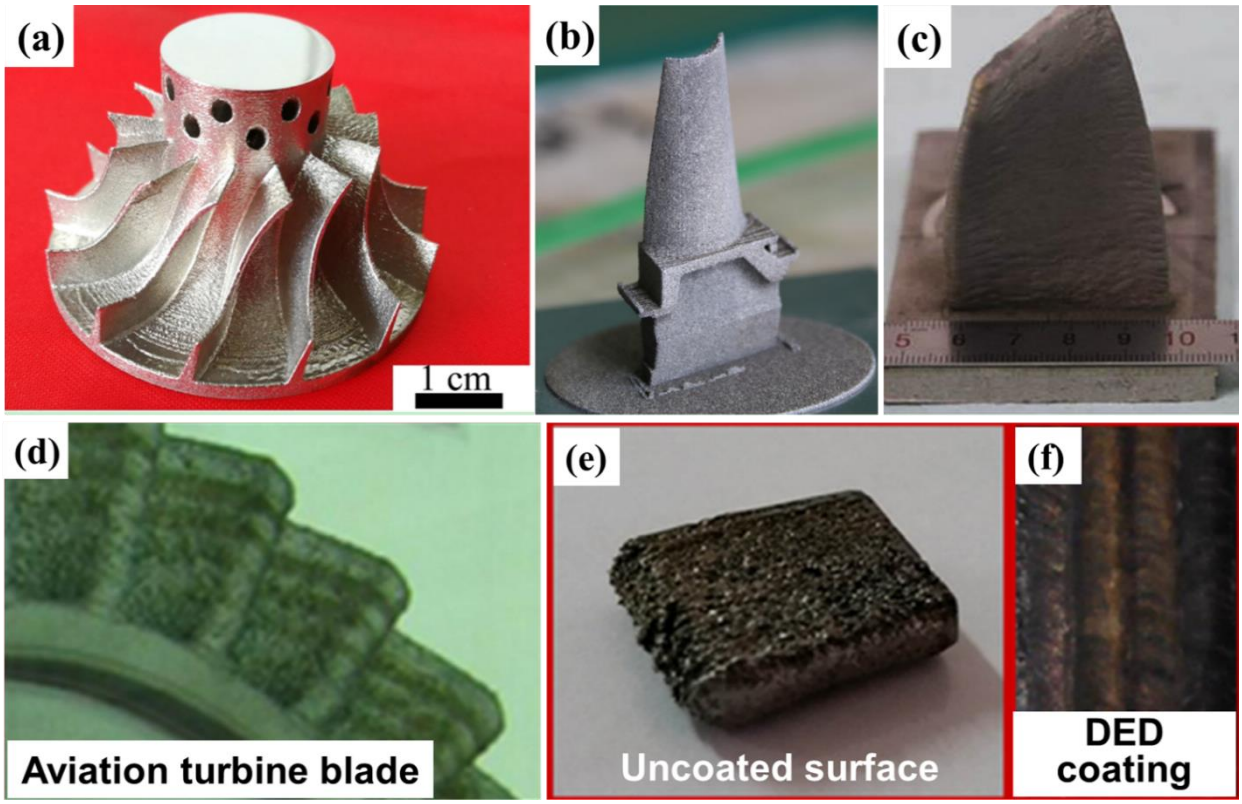

Figure 30. Validation of HEA products by DED and PBF printing processes in the aerospace industry: (a) a SLM-printed $Al_{0.5}$CoCrFeNi turbine blade,[85] (b) a SLM-printed WNbTaMo blade,[208] (c) a DED-printed CoCrFeMnNi vane prototype,[173] (d) a DED-printed titanium aviation turbine blade, (e) uncoated surface of the blade, and (f) modified surface with HEA coating by DED.[155] Reproduced with permission.[85] Copyright 2019, Elsevier. Reproduced with permission.[208] Copyright 2018, Springer. Reproduced with permission.[173] Copyright 2019, Elsevier. Reproduced with permission.[155] Copyright 2017, Elsevier.

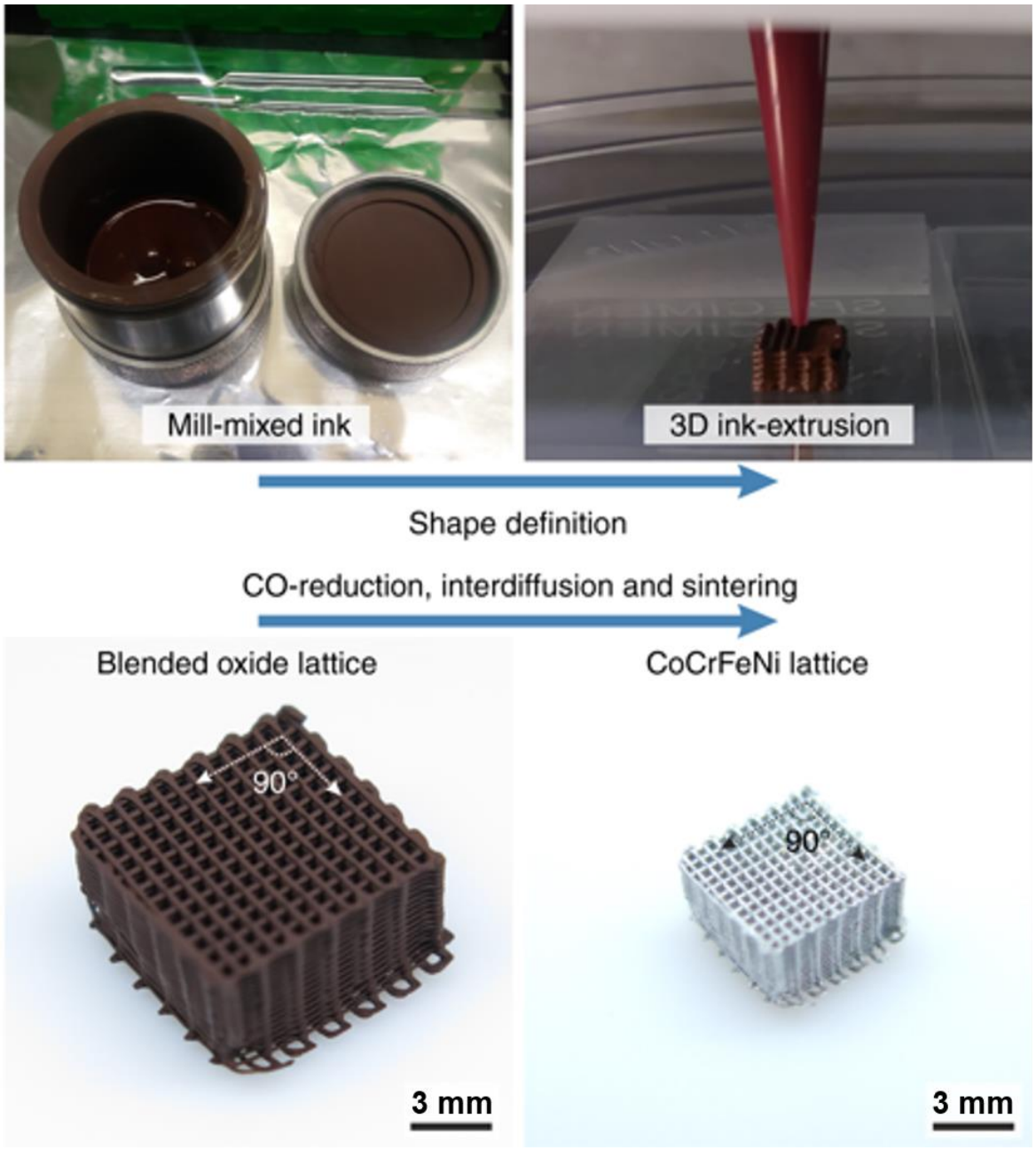

Figure 31. A CoCrFeNi HEA micro-lattice printed using 3D ink-extrusion from mill-mixed ink. The ink for ink-extrusion was mill-mixed and thickened for the shape-defining first step, which defined the architecture. The blended oxide lattice were co-reduced, inter-diffused and sintered to yield a CoCrFeNi HEA lattice with much smaller overall dimensions and strut diameter, without warping or cracking.[217] Reproduced with permission.[217] Copyright 2019, Nature Research.

Table 1. HEA powders developed by gas atomization.

HEA powder	Feedstock	Particle size distribution (μm)	Average particle size (μm)	Phase	Ref.
$AlCoCrFeNi_{2.1}$	Elemental metals	20–80	-	FCC + BCC	[76]
AlCoCrFeNi	-	-	70	BCC	[81]
	Alloy ingot	40–100	-	BCC	[80]
	-	-	70	BCC	[82]
	-	45–105	-	-	[83]
	Elemental metals	-	75	BCC	[84]
$Al_{0.5}CoCrFeNi$	Elemental metals	-	33.5	FCC + BCC	[85]
$Al_{0.6}CoCrFeNi$	Alloy ingot	-	78.65	FCC + BCC	[79]
$Al_{0.5}CoCrFeNiCu$	Alloy ingot	-	27	FCC	[77]
$Al_{0.5}CoCrFeNiCuSi$	Alloy ingot	-	27	FCC + BCC	
AlCoCrFeNiCu	-		47.88	FCC	[86]
CoCrFeNi	Elemental metals	-	35.2	FCC	[87]
CoCrFeNiMn	-	63–160	-	FCC	[88]
	Elemental metals	-	45.2	FCC	[89]
	-	5–45	36	FCC	[90]
CoCrFeNiMn	Alloy ingot	0–53; 100–150	-	FCC	[91]
	-	-	36	FCC	[92]
$CoCrFeNiC_{0.05}$	-	9–85	45	FCC	[93]
$CoCrFeNiMo_{0.2}$	Alloy ingot	15–45	-	FCC	[78]

Table 2. HEA powders developed by mechanical alloying with regard to the feedstock, milling parameters and phases.

HEA powder	Feedstock		Milling parameters				Phase	Crystallite size (nm)	Lattice strain (%)	Ref.
	Purity (wt%)	Particle size (μm)	Ball to powder ratio	Time (h)	Speed (rpm)	Apparatus				
AlCoCrFeCu	99.5	-	10:1	15	300	Pulverisette-P5	FCC + BCC	10	0.5	[116]
$Al_xCoCrFeMnNi$	99	45	18:1	14	600	Pulverisette-P7	FCC	7.4–11.4	0.84–1.28	[117]
AlCoCrFeMnNi	99	45	10:1	40	200	Retsch PM 400	BCC	15-20	0.24–0.70	[109]
AlCoCrFeNiSi	99.5	75	10:1	30	300	QM-3SP2	FCC + BCC	11.7	0.73	[118]
$Al_{0.15}CoCrCuFeNiTi_xC$	99.5–99.9	180	15:1	36	500	KMC-1BV	FCC + BCC	-	-	[119]
$AlCoCrCuFeTi_x$	-	45	10:1	20	300	Pulverisette-P5	FCC + BCC	13–58	0.096–0.231	[120]
$Al_xCrFeMoV$	99.5	-	10:1	7	200	-	BCC	-	-	[121]
$Al_{0.4}CoFeNiSi_{0.4}$	99	-	20:1	70	300	QM-QX4	FCC + BCC	-	-	[122]
$Al_{0.4}CoCr_{0.5}FeNiTi_{0.6}$	99.6	30	10:1	60	-	QM-3SP4	FCC + BCC	7	0.175	[123]
$AlCo_xFeNiSiB$	99.5	75	15:1	140	350	-	BCC	-	-	[124]
$Al_xCoFeNi_{1.5}V_{0.5}Cu_{1-x}$	99.5	48	10:1	70	300	QM-3SP4	FCC + BCC	6.3–7.7	1.21–1.52	[125]
AlCoFeNiCu	99	-	5:1	10	-	SPEX-8000M	FCC + BCC	7.1	-	[126]
AlCoCrFeNiCuTi	99	-	5:1	10	-	SPEX-8000M	FCC + BCC	6.8	-	
AlCoCrFeNiMo	99	-	5:1	10	-	SPEX-8000M	BCC	8.3–16.5	-	
AlCoNiZnCu	99.5–99.8	60	10:1	50	300	Pulverisette-P7	FCC	14.5	0.84	[127]
AlCrFeCuMnW	99.5	-	10:1	20	300	Pulverisette-P7	FCC + BCC	17–25	0.43–0.53	[128]
AlCrFeTiZnCu	99.5	45	10:1	20	300	Pulverisette-P5	BCC	9–10	1.31–1.52	[105]
$(AlCrFeMnV)_{100-x}Bi_x$	99.5	-	20:1	25	200	Pulverisette-P5	BCC + Bi	-	-	[129]
AlNiTiZrCu	99.5	70	15:1	-	350	KE-2L	amorphous	-	-	[130]
CoCrFeNi	99.5	-	10:1	15		Pulverisette-P5	FCC + BCC	10	-	[131]
CoCrCuFeNi	99.5	-	10:1	15	300	Pulverisette-P5	FCC + BCC	7	1	[116]
CoCuFeNi	99.5	-	10:1	15	300	Pulverisette-P5	FCC	9	0.73	
CoCrFeNi	99.5	-	10:1	15	300	Pulverisette-P5	FCC + BCC	6	0.83	

CoCrCuNi	99.5	-	10:1	15	300	Pulverisette-P5	FCC + BCC	6–10	-	[132]
Co_xCrCuFeMnNi	99.5	75	10:1	50	300	QM-WX4	FCC + BCC	5.6–8.9	1.05–1.84	[114]
	99.5	-	10:1	35	200	Pulverisette-P5	FCC	-	-	[133]
CoCrFeMnNi	99.9	-	15:1	45	250	QM-QX4L	FCC	-	-	[134]
$CoCrFeMnNiTi_{0.3}C_{0.3}$	99.9		15:1	45	250	QM-QX4L	FCC + BCC	-	-	
CoCrFeNiTi	99.9	50	25:1	10	400	-	FCC	6.38	1.4	[135]
CrFeNiMnTi	99.9	50	25:1	10	400	-	FCC	5.17	1.84	
CrFeNiTi	99.9	50	25:1	10	400	-	FCC	6.53	1.5	
$Co_{1.5}CrFeNi_{1.5}Ti_{0.5}$	99.5	-	10:1	30	250	-	FCC + BCC	-	-	[136]
$CrFeMoVMn_x$	99	75	10:1	15	200	-	BCC + σ	-	-	[121]
$(CrCuFeTiZn)_{100-x}Pb_x$	99.5	-	20:1	25	200	Pulverisette-P5	BCC + FCC + Pb	-	-	[129]
$(CuCrFeTiZn)_{100-x}Pb_x$	99.5	-	20:1	44	200	Pulverisette-P5	FCC + BCC + Pb	-	0.0372–0.1092	
NbMoTaW	99.9	48	10:1	60	300	TENCAN	BCC	11.8	0.688	[107]
NbMoTaWV	99	75	10:1	6	300	Pulverisette-P5	BCC	66.1	0.96	[137]
NbMoTaWVTi	99.9	-	13:1	40	-	-	BCC	-	-	[138]
NbMoWZrV	99.5	50	10:1	100	-	Pulverisette-P5	FCC + BCC	11	0.58	[139]
$Fe_{18}Ni_{23}Co_{25}Cr_{21}Mo_8WNb_3C_2$	99.5	70	60:1	24	940	-	γ + Mo	-	-	[115]

Table 3. Magnetic properties of reported HEA powders produced by mechanical alloying.

HEA powder	Milling time (h)	Saturation magnetization (emu/g)	Coercivity (Oe)	Ref
$Co_{0.5}$CrCuFeMnNi	50	21	63	[114]
$Co_{1.0}$CrCuFeMnNi	50	32	27	
$Co_{1.5}$CrCuFeMnNi	50	40	19	
$Co_{2.0}$CrCuFeMnNi	0/5/10/15/30/45/50	105/76/79/74/69/51/52	56/85/59/49/33/17/14	
$Al_{0.4}$CoFeNi$Si_{0.4}$	0/10/30/50/70	113/105/94/94/95	65/85/150/160/142	[108]
AlFeNiSiB	140/160/260	8/6/1	380/380/290	[140]
AlFeNiSiBNb	100/180/260	10/4/1	350/350/280	
AlFeNiSiBCo	40/80/140	25/15/2	320/310/230	
AlFeNiSiBC	20/40/80/140/160	53/49/32/35/27	238/338/190/75/80	[141]
AlFeNiSiBCe	20/40/80/140/160	25/6/5/2/2	250/350/325/240/230	
AlFeNiSiBCu	40/80/140	5/3/2	310/290/340	
AlFeNiSiBAg	40/80/140	15/3/2	330/320/310	
CrFeNiTi	20	14	167	[120]
CrFeMnNiTi	20	2	226	
CoCrFeNiTi	20	24	150	

Table 4. The DED processing conditions for printing HEA products.

HEA	Laser power (W)	Scanning speed (mm/min)	Layer thickness (mm)	Oxygen level (ppm)	Apparatus	Ref.
AlCoCrFeNi	800	800	0.25	10	TruLaser Cell 7040	[150]
AlCoCrFeNi	600–650	300	0.7–0.8	-	-	[151]
$AlCo_xCr_{1-x}FeNi$	200–300	400	0.25	10	-	[152]
$Al_xCoCrFeNi$	800	800	-	-	TruLaser Cell 7040	[153]
$Al_xCoCrFeNi$	800–1200	400–1200	-	20	TruLaser Cell 7040	[154]
AlCoCrFeCu	1000–3000	60–900	-	-	TLF1500 TURBO	[155]
$AlCrFeMoV_x$	400	1020	0.254	10	Optomec LENS-750	[156]
AlCrFeNiTa	600–650	300	0.7–0.8	-	-	[151]
CoCrFeMnNi	370	800	-	-	Schuler	[157]
$CoCrFeNiCu_{0.5}$	250	480	-	10	Optomec LENS-750	[158]
TiZrNbMoV	300/1000	300	0.25	10	LENS MR7	[159]
ZrTiVCrFeNi	200–300	96	0.1	10	LENS MR7	[160]
LaNiFeVMn	200–300	96	0.1	10	LENS MR7	[161]

Table 5. Summary of phases and crystal features observed in various HEA products developed by DED.

HEA	Phase	Crystal features	Ref.
AlCoCrFeNi	B2	Periodic and fine grains consisting of ordered B2 phase	[150]
	BCC + B2	Columnar grains; equiaxed grains at the interlayer interface; grain sizes of 27.4–114.2 μm; disordered BCC precipitates in the ordered B2 matrix in the dendrites and interdendrites	[80]
$Al_xCoCrFeNi_{2-x}$	γ (x = 0.3)	Columnar grains with length greater than 1 mm	[164]
	γ + B2 (x = 0.7)	Dendritic structure	
	A2 + B2 + $L1_2$ (x = 1)	Equiaxed grains with alternating Fe-Cr and Al-Ni rich plates with $L1_2$ precipitates	
	A2 + B2 (x = 1.7)	Dendritic structure with alternating Fe-Cr and Al-Ni rich plates	
$Al_xCoCrFeNi$	FCC (x = 0.3)	Columnar structure with elongated grains longitudinal to the build direction and equiaxed grains transverse to the build direction; segregation of Al in grain boundaries	[153, 171]
	FCC + BCC (x = 0.6)	Widmanstätten grains with random crystallographic orientations	
	BCC (x = 0.85)	Columnar structure	
	FCC (x = 0.3)	Columnar grains with an average size of 40.9 μm; uniform cellular substructures with an average size of 5.7 μm in grains	[154]
	FCC + BCC (x = 0.6)	Columnar grains with an average size of 38.2 μm; a dispersion of FCC phase in the matrix of columnar BCC grains	
	BCC (x = 0.85)	Columnar grains with an average size of 32.5 μm; segregation of Cr and Fe in grain boundaries	
	FCC (x = 0.3)	Elongated grains	[165]
	FCC + B2 (x = 0.7)	FCC lamella widths of 2–3 μm	
$AlCo_xCr_{1-x}FeNi$	B2 (x = 1)	Columnar grains with an average size of 100 μm in length and 25 μm in width	[152]
	BCC + B2 + FCC (x = 0.8)	Equiaxed grains with an average size of 25μm; disordered BCC uniformly distributed within ordered B2 matrix; precipitation of disordered FCC phase in grain boundaries	
	BCC (x = 0.6)	Equiaxed grains with an average size of 25μm; A fine substructure in grains	
	BCC + B2 (x = 0.4)	Equiaxed grains with an average size of 40 μm; ordered B2 enriched in Al, Ni, and Co, disordered BCC enriched in Fe and Cr	
	BCC + B2 (x = 0.2)	Columnar grains with an average size of 150 μm in length and 240 μm in width	
	BCC + B2 (x = 0)	Columnar grains with an average size of 150 μm in length and 10 μm in width; ordered B2 enriched in Al and Ni, and disordered BCC enriched in Fe and Cr	

$Al_xCrCuFeNi_2$	FCC + BCC (x = 0)	Dendritic structure	[163]
	FCC (x = 0.4)	Dendritic structure; cellular boundary structure with fine precipitates; segregation of Cu in to interdendritic regions	
	FCC + $L1_2$ + BCC + B2 (x = 0.8)	Dendritic structure with coarse and fine needle-like BCC/B2 precipitates	
	FCC + $L1_2$ + BCC + B2 (x = 1.0)	Equiaxed grains with coarse and fine needle-like precipitates	
	FCC + $L1_2$ + BCC + B2 (x = 1.3)	Large equiaxed grains of BCC/B2 with highly refined intragranular precipitates of FCC/$L1_2$	
	FCC + BCC + B2 (x = 1.5)	Fine-scale equiaxed grains; eutectic mixture of BCC and B2 phases; FCC precipitates	
$Al_xCoFeNiCu_{1-x}$	FCC (x = 0.25)	Columnar dendritic grains	[172]
	FCC (x = 0.5)	Columnar dendritic grains	
	FCC + BCC (x = 0.75)	Dendritic FCC structure enriched in Co and Fe; BCC matrix enriched in Al and Ni	
$AlCrFeMoV_x$	BCC (x = 0.3 at%)	Equiaxed grains with an average size of 68 μm	[156]
	BCC (x = 10 at%)	Elongated grains with an average size of 127 μm in length and 56 μm in width	
	BCC (x = 18.5 at%)	Elongated grains with an average size of 165 μm in length and 110 μm in width	
CoCrFeMnNi	FCC	Fine cellular dendrite structure with sizes of 2.9–5.2 μm	[157]
		Columnar and equiaxed grains	[173]
		Equiaxed grains with an average size of 3.68 μm and dendritic columnar grains with an average size of 3.11 μm in width; grain boundaries enriched in Mn and Ni	[174]
		Columnar grains with an average size of 13 μm and micro-sized cellular substructures	[175]
TiZrNbTa	BCC	From equiaxed grains to elongated grains along with grain sizes of 2–60 μm	[149]
TiZrNbHfTa	BCC	Equiaxed grains with random orientations	[168]
TiZrNbMoV	BCC + $NbTi_4$	Dendrites composed of BCC and $NbTi_4$-type phases with Zr-rich precipitates; no dendritic segregation	[159]
ZrTiVCrFeNi	C14 + αTi	Irregular cell-like structure with an average grain size of 50 μm	[160]
$La_{0.1}Ni_{0.5}Fe_{0.1}V_{0.1}Mn_{0.2}$	FCC + La(Ni, Mn)$_5$	FCC dendritic microstructure	[161]
$La_{0.03}Ni_{0.17}Fe_{0.2}V_{0.2}Mn_{0.4}$	σ + La(Ni, Mn)$_5$	Granular La(Ni, Mn)$_5$ precipitates; (V, Mn)-rich needle-like precipitates in the σ matrix	
$AlCoCrFeCu/Y_2O_3/ZrO_2$	I + $AlCu_2Zr$ + Amorphous	Block-shape crystalline phases composed of ultrafine nanocrystals	[155]

Table 6. Summary of relative density, phase and crystal features in SLM-printed HEA products.

HEA	Relative density (%)	Phase	Crystal features	Ref.
$Al_{0.5}CoCrFeNi$	-	FCC	Coarse columnar grains and fine equiaxed grains	[85]
AlCoCrFeNi	98.4	A2 + B2	Epitaxial growth of columnar A2 grain bundles perpendicular to the melt pool boundary with an average grain size of 1.5 μm; the B2 phase is between A2 grains; Precipitates enriched in Fe and Cr	[193]
	-	A2 + B2	Elongated grains with an average size less than 20 μm; B2 subgrains with sizes of 20–30 nm	[195]
AlCoCuFeNi	-	B2	Fine columnar grains located along melt pool boundaries in the <001> orientation and equiaxed grains at the centre of melt pools with <001> and <101> orientations; an average size of 10 μm for B2 subgrains	[196]
AlCrCuFeNi	99.7	A2 + B2	Fine columnar grains consisting of ultrafine subgrains with a <100> preferred orientation; precipitation of nano-scale Cu-rich phases with chain-like and granular shape	[197]
$Al_{0.26}CoFeMnNi$	99.5	FCC	Microstructure enriched in Co, Fe, and Ni under low energy densities	[198]
$AlCoFeNiSm_{0.1}TiV_{0.9}$	-	FCC	Uniformly distributed equiaxed grains with random orientations; no element segregation	[199]
CoCrFeNi	-	FCC	Fine grains with dissimilar crystallographic orientations	[187]
	98.7	-	Epitaxial growth of columnar grains with an average size of 3 mm in length and 200 μm in width	[200]
CoCrFeMnNi	98.2	FCC + σ	Epitaxial growth of grains to form elongated columnar grains with a <001> orientation parallel to the build direction	[90]
	-	FCC	Epitaxial growth and competitive grain growth	[188]
	99.2		A hierarchical microstructure with columnar grains along the build direction and a typical submicron cellular structure	[92]

	-		A hierarchical microstructure with epitaxial growth of grains with sizes of 5.98–15.66 μm; cellular- and columnar-type structures within the grains	[194]
	-		Elongated grains with a preferred growth <001> direction along the build direction	[201]
$CoCrFeNiC_{0.05}$	99	FCC	Fine columnar-like grains with sizes of 40–50 μm; cellular and columnar subgrains with an average size of 500 nm; precipitates enriched in C and Cr	[202]
$Co_{1.5}CrFeNi_{1.5}Ti_{0.5}Mo_{0.1}$	99.3	FCC + Single cubic + HCP	Fine uniform microstructure with no visible segregations	[203]
MoNbTaW	-	BCC	Lamellar martensite structure dendrites with the primary and secondary dendrite arm spacings of 6.59 and 1.68 μm, respectively	[204]
$Ni_6Cr_4WFe_9Ti$	-	FCC + Unknown phase	Columnar dendritic and fine equiaxed dendritic structures; tiny precipitates (unknown phase) with sizes of 30–50 nm dispersed on intragranular boundaries	[205, 206]

Table 7. Comparison of microstructures of typical HEA products manufactured by both 3D printing and conventional processes.

Manufacturing method		**AlCoCrFeNi**	**Ref.**
3D printing	DED	Ordered B2 + disordered BCC phases; grain sizes of 27.4–114.2 μm; BCC precipitates; (Al, Ni)- rich in B2 and (Cr, Fe)-rich in BCC	[80]
	SLM	Ordered B2 + disordered A2 phases; grain sizes less than 20 μm; BCC precipitates; (Al, Ni)- rich in B2 and (Cr, Fe)-rich in BCC	[193, 195]
	EBM	Ordered B2 + disordered BCC + FCC phases; an average grain size of 10 μm; FCC precipitates; (Al, Ni)- rich in B2 and (Cr, Fe)-rich in BCC	[83]
Conventional process	Cast	Ordered B2 + disordered BCC phases; an average grain size of 179.3 μm; BCC precipitates; Al and Ni segregated into dendrites, and Cr and Fe segregated into interdendrites	[80]
	Powder metallurgy	Ordered B2 + disordered BCC + FCC phases; grain sizes of 10–20 μm; B2 + σ precipitates	[220, 221]
Manufacturing method		**CoCrFeMnNi**	**Ref.**
3D printing	DED	FCC phase; columnar grain sizes with several hundred microns in length and 3.11 μm in width; Ni and Mn segregated into grain boundaries	[174]
	SLM	FCC phase; grain sizes of 5.98–15.66 μm; σ phase precipitate; Mn segregated into melt pools	[90, 194]
	EBM	FCC phase; cellular grains with an average size of 2.9 μm; Co, Cr and Fe segregated into dendrites, and Mn and Ni segregated into interdendrites	[75]
Conventional process	Cast	FCC phase; grain sizes greater than 1000 μm; Cr and Mn segregated into interdendrites	[222, 223]
	Powder metallurgy	FCC phase; an average grain size of 25 μm	[88]

Table 8. Tensile and compressive properties of 3D-printed HEA products, compared with those manufactured by conventional processes. UTS, UCS, YS and EI represent ultimate tensile strength, ultimate compressive strength, yield strength and elongation, respectively.

HEA	Printing process	Tensile property			Compressive property			Ref.
		YS (MPa)	UTS (MPa)	EI (%)	YS (MPa)	UCS (MPa)	EI (%)	
CoCrFeMnNi	DED	518	660	19.8	-	-	-	[174]
		-	-	-	260	1400	52	[157]
		290	535	55	-	-	-	[173]
		346	566	27	-	-	-	[228]
		517	650	16	-	-	-	[175]
		424	651	48	-	-	-	[229]
CoCrFeMnNi	DED + Annealing	232	647	58	-	-	-	
$Al_{0.3}$CoCrFeNi	DED	194	-	38	194	1400	-	[171]
Al_xCoCrFeNi		-	-	-	200–1400	1400–2100	2.5–10	[153]
$Al_{0.3}$CoCrFeNi	DED + HIP	-	825	6	183	-	-	[230]
$Al_{0.6}$CoCrFeNi		400	952	1	-	1595	74	
$Al_{0.85}$CoCrFeNi		-	-	-	1300	-	3	
AlCoCrFeNi	DED + Aging	-	-	-	1070–1310	2600–3020	16.8–24.9	[151]
$Al_{0.5}$CoCrFeNi	SLM	579	721	22	-	-	-	[85]
AlCoCrFeNi		-	-	-	1342	1471	6.4	[196]
AlCoCrFeNi	SLM + Annealing	-	-	-	744–766	1292–1600	11–16	
AlCrCuFeNi	SLM	-	-	-	-	2053	6.8	[197]
CoCrFeNi		402–600	480–745	8–32	-	-	-	[187]
		572	691	17.9	-	-	-	[200]
CoCrFeMnNi		519	601	34	-	-	-	[90]
		510	609	34	-	-	-	[92]
		-	-	-	703.5–778.4	-	-	[194]
$CoCrFeNiC_{0.05}$		656	797	13.5	-	-	-	[93]
		638	795	13.5	-	-	-	[202]
$Co_{1.5}CrFeNi_{1.5}Ti_{0.5}Mo_{0.1}$		773	1178	25.8	-	-	-	[203]
$Ni_6Cr_4WFe_9Ti$		742	972	12.2	-	-	-	[205]
		630–710	920–983	8.6–12.9	-	-	-	[206]
AlCoCrFeNi	EBM	769	1074	1.2	944–1015	1447–1668	14.5–26	[81, 82]

CoCrFeMnNi		205	497	63	-	-	-	[75]
$Co_{1.5}CrFeNi_{1.5}Ti_{0.5}Mo_{0.1}$		743.4	932	4	-	-	-	[203]
CoCrFeNi	3D extrusion + Sintering	250–388	598–864	33.8–37.6	-	-	-	[217]
AlCoCrFeNi	Binder jetting + Annealing	-	-	-	1203–1461	1996–2272	31.5–32.3	[218]
	Cast	-	-	-	1308.3	1425	5.6	[81]
CoCrFeMnNi		205	493	55	-	-	-	[231]
CoCrFeNi		188	457	50	-	-	-	[187]
AlCrCuFeNi		-	-	-	-	1750	1.8	[232]
$Al_{0.5}CoCrFeNi$		334	709	43	-	-	-	[233]
CoCrFeMnNi	Weld	270	565	30	-	-	-	[234]
	Sintering	312	613	27	-	-	-	[88]
CoCrFeNi	Hot extrusion	359	713	56	-	-	-	[87]

Table 9. Electrochemical parameters of 3D-printed HEA products.

HEA	Process	Solution	Corrosion potential (mV)	Pitting potential (mV)	Corrosion current density ($\mu A/cm^2$)	Ref.
AlCoCrFeNi	EBM	Artificial seawater	-355	112	1.45	[82]
	DED + Aging (800℃)	0.6 M NaCl	-264.1	5.1	0.117	[150]
	DED + Aging (1000℃)		-259.6	-7.2	0.129	
	DED + Aging (1200℃)		-240.9	35.5	0.089	
CoCrFeMnNi	DED		-250	400	-	[229]
	SLM	3.5 wt% NaCl	-189	197	0.09	[242]
$Co_{1.5}CrFeNi_{1.5}Ti_{0.5}Mo_{0.1}$	EBM		-	500	-	[213]
	EBM + Water quenching		-	900	-	
	EBM + Air cooling		-	840	-	
	SLM		-	880	-	[203]
	SLM + Water quenching		-	1000	-	
	SLM + air cooling		-	800	-	
AlCoFeNiTiVZr	SLM		-755	10	36.31	[199]
$AlCoFeNiSm_{0.05}TiV_{0.95}Zr$			-665.9	10	10.96	
$AlCoFeNiSm_{0.1}V_{0.9}$			-655	-	8.32	
$AlCoFeNiSm_{0.1}TiV_{0.9}$			-628.3	-	6.75	
MoNbTaW			-91.57	-	0.00024	[204]

Table 10. A comparative summary of DED, SLM and EBM processes for printing HEA products.

	DED	**SLM**	**EBM**
Number of HEA types	17	15	4
Environment	Argon	Argon	Vacuum
Feedstock	Pre-alloyed powder, elemental powder	Pre-alloyed powder	Pre-alloyed powder
Powder feed	Brown powder	Powder bed	Powder bed
Energy source	Laser	Laser	Electron beam
Scanning speed (mm/s)	1–20	10–2000	215–3446
Preheating (°C)	-	-	900–1253
Residual stress	High	High	Very low
Tensile yield strength (MPa)	194–518	402–773	205–769
Ultimate tensile strength (MPa)	535–660	480–1178	497–1074
Elongation (%)	19.8–55	8–34	1.2–63
Microhardness (HV)	195–860	212–829	157–500

Author Photographs

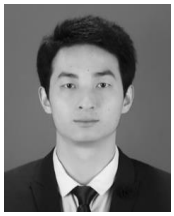

Changjun Han received his Ph.D. from the School of Materials Science and Engineering, Huazhong University of Science and Technology, China in 2018. Currently, He works as a Postdoctoral Fellow with Prof. Kun Zhou at the School of Mechanical & Aerospace Engineering, Nanyang Technological University, Singapore. His research interest focuses on additive manufacturing of metals.

Kun Zhou is an Associate Professor at the School of Mechanical & Aerospace Engineering, Nanyang Technological University, Singapore. His research interests focus on micro/nano mechanics of materials and structures, modelling and design of sustainable materials and additive manufacturing.

Table of Contents

3D printing of HEAs has great potential for manufacturing geometrically complex and/or customized HEA products with desirable performances, inspiring their increased manifestation in industrial applications. This article provides a comprehensive review of the recent advances on the 3D printing of HEAs, in the aspects of their powder development, printing processes, microstructures, mechanical properties, functionalities and potential applications.

Keywords: 3D printing, additive manufacturing, high-entropy alloys, rapid solidification, powder development

*Changjun Han, Qihong Fang, Yusheng Shi, Shu Beng Tor, Chee Kai Chua, Kun Zhou**

Recent Advances on High-Entropy Alloys for 3D Printing

ToC figure